DEVELOPMENT OF MESOSCALE BURNER ARRAYS FOR NEXT GENERATION COMPACT GAS TURBINES

BY

JEONGAN CHOI

DISSERTATION

Submitted in partial fulfillment of the requirements
for the degree of Doctor of Philosophy in Mechanical Engineering
in the Graduate College of the
University of Illinois Urbana-Champaign, 2021

Urbana, Illinois

Doctoral Committee:

Professor Tonghun Lee, Chair and Director of Research
Professor Moshe Matalon
Assistant Professor Lili Cai
Assistant Professor Francesco Panerai

ABSTRACT

In this study, a multi-node mesoscale burner array for compact gas turbines was developed. The burner array was designed to improve the overall combustion stability by exploiting flame-to-flame interactions under fuel-lean operation. Moreover, its design can be adjusted by scaling the element dimensions or array size to flexibly accommodate a wide range of combustion power outputs. The combustion characteristics of the mesoscale burner array were experimentally investigated using several optical diagnostic and analysis techniques. Lean blow off limit, flame temperature, and NO emission measurements were performed on the mesoscale burner array; the obtained measurements were compared with those of a baseline single-swirl burner. Furthermore, various flame structures from the mesoscale burner array were visualized using OH and CH_2O planar laser-induced fluorescence (PLIF).

Next, a diffusion type mesoscale burner array was developed and investigated for small-scale combustion applications. Each burner element in the diffusion mesoscale burner array was equipped with its own fuel injection holes built into its swirl-inducing geometry to improve flame interactions and reduce flame length. The performance of the diffusion mesoscale flame array is comparable to that of a premixed mesoscale flame array under similar operating conditions despite fuel unpremixedness.

Furthermore, the combustion experiments were extended for a liquid fuel (Jet A) and the results successfully demonstrated the potential for the integration of heavy hydrocarbon liquid fuels. The mesoscale burner array was investigated using pre-vaporized Jet A fuel. The effects of inlet temperature on Jet A flames in the mesoscale burner array were studied. Then, the flame characteristics of the Jet A and methane flames in the mesoscale burner array were compared. The results provide solid foundation for designing and operating small-scale combustors that are

operated with heavy hydrocarbon fuels. Moreover, hydrogen addition effects on the burner array were studied to improve the flame stability and combustion dynamics because hydrogen enhancement can be a promising solution for small-scale combustion systems.

In summary, this study demonstrates the potential for a novel combustor architecture that can be scaled across a wide range of power outputs with minimal performance degradation for next generation propulsion and power systems.

ACKNOWLEDGMENTS

Looking back on my life at UIUC, I liken it to climbing a steep mountain. Now that I have reached the peak, I have a chance to look forward to new adventures and to reflect on all the help that made this achievement possible.

First and foremost, I want to express my sincere gratitude to my research advisor Prof. Tonghun Lee for supporting and guiding my Ph.D. research. His lab provided me a great research environment, excellent facilities, and the chance to collaborate with top-notch lab mates. It was a great honor to study and work under his guidance. In addition, special thanks to my committee members, Prof. Moshe Matalon, Prof. Francesco Panerai, and Prof. Lili Cai, for their advice and guidance. I really appreciate the time and support they gave me during both my prelim and final defense. I also want to thank Professor Jihyung Yoo at Hanyang University for his support during my mesoscale burner research.

I am grateful as well to Dr. Constandinos Mitsingas and Dr. Rajavasanth Rajasegar for their support. When I first joined this lab, their assistance enabled me to develop experiment skills and to adapt to my new surroundings. Thanks also to Dr. Qili Liu and Dr. Brendan McGann for helping me whenever problems arose during experiments. Furthermore, to all the members of the Laser Diagnostics Laboratory for Advanced Energy and Propulsion Research, I really appreciate every moment we enjoyed or worked together. I wish everyone good luck and happiness in your Ph.D. journeys.

Finally, I especially want to thank my family and friends whose support made it possible for me to successfully complete my studies and research work and to overcome all the challenges I faced throughout this process.

To my family and friends

TABLE OF CONTENTS

LIST OF FIGURES

LIST OF TABLES

CHAPTER 1. INTRODUCTION

1.1. Background and motivation

1.1.1. Compact combustors

Most gas turbine technologies geared towards small-scale combustors have been motivated by the fact that hydrocarbon fuels have higher energy densities than those of commercial fuel cells or batteries [1, 2]. Even accounting for conversion losses in practical applications, hydrocarbon fuels can easily outperform other power sources. However, a vision of a truly compact high-efficiency combustor is still elusive due to a number of key technical challenges.

Smaller flames in compact geometries are susceptible to thermal and chemical quenching, potential extinction mechanisms that can affect flame stability [3-5]. Moreover, compact and restricted dimensions can induce incomplete air/fuel mixing and insufficient residence time [6]. These concerns should be addressed in order to develop small-scale combustors with applications ranging from portable power generation sources to micro gas turbine combustors [2, 7].

The development of compact power generation, which incorporates the concepts of both micro-reactors along with energy conversion devices, has been investigated in the literature. Starting in the late 90s, MIT's Gas Turbine Research Laboratory developed a range of micro gas turbine engines using silicon based MEMS micro-fabrication technology [8]. Notably, Swiss-roll burners based on heat recirculation have been designed and studied for small scale power generation systems [9, 10]. For use of liquid fuel, meso-scale catalytic combustors were developed using electrospray in combination with direct energy conversion modules [11, 12].

In an effort to achieve higher performance in compact combustors, many studies have considered the use of heat recirculation to minimize heat loss and increase thermal efficiency.

Flames stabilized within the matrix of a porous media have higher burning speeds and leaner flammability limits than open flames, due to the internal feedback of heat from the burned gases by radiation and conduction through the porous medium [13]. The integration of a heat recuperator can also increase combustion efficiency and provide fuel vaporization capability by increasing combustor inlet temperature. Ceramic composite based recuperators offer a solution to this issue and novel ceramic recuperators for micro turbines have been investigated by Vick *et al.* [14]. Other radical design changes include the ultra compact combustor (UCC) from Air Force Institute of Technology. This is a promising new design which exploits circumferential flow to reduce engine size by altering the flow path through the combustor [15]. A number of previously studied technologies for compact combustors are listed in Table 1.1.

Combustor / Project	**Technology**	**Material**	**Note**	**Ref.**
Micro-gas turbine	Micro fabrication	Silicon	Silicon-based combustion systems	[8]
Swiss roll	Heat recuperation	Steel / Ceramic	Miniaturization / Improved extinction limits	[9, 10]
Meso scale catalytic	Electrospray	Catalyst grid	Dispersion of the liquid fuel using electrospray	[11, 12]
Porous media burner	Heat recuperation	Porous ceramic	Radiation & conduction from the reaction	[13]
Ceramic recuperator	Heat recuperation	Silicon nitride	Ceramic injection molding	[14]
Ultra compact combustor	Cavity	Stainless steel	Circumferential cavity to enhance reaction	[15]

Table 1.1 Prior technologies focused on compact combustion systems.

1.1.2. Combustion instability

Modern combustors must be capable of achieving high efficiency while complying with stringent emission regulations. A commonly accepted solution for reducing emissions (NO_x in particular) is to lower the combustion temperature using lean premixed combustion [16]. Large combustors for power generation predominately operate near the lean stability limit for this very reason. However, lean premixed combustion is more susceptible to combustion instabilities and can therefore cause major performance deterioration in a wide range of applications [17]. These instabilities are often attributed to closed-loop thermo-acoustic coupling between pressure fluctuations and unstable heat release, thereby resulting in overall performance degradations, total engine flame out, and even catastrophic engine failures as shown in *Figure 1.1* [18, 19].

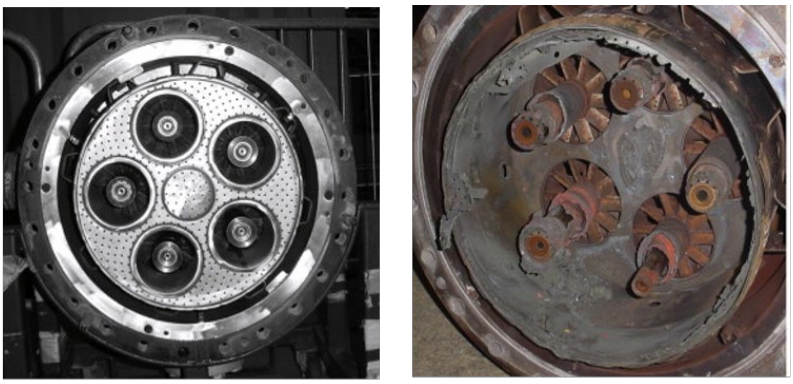

Figure 1.1 Undamaged gas turbine burner assembly and damaged burner face due to combustion instability. [19]

Large scale systems can potentially minimize the impact of combustion instability through active and passive combustion instability control strategies [19]. However, these mitigation strategies may not be applicable to small scale systems where smaller flames are driven by

different physical and chemical characteristics than those of larger flames. For example, smaller flames are susceptible to thermal and chemical quenching, a potential extinction mechanism that can affect flame stability [3-5]. Furthermore, compact burner dimensions may limit fuel mixing and residence time, thereby compromising efficient and stable combustor operation [6]. The reduced residence time may also coincide with the characteristic chemical reaction time scale of the burner, resulting in insufficient heat generation, flame extinction, and unsteady combustion dynamics [20-22]. These concerns must be addressed for compact burners to potentially replace batteries in high-powered and small-scale applications [2, 7].

1.2. Objective

The principal vision of this work is to investigate the novel concept of swirl-stabilized mesoscale burner arrays, which can potentially be utilized in the next generation of small-scale gas turbines. The new architecture can provide dramatic improvements in flame stability and susceptibility to extinction, while maintaining low NOx emission levels. Most importantly, this unique architecture can be scaled and applied to a wide range of combustion systems from macro-scale gas turbines to small-scale portable units without performance degradation.

The basic concept of a mesoscale swirl-stabilized burner is shown in Figure 1.2 along with three prototypes with different array sizes. The prototypes consist of individual swirl-stabilized counter rotating flames arranged in a Taylor-Green vortex configuration [23]. The complex flame-to-flame interactions dictated by this configuration generate an array of flames which are mutually supported between the individual nodes.

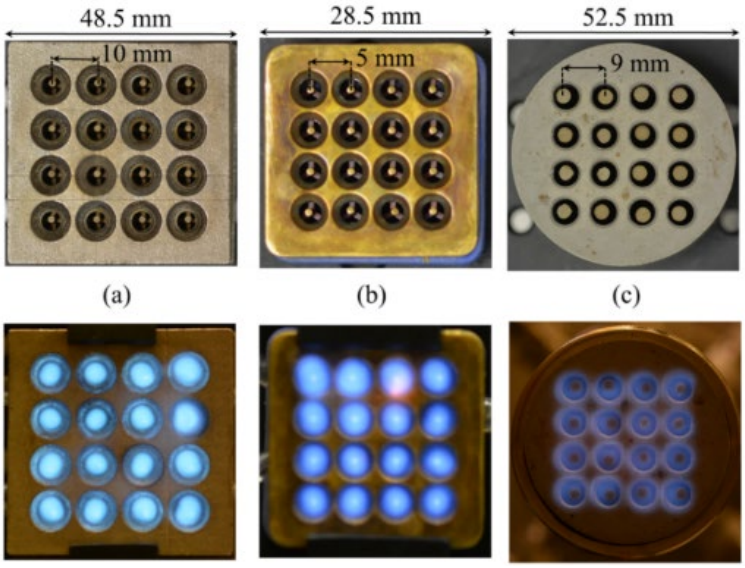

Figure 1.2 Various 3D metal printed mesoscale array burner concepts. [24]

The overall combustor size can be scaled up or down by integrating more or less nodes and adjusting the size of individual nodes to match the overall combustion power. The intricate design features, enabled by using novel 3D additive metal printing techniques, can be easily modified using a variety of metal substrates such as titanium alloys, stainless steel, Inconel 625, and Inconel 718. A mesoscale burner array can offer substantial benefits in comparison to the single or multi-cup swirl combustors that are commonly used today. These benefits are listed below in Table 1.2.

- ***Compact combustor design:*** Fuel-air mixing is performed at a scale where molecular mixing is sufficiently fast to achieve compact yet well distributed flames. This allows for significant decrease in the overall engine length with good control over the pattern factor (uniform temperature distribution at the combustor exit).
- ***Lower NOx emissions:*** Mesoscale arrays can sustain stable flames over a wide range of lean operating conditions due to the faster diffusion scales. Also, mesoscale arrays are suited for employing highly vitiated combustion to achieve uniform oxidation over the reaction zone, resulting in lower emission levels.
- ***Improved flame stability:*** The mesoscale array employs multiple flames arranged in a counter-rotating pattern (Taylor-Green vortex array). This configuration improves flame stability as any single flame can propagate over the entire array during ignition or in the case of a local extinction.
- ***Scalability:*** A key benefit of the mesoscale burner array is scalability to facilitate potential incorporation into larger combustors without lengthening of the axial dimension.

Table 1.2 Benefits of a mesoscale burner array.

This burner design can improve combustion stability compared to a single swirl combustor by exploiting flame interactions [24]. Therefore, burner arrays can be used to achieve significant weight reduction and improve the aspect ratio (compactness) of a gas turbine engine while enhancing design flexibility. Furthermore, optimized flame interactions on the mesoscale burner array can improve scaling and seamless integration of the burner array over a wide range of operating conditions without causing performance degradation. Despite its importance, the complex nature of flame interactions on mesoscale burner stability is not fully understood and hence necessitates a comprehensive study.

1.3. Chapter summary

- Chapter 1: This chapter highlights the background and motivation of this dissertation.
- Chapter 2: This chapter introduces a mesoscale burner array, designed to improve combustion stability. The performance evaluation of the burner array was carried out by several diagnostic and analysis techniques. The mesoscale burner array showed improved flame stabilization compared to a single swirl burner under fuel lean operation.
- Chapter 3: In this chapter, a diffusion mesoscale burner array with an integrated fuel manifold and injection holes is introduced. The burner array was developed for compact and efficient propulsion systems. The flame characteristics of the diffusion burner array were studied compared to premixed flames on a mesoscale burner array.
- Chapter 4: This chapter focuses on flame structures and combustion characteristics of Jet A fuel in a mesoscale burner array. Jet A is fully or partially vaporized and used to analyze Jet A flame characteristics. Flame structures and characteristics of Jet A flames were studied and compared to methane flames.
- Chapter 5: In this chapter, a hydrogen-enriched methane flame in a mesoscale burner array was investigated. Flame structures and characteristics were studied in terms of hydrogen volumetric concentration from 0 to 50%.
- Chapter 6: This chapter demonstrates the effects of hydrogen enhancement on flame stability in a mesoscale burner array, subjected to external perturbations. Two different

transverse acoustic perturbation configurations, a pressure node and a pressure antinode, were imposed on the mesoscale burner array.

- Chapter 7: Major conclusions and recommended future works are summarized in this chapter.

The research in this dissertation includes journal articles previously published by the author and manuscripts currently under review for publication. The list of those articles is as follows:

1. Rajavasanth Rajasegar, **Jeongan Choi**, Brendan McGann, Anna Oldani, Tonghun Lee, Stephen D Hammack, Campbell D Carter, Jihyung Yoo, "Mesoscale burner array performance analysis", ***Combustion and Flame***, Vol. 199, pp. 324-337, (2019).

2. **Jeongan Choi**, Rajavasanth Rajasegar, Constandinos M. Mitsingas, Qili Liu, Tonghun Lee, Jihyung Yoo, "Effect of flame interaction on swirl-stabilized mesoscale burner array performance", ***Energy***, Vol. 192, p. 116661, (2020).

3. **Jeongan Choi**, Rajavasanth Rajasegar, Tonghun Lee, Jihyung Yoo, "Development and characterization of swirl-stabilized diffusion mesoscale burner array", ***Applied Thermal Engineering***, Vol. 175, p. 115373. (2020)

4. **Jeongan Choi**, Rajavasanth Rajasegar, Wooyoung Lee, Tonghun Lee, Jihyung Yoo, "Hydrogen enhancement on a mesoscale swirl stabilized burner array", ***International Journal of Hydrogen Energy***, in press. (2021)

5. **Jeongan Choi**, Rajavasanth Rajasegar, Qili Liu, Tonghun Lee, Jihyung Yoo, "Jet A combustion in a mesoscale swirl-stabilized combustor array", ***Energy & Fuels***, in press. (2021)

6. **Jeongan Choi**, Wooyoung Lee, Rajavasanth Rajasegar, Tonghun Lee, Jihyung Yoo, "Effects

of hydrogen enhancement on mesoscale burner array flame stability under acoustic perturbations”, under review.

CHAPTER 2. MESOSCALE BURNER ARRAY PERFORMANCE ANALYSIS

Combustion characteristics have been experimentally analyzed in a mesoscale burner array using several optical diagnostic and analysis techniques. The mesoscale burner array was designed to improve combustion stability under fuel-lean operating conditions, by inducing flame-to-flame interactions. The 4×4 mesoscale burner array exhibited stable burner operation up to 3 kW and represented a novel design to flexibly accommodate a wide range of combustion power outputs by scaling the element dimensions or array size. Flame stabilization mechanisms were studied using hydroxyl (OH) and formaldehyde (CH_2O) planar laser-induced fluorescence (PLIF) of premixed methane (CH_4) and air flames at various operating equivalence ratios. Combustion heat release rate was also estimated by the product of OH and CH_2O-PLIF images. Lean blow off limits and emissions were analyzed across a wide range of equivalence ratios to better understand mesoscale burner array combustion characteristics. Marked improvement in combustion stability was observed compared to a single swirl-stabilized flame of similar power output. Results indicate that mesoscale burner arrays can serve as next generation propulsion and power systems.

2.1. Introduction

In recent years, improving the efficiency of gas-turbine engines while complying with stringent emission regulations has become a significant challenge. Furthermore, combustion instabilities are a major problem in the design of modern high-performance propulsion systems [25]. They often manifest as large amplitude pressure oscillations that result in many undesirable effects and can lead to performance degradation [18]. Combustion instabilities refer to self-sustained combustion oscillations at or near the acoustic frequency of the combustion chamber, which arise due to the closed-loop coupling between unsteady heat release and pressure fluctuations [17]. These phenomena can induce unstable operations where enhanced heat transfer at combustor walls may lead to partial or total blow off [17, 25]. Furthermore, the oscillations, which are typically low frequency, induce large mechanical vibrations in the system that may ultimately result in combustor failure. Combustion instabilities are a major concern for modern gas turbines that are being designed to operate under ultra-lean conditions. These operating modes result in significant reductions in NOx emissions and maintenance cost due to lower flame temperatures, which also promote increased component life time [26]. However, reduced turbine inlet temperatures can lead to combustion instabilities in addition to lowering the efficiency and specific work output of the engine. Even small perturbations in lean premixed combustion can trigger strong combustion instabilities [19] that exacerbate lean blow out susceptibility. Thus, the potential harm to system performance posed by combustion instabilities often necessitates flame oscillation mitigation during the development of a new combustion system. However, modifications to existing combustor designs may not satisfactorily fulfill both design requirements. Hence, a different combustion architecture may be necessary to alleviate the tradeoff noted above.

This research utilizes highly distributed, millimeter-scale combustion arranged in a grid array to improve combustion stability. A mesoscale burner array [24, 27] featuring 16 interacting swirl-stabilized burner elements arranged in a 4×4 counter rotating vortex pattern known as Taylor-Green vortex array [23] was built. Individual burner elements support nearby elements via flame-to-flame interactions. Despite overall smaller flame size, this configuration promotes a more stable flame characteristics. A single remaining flame after ignition or partial blow off can propagate over the entire array. Each mesoscale burner element consists of a center bluff body surrounded by two tangential inlets to induce swirling motion. A diverging quarl at the burner exit promotes flow divergence and improves the recirculation zone strength [26] leading to rapid diffusion. The main benefit of this architecture is that the fuel-air mixing is performed at a scale where molecular mixing is sufficiently fast to achieve very compact (in axial length) yet uniform flame distribution over the array. These flames allow for significant reduction in overall engine length with good control over pattern factor. Furthermore, these flames allow for low premixed NOx emission levels as they employ highly vitiated combustion in which the air-fuel mixture is diluted with previously burned gas and oxidized homogeneously over the reaction region. The novel mesoscale burner array architecture can provide dramatic improvements in flame stability and extinction susceptibility, while maintaining low NOx emission levels. This is due to the highly distributed combustion, near-diffusive mixing scale, and flame interactions. Thus, the architecture can be adopted over a wide range of combustor outputs.

In this study, several diagnostic and analysis techniques were employed to characterize mesoscale burner array combustion. First, a simultaneous multispecies planar laser-induced fluorescence (PLIF) diagnostic (OH and CH_2O) technique identified various flame-to-flame interaction mechanisms and explored mesoscale burner array flame phenomenology. Second, lean

blow off limits provided additional insight into flame stability. Third, emission measurements using a gas chromatography–mass spectrometry (GC-MS) and a gas analyzer probed mesoscale flame combustion efficiency. Fourth, flame temperature measurements indicated thermal performance of the mesoscale flame array. The same analyses were also performed on a single swirl-stabilized burner with similar power output for comparison.

2.2. Experimental setup and diagnostics

2.2.1. Combustor setup

The mesoscale burner array shown in Figure 2.1 (a) and (b) consists of 16 individually swirl-stabilized mesoscale burner elements. The burner array is fabricated as a single monolithic unit via a direct metal laser sintering process. The design parameters of the burner element are listed in Table 2.1. The burner array employs a counter-rotating vortex pattern to improve flame-to-flame interactions. Each mesoscale burner element consists of a bluff body along with two tangential inlets that produce a swirling flow; thus, these inlets apply a center recirculation zone on the bluff body. The burner array produces uniform mesoscale flames that are less susceptible to combustion instabilities while achieving better performance than those of large scale burners.

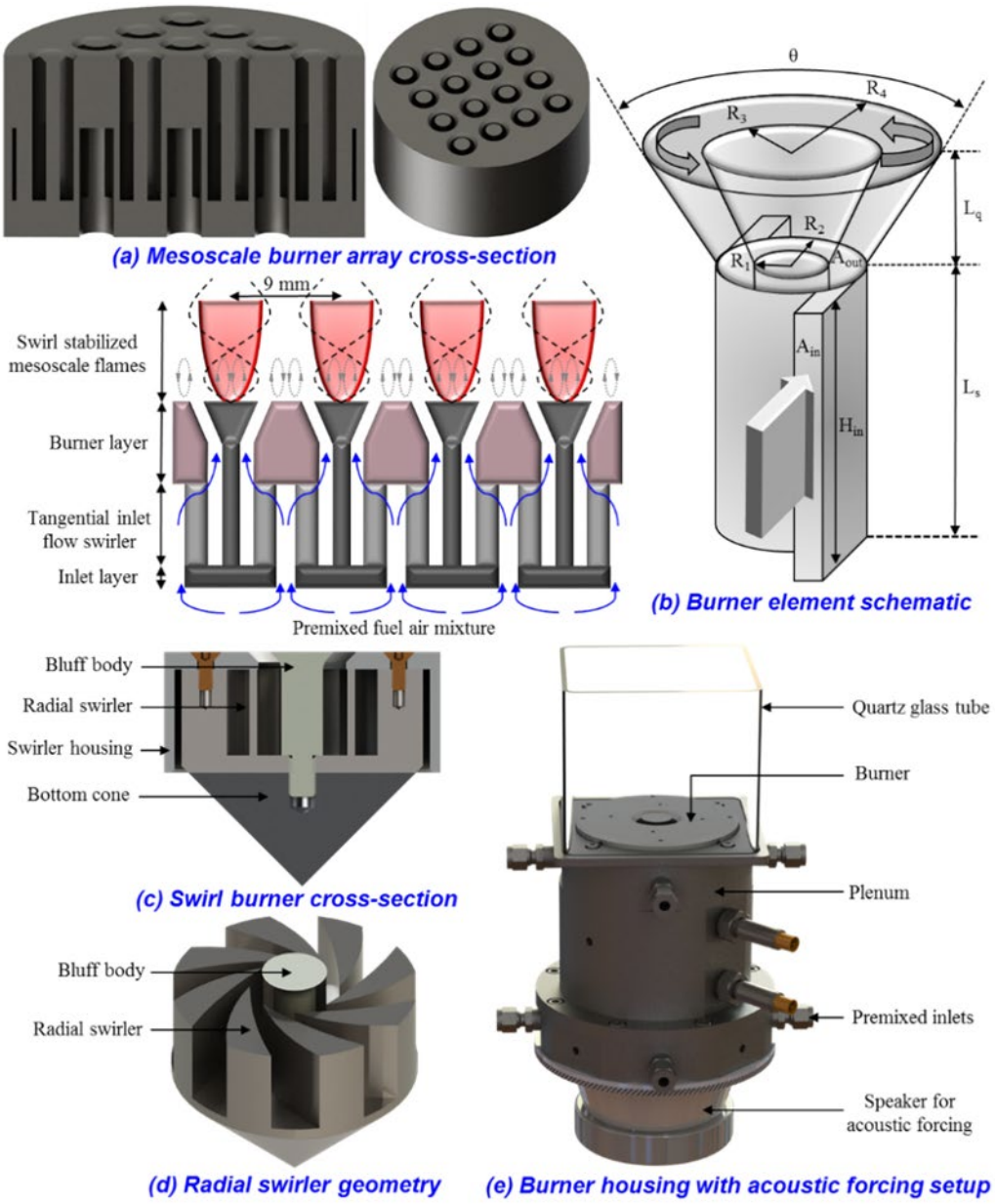

Figure 2.1. Schematic layout of (a) and (b) the mesoscale burner array, (c) and (d) the single (radial) swirl burner and (e) the burner housing.

Part	Parameter	Value
Mesoscale burner element	Quarl angle θ (degrees)	45
	Quarl length L_q (mm)	1
	Cylindrical post radius R_1 (mm)	1
	Swirler length L_s (mm)	19
	Cylindrical chamber radius R_2 (mm)	3
	Bluff body radius R_3 (mm)	2
	Quarl radius R_4 (mm)	3.75
	Swirl injector length H_{in} (mm)	19
	Inlet area A_{in} (mm^2)	15
	Outlet area A_{out} (mm^2)	27.5

Table 2.1. Design parameters for the mesoscale burner element.

The combustion characteristics of the mesoscale burner array are compared to those of a single swirl burner as a suitable benchmark. Modern gas turbine combustors employ a swirl-stabilized flame as a means of extending the stable burner operating range. As shown in Figure 2.1 (c) and (d), the single swirl burner employs a radial swirler equipped with eight curved vanes at a 60^0 angle and a central conical bluff body with a diameter of 12 mm. For the comparative study, the outlet area of the single swirl burner is equal to the total outlet area of the mesoscale burner array.

As shown in Figure 2.1 (e), the combustor housing is designed to test both burners and to provide identical upstream geometric and flow conditions. This design ensures that the observed flame characteristics are due to the differences in the flame stabilization mechanism. The burner housing has a diameter of 100 mm and a length of 75 mm, and the air/fuel inlets and flow straightener plate are located upstream. Mass flow controllers (MKS Instruments) are used to independently feed the reactants (air and methane) into the housing of the mesoscale burner array

at 1 atm and 300 K. To study the flame forcing responses, a speaker is installed upstream of the plenum in order to perturb the upstream flow. The premixed fuel-air mixture is also introduced here. The mesoscale burner array or the single swirl burner is installed at the downstream end of the chamber. A quartz tube with a length of 100 mm and a cross-sectional area of 100×100 mm^2 is placed over the burner housing to provide optical access for laser diagnostics.

2.2.2. Diagnostics

Flame temperature measurements were conducted using an R-type thermocouple (Nordic Sensors) with a bead diameter of 0.875 mm. This was mounted on a translational stage to allow accurate positioning above the burner array. The temperature signal was obtained using the cold-junction compensated NI DAQ system at 10 kHz and the resulting data were averaged over 60 s to obtain the steady-state temperature. The raw temperature measurements were corrected for thermocouple bead radiation losses using convection-radiation energy balance.

The combustion products were analyzed using a gas chromatograph equipped with a mass spectrograph (GC-MS) with helium as the carrier gas. The exhaust gas from the combustor was fed into the GC-MS system via a gas sampling unit. A HP-Plot U column was used to analyze CO_2 from the exhaust gas.

In addition, NO_x measurements were made using a Cerex Micro-Hound multi-gas analyzer. This relies on ultra-violet (UV) differential optical absorption spectroscopy (UV-DOAS), where the UV beam is directed through the gas sample and analyzed in a high-resolution miniature spectrometer. The minimum detection limit of the analyzer was 116 parts per billion (ppb) of NO.

2.2.3. Laser diagnostics setup

A layout of the OH and CH_2O-PLIF imaging setup is shown schematically in Figure 2.2. The OH-PLIF imaging was performed using the second harmonic output (532 nm, 500 mJ/pulse) of an Nd: YAG laser (Spectra Physics, Quanta-Ray PRO-250) as a pumping source to a dye laser (Sirah Lasertechnik, PRSC-D-24) at a repetition rate of 10 Hz. The dye laser was operated using DCM dye dissolved in ethanol. The pumped laser beam at a peak wavelength at 627 nm was frequency-doubled using a doubling crystal, then turned to ~ 310.60 nm to excite the $Q_1(12)$ line of the $A^2\Sigma^+ - X^2\Pi$ (0,0) band of OH. The laser beam was formed into a 50 mm-high, 0.3 mm-thick laser sheet via sheet forming optics. The OH fluorescence was carefully separated from the visible flame luminosity and background scattering using two customized long pass filters (Semrock, AFRL-0002) [28] and a band pass filter (Semrock FF01-315/15-25) with a FWHM of 20 nm at 315 nm. The OH fluorescence was imaged using a UV lens (f/2.8 Sodern Cerco) and an intensified camera (Andor iStar intensified camera) with a 100 ns gate.

For the CH_2O-PLIF imaging, the third harmonic output beam (355 nm, 150mJ/pulse) of the Nd:YAG laser was used. For simultaneous OH and CH_2O-PLIF imaging, the 355 nm laser output beam was combined with the dye laser output beam using a beam combiner. The output beam was also expanded by using the same sheet forming optics. The 355 nm laser beam excited multiple rotational transitions from a CH_2O vibrational band [29-32]. A band pass filter with an FWHM of 50 nm and a center wavelength of 400 nm was used to isolate the broadband CH_2O fluorescence. The CH_2O fluorescence was captured using a Sodern Cerco UV lens (100 mm focal length, f/2.8) and a LaVision Imager Intense CCD camera coupled to a LaVision IRO image intensifier (gate = 100 ns).

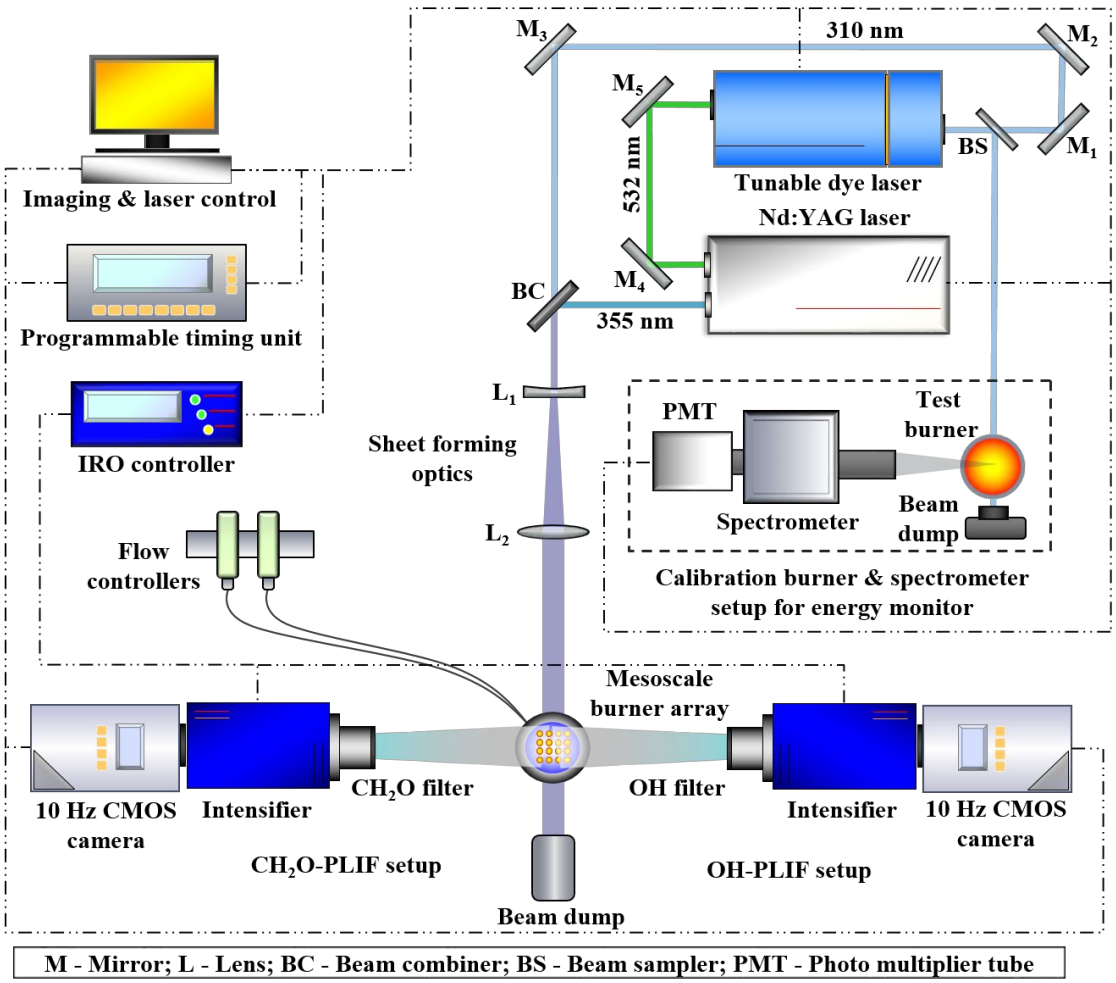

Figure 2.2. Schematic diagram of the 10 Hz simultaneous multispectral (CH_2O and OH) PLIF imaging setup.

2.3. Results and discussion

2.3.1. Multi-species imaging

The effect of the equivalence ratio upon flame stabilization in the mesoscale burner array was studied via simultaneous OH and CH_2O-PLIF imaging to identify the post combustion reaction zone (combustion product) and cool flame zone (reactant pre-heating region). Additionally, the concentration of HCO during the combustion reaction was considered as a good

indicator of the combustion heat release rate [33]. However, because the electronic transition of HCO is pre-dissociative, the combustion heat release rate was estimated via OH × CH_2O rather than HCO [34, 35]. Thus, the averaged OH, CH_2O, and heat release rate (OH × CH_2O) images of the mesoscale flame arrays for equivalence ratios ranging from 0.554 to 1.278 are presented in Figure 2.3. The OH and CH_2O images were obtained simultaneously, and the heat release rate images were visualized via pixel-by-pixel multiplication of the OH and CH_2O intensities. These images clearly reveal the presence of multiple structural regimes depending upon the equivalence ratio.

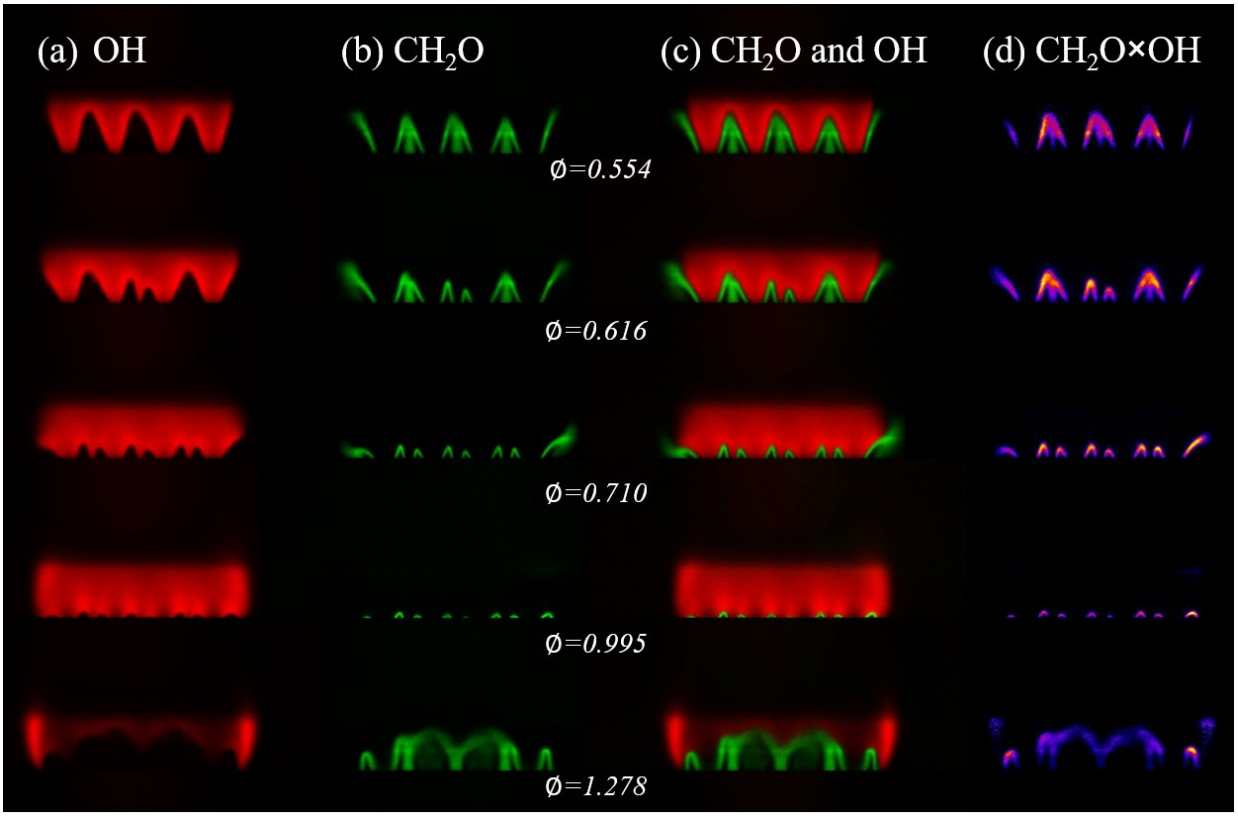

Figure 2.3. Simultaneous OH and CH_2O-PLIF images in the mesoscale burner array (averaged over 100 frames): *(a) OH, (b) CH_2O, (c) paired CH_2O and OH-PLIF, and (d) the estimated heat release rate by multiplication of the CH_2O and OH-PLIF images at an air flowrate of 20 SLPM.*

The flame structure is clearly visualized by the OH-PLIF images in Figure 2.3 (a). The mesoscale flame structures exhibit two major types, namely V-shaped and M-shaped, and are strictly dependent upon the operating conditions. Thus, at an equivalence ratio of 0.554, the mesoscale flame array exhibits a stable V-shaped swirling flame structure. With increasing fuel concentration, however, this V-shaped flame structure begins to transform into the M-shaped structure. This V- to M-shape transition of the flame structure is known to be due to the increased flame burning speed [36, 37]. Finally, at an equivalence ratio of 1.278, a merged flame is formed on the burner array due to the presence of excess unburnt fuel and a reduced flame speed.

The pre-heating zones of the mesoscale flame arrays are shown in Figure 2.3 (b). Here, the CH_2O layer reveals the reactant interactions in the burner array. Thus, the merging of the CH_2O layer in the flame interaction region demonstrates that reactant interactions occur at equivalence ratios of 0.554 and 0.616. With increasing equivalence ratio, however, the CH_2O layer close to the flame merging region begins to separate due to the V- to M-shaped flame transition. The flame transition is attributed to strong flame-to-flame interactions, thus inducing a shrunken CH_2O zone due to increased flame speed and burning temperature [38]. At an equivalence ratio of 1.278, the CH_2O layers merge and exhibit a thickened pre-heating zone that prevents individual flame-to-flame interactions and swirl stabilization on the bluff body.

The combined OH and CH_2O images and the calculated heat release images are presented in Figure 2.3 (c) and (d), respectively. With increasing equivalence ratio, the combustion reaction length is dramatically reduced from $\phi = 0.554$ to $\phi = 0.995$ as observed in the smaller heat release regions. Moreover, at an equivalence ratio of 1.278, the heat release reaction occurs further downstream without any flame stabilization on the bluff body. The overall flame phenomenology

observed in Figure 2.3 demonstrates that the mesoscale burner array has favorable operation capabilities under lean fuel conditions, thus resulting in strong flame-to-flame interactions.

2.3.2. Lean-blow off limit

The lean blow off limits of the mesoscale burner array and the single swirl burner under premixed operating conditions are shown in Figure 2.4. Power output is normalized by the burner exit area (power flux, MW/m^2). The LBO limit is evaluated by decreasing the fuel flow rate while holding the air flow rate constant.

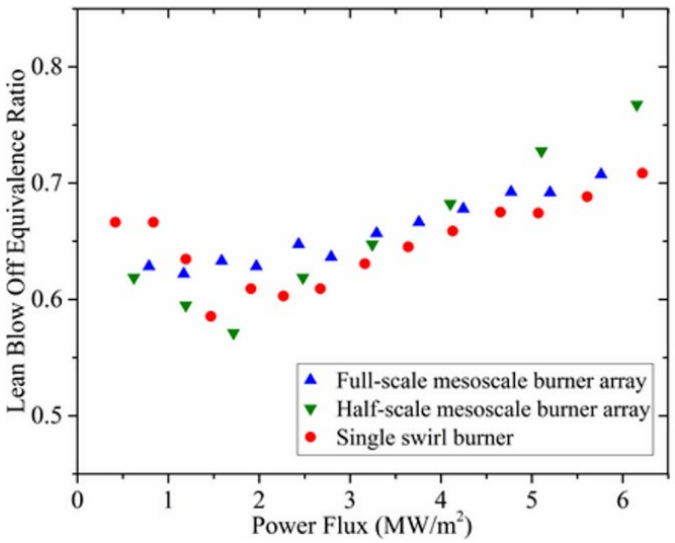

Figure 2.4. Lean blow off limit for two mesoscale burners and the single swirl burner at various burner power flux (MW/m^2).

As equivalence ratio decreases, flames begin to lift off one by one until all the flames were completely lifted from the bluff body. The first lift off invariably sets in on one of the edge elements as they were most prone to external disturbances such as rapid outside air entrainment

and heat loss. Coupled with decreasing flame speed, flame lift off propagates across the mesoscale burner array. Conversely, as flow conditions were gradually reverted to a more stable operating condition, the flame self-propagated across the entire array due to the counter rotating vortex pattern. A single solitary flame always relit all the burner elements through cross burner flow interaction, demonstrating that the flames are mutually supported by one another.

Results in Figure 2.4 show that the full-scale mesoscale burner array can sustain ultra-lean premixed flames ($\phi < 0.7$) over a wide range of burner power outputs similar to the single swirl burner. A second, half-scale, mesoscale burner was also tested and exhibited very similar lean blow off characteristics. This indicates that the full-scale mesoscale burner array is yet to be limited by microscale combustion instability phenomena and can be scaled down without significant performance degradation for a more compact burner design. On the other end of the spectrum, higher power output can be obtained by adding more elements to the existing mesoscale architecture. This will enable a more stable flame as the ratio of central and edge burner elements increases.

2.3.3. Flame temperature

Two temperature measurements were made to evaluate the thermal performance of the two burners. First, maximum temperatures at the flame surface under various lean equivalence ratio are shown in Figure 2.5 (a). All temperature measurements were corrected using convection-radiation energy balance for radiation losses. Maximum temperatures of the mesoscale burner array agree very well with adiabatic flame temperature. Stronger flame-to-flame interactions in the mesoscale burner array may likely raise the overall thermal conversion efficiency to exceed that

of the single swirl burner since interactions across identical flames can increase total heat release rate by 30% over an isolated flame [39].

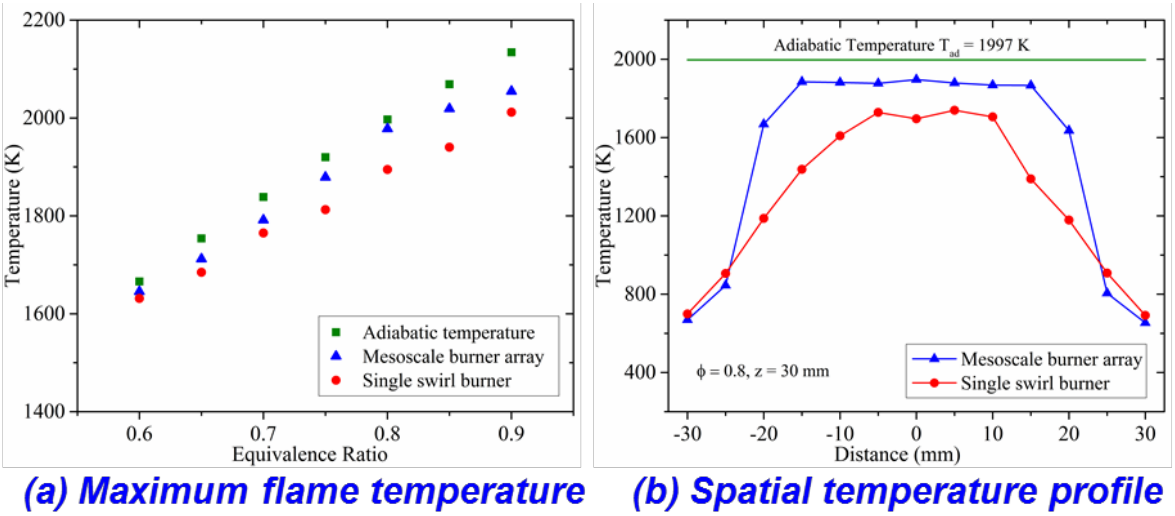

Figure 2.5. (a) Maximum flame temperatures of the mesoscale burner array and single swirl burner at various equivalence ratio. CH_4/air mixture, 30 SLPM. (b) Temperature profile along the burner centerline: CH_4/air mixture, 30 SLPM, ϕ = 0.8, 30 mm above the burner surface.

Second, spatial temperature profiles along the burner centerline are presented in Figure 2.5 (b). Spatially-resolved temperature profiles can be very useful in determining combustion uniformity. Temperature variation in the mesoscale burner array is less than 0.5% across the central elements (-15 to + 15 mm). The dotted line in the figure indicates the adiabatic flame temperature at ϕ = 0.8 (1996.9 K). The mesoscale burner array prevents heat loss through flame interactions within the thin reaction layers, thereby generating high temperatures very close to the adiabatic flame temperature. The temperature drop at the burner edge is likely due to the combination of heat loss and cold air entrainment. Temperature profile across the single swirl burner was much

less uniform and lower than that of the mesoscale burner array. Low thermal output of the single swirl burner may be attributed to its larger flame front volume as shown in Figure 2.6, since heat loss is proportional to volumetric size and flame stretch.

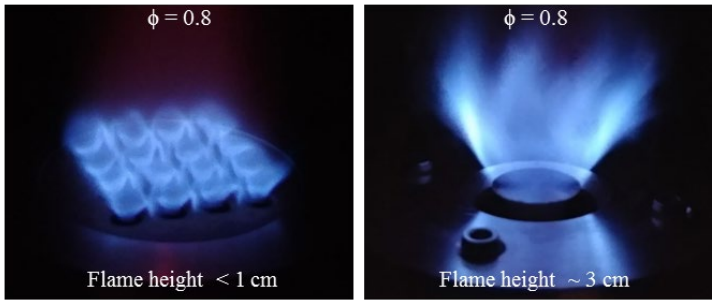

Figure 2.6. Visible flame emission, CH_4/air mixture, 30 SLPM, $\phi = 0.8$ in (a) mesoscale burner array; (b) single swirl flame.

2.3.4. Emissions

Carbon dioxide (CO_2) concentrations were measured using a GC/MS to quantify combustion efficiency. A TIC of the mesoscale burner array combustion products such as air, CO_2 CO, CH_4, and H_2O, was detected and identified against the NIST database as shown in Figure 2.7 (a). Measurements showed that CH_4 and CO mass fractions in the mesoscale burner array were less than 0.1% under lean premixed operating conditions [24].

To provide maximum contrast between the two burners, CO_2 was used to evaluate chemical conversion efficiency. Results given in Figure 2.7 (b), show that mesoscale burner array CO_2 emissions are roughly 13% higher than those of the single swirl burner. This is possibly due to stronger flame interactions reducing heat loss in the mesoscale burner array. Also, each bluff body recirculation zone acts as flame stabilizer, creating a dense combustion zone and accelerating

hydrocarbon conversion. On the other hand, overall lower temperatures in the single swirl burner are insufficient for completing the oxidation process on short time scales.

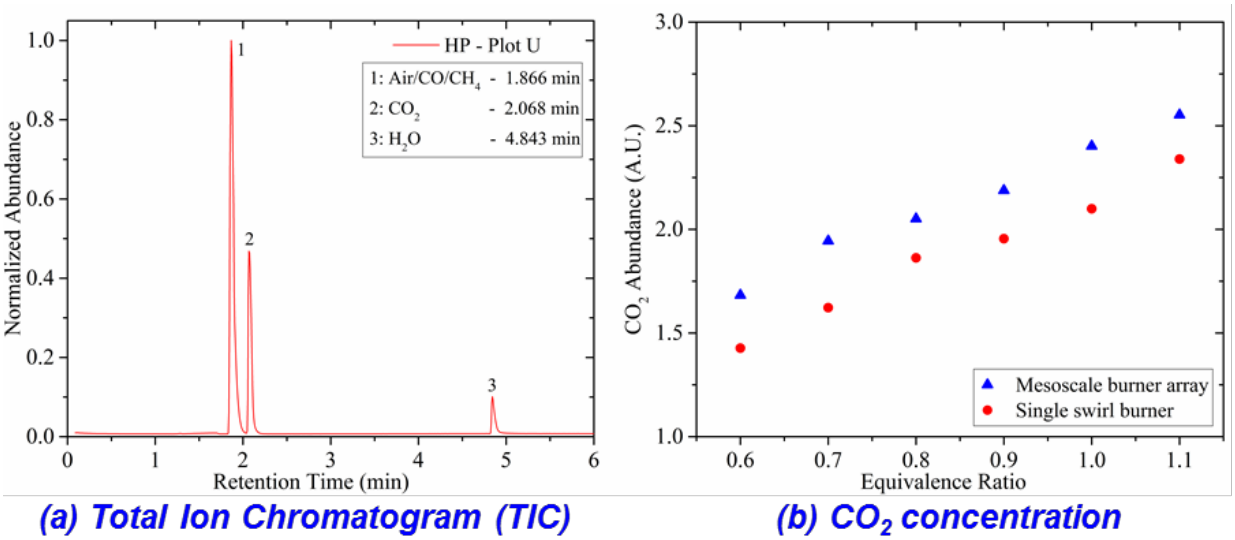

Figure 2.7. (a) Total ion chromatogram spectrum for CO_2 separation on the mesoscale burner array, ϕ = 0.8, 30 SLPM. (b) Comparison of CO_2 concentration between two burners at various equivalence ratios, premixed CH_4/air, 30 SLPM.

Next, nitric oxide (NO) emissions were measured in both burners to understand the effects of flame-to-flame interactions on NO concentration. NO and NO_2 (or NO_x) formation during combustion is largely driven by the Zeldovich mechanism (thermal NO_x) [40], which is highly temperature dependent. NO_2 in fully premixed methane combustion is negligible as its contribution is limited to about 1-2 ppm [41]. Results in Figure 2.8 (a) clearly show two distinct regimes. For lean mixtures below ϕ = 0.75, both burners produce similar amounts of NO since the Zeldovich mechanism is not significant when the overall gas temperature is low [41]. At higher equivalence

ratios, however, slightly higher temperatures in the mesoscale burner array drive up NO concentrations much faster than the single swirl burner.

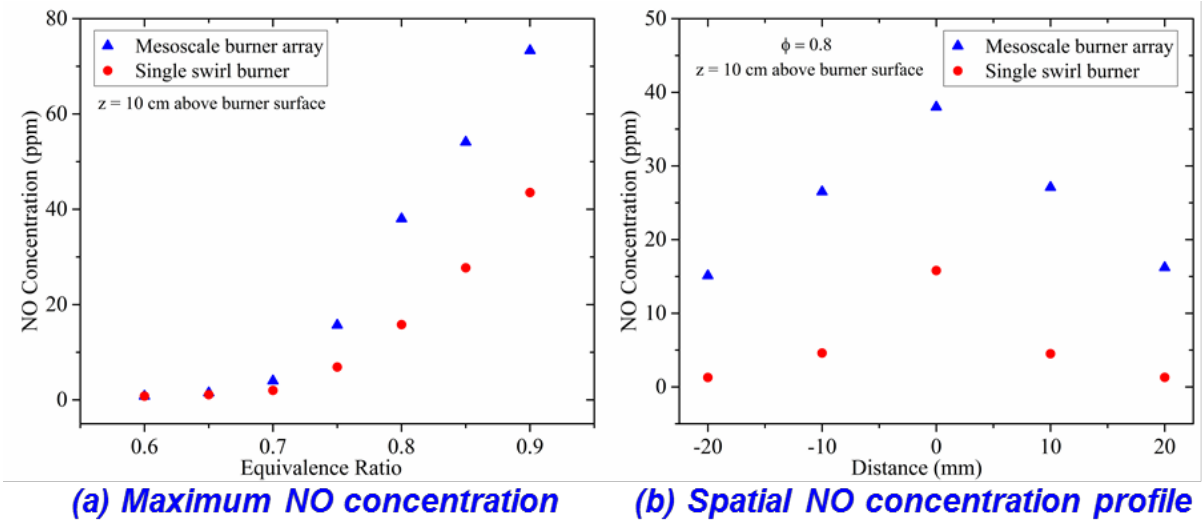

Figure 2.8. (a) NO concentrations for various equivalence ratio in the mesoscale burner array and single swirl burner, CH_4/air, 30 SLPM; (b) NO distribution along both burner centerline, CH_4/air, ϕ = 0.8, 30 SLPM, 10 cm above burner surface.

Spatial NO concentration measurements across the centerline of both burners are shown in Figure 2.8 (b). NO_x emissions from lean premixed CH_4/air flames ($\phi = 0.8$) were probed at a height of 10cm from the burner surface. Results show that the highest NO concentration was detected at the burner center for both burners. Inhomogeneous NO generation across the mesoscale burner array surface may be due to extreme temperature sensitivity of the thermal NO_x mechanism. On average, the mesoscale burner array generated around 20 more ppm of NO than that of the single swirl burner. This is possibly due to smaller and densely packed flame front volume in the mesoscale burner array increasing the high temperature region.

2.4. Conclusions

A mesoscale burner array designed to enhance combustion stability was experimentally investigated using several diagnostic and analysis techniques. Multi-species (OH and CH_2O) PLIF images showed flame-to-flame interactions with adjacent elements and identified their effect on flame stability and phenomenology. The interactions also minimized heat loss and improved combustion efficiency. Flame interactions are an important aspect of the mesoscale combustion array that affect its chemical and physical characteristics. Emission and lean blow off limit measurements demonstrated high combustion efficiencies in the mesoscale burner array. The maximum mesoscale burner array flame temperature was around 50 K higher than that of the single swirl flame and agreed very well with adiabatic flame temperature. Uniform spatial temperature distribution across the mesoscale burner array surface also indicates improved combustion performance. We expect that this design allows the mesoscale burner array to flexibly scale to accommodate a wide range of combustor power requirements by expanding the array size. Furthermore, we expect the efficiency, performance, and stability benefits of the mesoscale burner array to improve with further development and may potentially be implemented in future small-scale energy applications.

CHAPTER 3. DEVELOPMENT AND CHARACTERIZATION OF SWIRL-STABILIZED DIFFUSION MESOSCALE BURNER ARRAY

A diffusion mesoscale burner array with integrated fuel manifold and injection holes has been developed for compact and efficient propulsion and power systems. Each burner element is equipped with its own fuel injection holes built into its swirl-inducing geometry to improve flame interaction and reduce flame length. The diffusion mesoscale burner array provides comparable performance to a premixed mesoscale burner array under similar operating conditions despite fuel unpremixedness. Overall, diffusion flames on the mesoscale burner array exhibit 7.8% lower global equivalence ratios at lean blow-off conditions compared to premixed flames. Imaging of two primary combustion intermediates, OH and CH_2O, is carried out using planar laser-induced fluorescence to visualize the post- and pre-combustion zones of diffusion and premixed flames. Simultaneous 10 kHz high-speed OH fluorescence images and pressure measurements are used to study flame response and stability under external acoustic perturbation at a frequency of 200 Hz. OH fluorescence images show higher heat release and flame front fluctuations for diffusion flames. Rayleigh index reveals similar thermo-acoustic stability characteristics between diffusion and premixed flames. However, diffusion mesoscale flames exhibit large flame surface variation under external acoustic perturbation by spectral proper orthogonal decomposition analysis.

3.1. Introduction

One of the major design goals of a modern gas-turbine combustor is maximizing combustion efficiency while minimizing emissions. To that end, gas-turbine engines are engineered to operate under ultra-lean premixed conditions close to lean blow-off limits since the resulting lower combustion temperature reduces NO_x emission [16, 42]. However, gas-turbine combustors may be more susceptible to combustion instabilities under ultra-lean operating conditions. Combustion instabilities are self-sustaining flame oscillations near the combustor system resonance frequency due to closed loop coupling between unsteady heat release and pressure fluctuations (thermo-acoustic coupling) [17, 43]. These instabilities may cause significant mechanical vibrations and induce combustor failure and engine damage, a critical concern for both aircraft and land-based combustion systems [18, 44].

In addition to combustion instabilities in fuel lean combustion, typical gas-turbine combustors have employed large swirl flames to increase reactant residence time and thereby enhance combustion performance under ultra-lean operating conditions. Swirl-stabilized combustor requires large swirl flow-inducing components and a relatively long combustion chamber. However, the increase in the overall weight and size of the turbine may reduce its overall performance and efficiency. In response, a multi-burner array system that utilizes flame-to-flame interactions [45-48] has been developed for application in low NOx gas turbine combustors. These systems can be scaled down to the mesoscale, further reducing the overall combustor dimensions, yet maintaining its stable operating characteristics. An additional benefit of multi-burner arrays includes higher degree of controllability for mitigating combustion instability [49]. As a result, scalable mesoscale burner arrays driven by flame-to-flame interactions [24, 50] have been demonstrated in recent history for their potential use in high-power, small-scale combustion

systems [1, 51]. These mesoscale burner arrays are designed to be relatively insusceptible to thermal and chemical quenching in small flames [3-5].

The mesoscale burner array in this study is made up of independent burner elements arranged in a counter-rotating Taylor-Green vortex arrangement. This configuration allows neighboring swirl flows to interact with one another. Flame interactions between mesoscale flames reduce the outer recirculation zone with minimal performance degradation thereby effectively reducing the combustor length and weight [24]. These improvements have little to no negative impact on burner power output and emission characteristics (NOx, CO, etc.) as a similarly sized single swirl burner [52]. However, shorter reactants residence time due to smaller combustor dimensions may reduce and negatively impact air-fuel mixing characteristics in diffusion flames. This can also result in shorter chemical reaction time scale and unsteady combustion dynamics. Furthermore, insufficient heat generation and unsteady flame dynamics due to inadequate fuel mixing may result in unstable and non-optimal burner performance such as flame extinction, insufficient heat generation, and unstable mode inside the combustor [20, 22, 53]. Despite these issues, employing diffusion flame stabilization in mesoscale burners has a major advantage. Flame flashback, a phenomenon that induces serious safety issues and burner system failures, can be prevented via diffusion fuel injection [54, 55]. Furthermore, the elimination of additional mixing chamber can yield more flexible design capability, an important consideration when considering small scale burner applications. Therefore, understanding and addressing the shorter air-fuel mixing characteristics is critical for successfully implementing diffusion mesoscale burner arrays in small-scale unmanned aerial systems (UAS) and portable power generation systems [6]. Mesoscale diffusion burner arrays can provide significant weight reduction, enhance design

flexibility, and improve gas turbine aspect ratio (compactness) while providing enough power to potentially replace batteries in aforementioned high-powered compact systems.

In this work, a diffusion mesoscale burner array is designed and characterized. Each diffusion burner element in the array has twenty-four 250 μm fuel injection holes integrated into its geometry. These holes are designed to enhance fuel mixing and flame stabilization in a mesoscale burner element. The diffusion mesoscale burner array performance is examined by analyzing its lean blow-off limits and temperature profiles. Premixed and diffusion operations on the diffusion mesoscale burner array are visualized and analyzed using OH and CH_2O-PLIF diagnostics. Thermo-acoustic instabilities under externally imposed acoustic perturbation are also studied. The effect of fuel mixedness on flame dynamics is analyzed by using frequency-driven Rayleigh index and spectral proper orthogonal decomposition (SPOD).

3.2. Experimental setup

3.2.1. Burner element design

Premixed methane and high-vapor pressure liquid fuel flames on the 4×4 mesoscale burner array have been extensively studied using a suite of optical and laser diagnostics as well as combustion stability analyses in our previous works [24, 56]. The schematic layout of the diffusion mesoscale burner array element and its bluff body is presented in Figure 3.1. Their major design parameters are given in Table 3.1. Each burner element in the diffusion mesoscale burner array is equipped with two rows of 12 radial fuel injection holes (total of 24 holes) as shown in Figure 3.1 (b). The 250 μm diameter injection hole is machined using EDM (electrical discharge machining). Four tangential inlets surrounding the bluff body create a swirling flow field for flame stabilization. For diffusion flames, fuel and air are injected via injection holes and tangential inlets, respectively.

For premixed flames, the air-fuel mixture is supplied through the four tangential inlets. A diverging quarl is provided at the burner exit to improve the strength of the central recirculation zone (CRZ) thereby enhancing reactant and product mixing. Individual burner elements of the mesoscale burner array are arranged in counter rotating vortex pattern (Taylor-Green vortex arrangement) to improve flame stabilization and enhance flame interactions with neighboring elements.

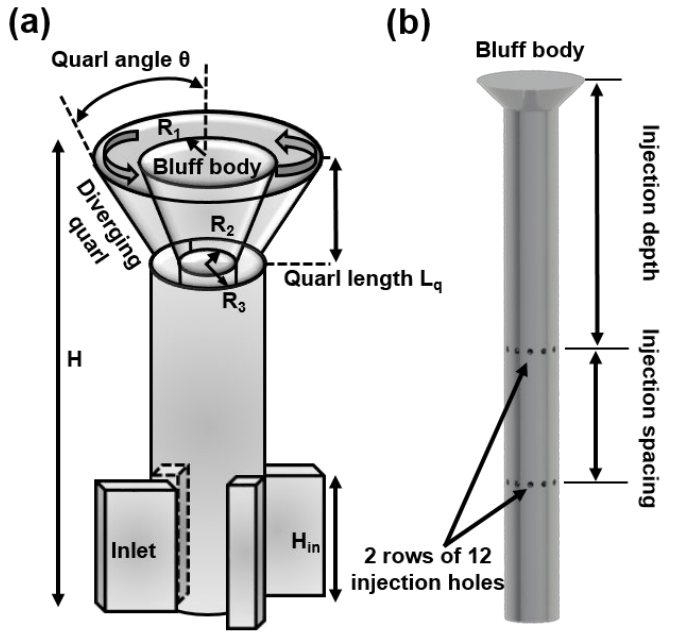

Figure 3.1. Schematic layout of (a) a mesoscale diffusion burner array element and (b) its bluff body with integrated holes for fuel injection.

Parameter	Value
Quarl included angle θ (degrees)	45
Quarl length L_q (mm)	1
Bluff body radius R_1 (mm)	2
Cylindrical post radius R_2 (mm)	1
Cylindrical chamber radius R_3 (mm)	3
Burner element length H (mm)	20
Swirl injector length H_{in} (mm)	5
Injection depth (mm)	10
Injection spacing (mm)	5

Table 3.1. Design parameters for the diffusion mesoscale burner array.

Numerical simulations of an individual burner element in the diffusion mesoscale burner array are carried out to estimate the degree of fuel mixedness and the location of flame stabilization on the bluff body using Fluent 18.2 combustion model [57]. The simulations utilize methane and air as fuel and oxidizer respectively with a combined volumetric flowrate of 3 L/min. Based on the hydraulic diameter and axial bulk velocity upstream of the swirler, the corresponding Reynolds number is estimated to be 510. The methane fuel flowrate is set to a global fuel/air equivalence ratio of 0.8. Existing studies focused on simulations of micro/mesoscale combustion [58-61] have suggested that the k–ε turbulence model can be used for estimating combustion characteristics even in the laminar or transient regime characterized by low Reynolds number. Therefore, the k–ε turbulence model based on Reynolds-Averaged Navier–Stokes (RANS) is employed in the viscous flow model. Discrete ordinates (DO) radiation model is used to solve for the energy

equation. Species transport is modeled using the partially premixed combustion model. The mixture fraction and the reaction progress variable are solved to determine the species concentrations. The fuel and air input conditions are set to 1 bar and 300 K, respectively. A tetrahedral meshing scheme is created using an optimized non-uniform grid for computational fluid dynamics in Fluent 18.2. The total mesh grid number is set to around 3 million. The grid size dependency of the results is analyzed and verified. The simulated methane mass fraction distribution gives a good indication of the fuel mixedness and flame stabilization in the flow field.

A section view of the computational domain is shown in Figure 3.2 (a). Figure 3.2 (b) shows the axis-symmetric methane distributions under non-reactive and reactive conditions in diffusion and premixed burner configurations. In premixed condition, the methane mass fraction is 0.0445 at the equivalence ratio of 0.8. Under non-reactive diffusion condition, regions of high fuel mass fractions (rich premixed zone) are observed in the central recirculation zone (CRZ) created by the bluff body and swirl flow. Under reactive conditions, the fuel mass fraction is distributed predominantly in a wide V-shaped region with the highest concentration right above the burner exit. Both flames exhibit effectively a V-shape, which can potentially improve flame interaction in the mesoscale burner array. However, the methane mass fraction under diffusion fuel injection is more restricted to a thinner layer.

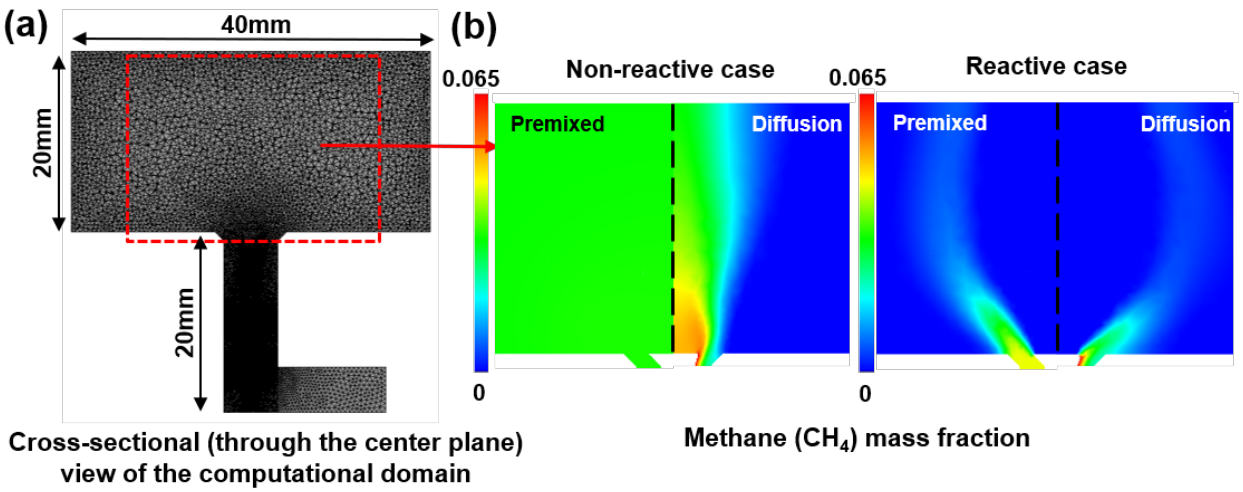

Figure 3.2. Numerical results of the mesoscale diffusion burner array element. (a) Section view of the computational domain with meshing. (b) Methane mass fractions under non-reactive and reactive environments.

3.2.2. Burner setup

The stainless steel 16-element mesoscale burner array is mounted onto a custom-designed burner housing and plenum chamber as shown in Figure 3.3. The fuel manifold is located below the burner elements and swirl structures. It is connected to 16 fuel feeding tubes that also double as the burner bluff body. The fuel manifold chamber is smaller than the diffusion mesoscale burner array so that the incoming gas is quickly fed into each burner element. In premixed combustion mode, the manifold chamber is closed, and the premixed air and fuel mixtures are injected in through the swirling geometry. The burner top down view in Figure 3.3 shows the 4×4 burner array with a center to center distance of 9 mm. The dotted lines on the mesoscale burner array in Figure 3.3 are the laser sheet paths for imaging diagnostics discussed later. This burner array adopted counter rotating vortex patterns, called Taylor-Green vortex array, which induces flame recovery over the entire burner array after initial ignition or under partial blow-off conditions. Air

and methane are supplied to the burner housing independently using mass flow controllers (MKS mass flow controller) (±1 % uncertainty) at 1 atm and 300 K. The maximum allowable flow rates for the mass flow controllers are 200 SLPM (air) and 5 SLPM (methane). A subwoofer (Dayton Audio) is attached at the bottom of the plenum to perturb the incoming flow. The amplitude and frequency are adjusted using a 1400 W power amplifier (Pyle Pro) and waveform generator (Agilent). Acoustic pressures are measured using a high temperature probe microphone (PCB Model 377B26) fitted with an ICP sensor signal conditioner (PCB Model 480B21). Temperature measurements are conducted using a type R (platinum – platinum 13 %, rhodium) high temperature thermocouple probe (Nordic Sensors) and corrected for radiation loss.

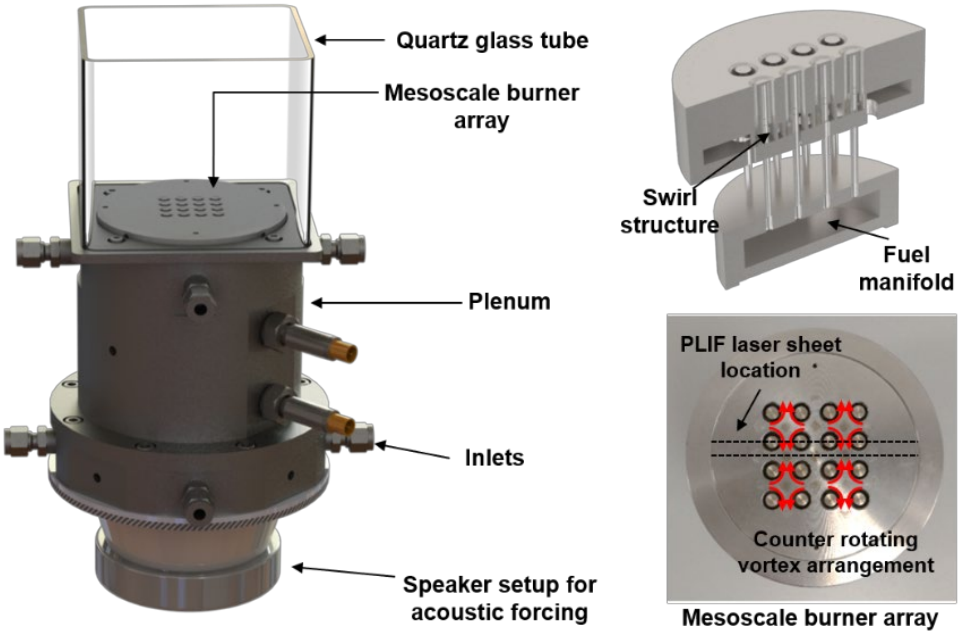

Figure 3.3. Burner housing with a speaker mounted upstream of the burner for inducing acoustic perturbations. Sectional view of the mesoscale diffusion burner array showing its internal geometry.

3.2.3. *Laser diagnostics setup*

A layout of PLIF imaging setup is shown in Figure 3.4. The 10 Hz OH and CH_2O-PLIF imaging used the second and third harmonic generation output from a Spectra Physics Quanta Ray Nd: YAG laser (532 and 355 nm) and a Sirah dye laser. The laser output from Sirah dye laser is precisely tuned to excite the $Q_1(12)$ line of the $A^2\Sigma^+$-$X^2\Pi$ (0, 0) band of OH at 310.60 nm [62, 63]. The UV output passes through sheet forming optics to form a thin laser sheet of thickness ~ 120 µm (FWHM). OH fluorescence is collected using an Andor iStar intensified (gate = 100 ns) CCD camera with Sodern Cerco UV lens (100 mm focal length and f/2.8). A long-wave-pass filter and a Schott UG-5 filter are used to remove scattering and visible emission from the flame.

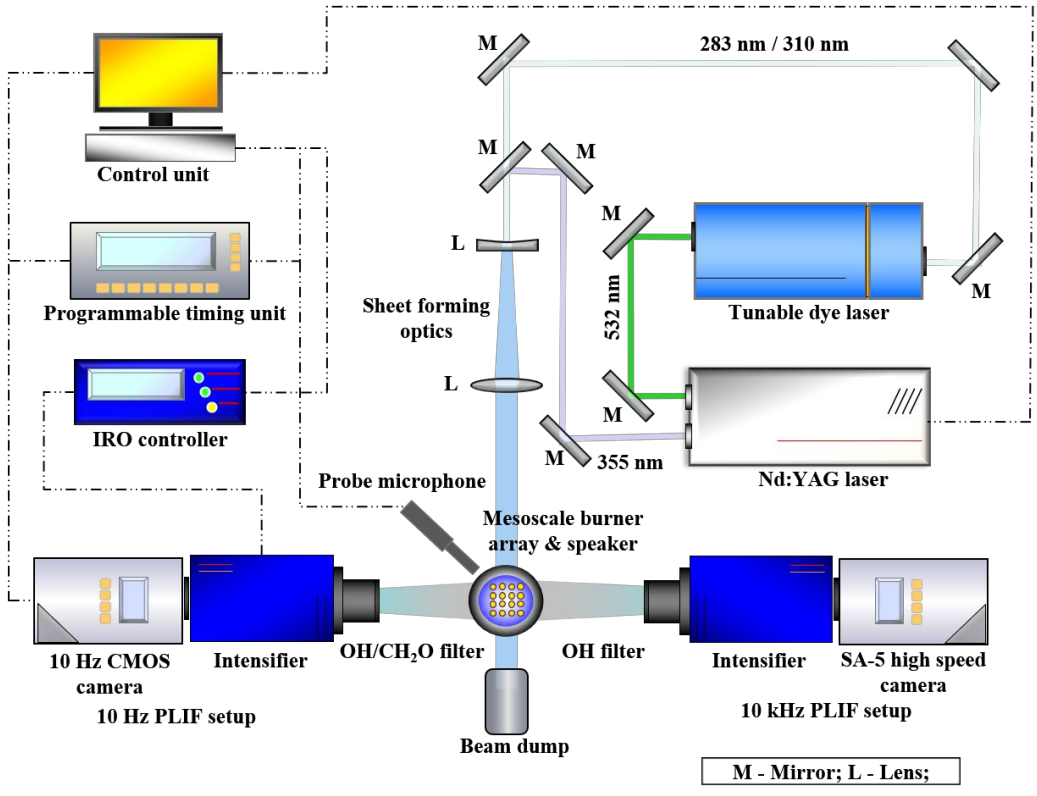

Figure 3.4. Schematic layout of the diagnostics setup for PLIF imaging and acoustic measurements.

The CH_2O (formaldehyde) PLIF is based on excitations of multiple rotational levels of a CH_2O vibrational band [29, 31]. CH_2O fluorescence, ranging from 375 to 425 nm, is collected using an Edmund Optics band pass filter (50 nm FWHM at 400 nm) and the same UV lens and CCD camera used for OH-PLIF. The 10 kHz OH-PLIF uses a diode pumped solid state Nd:YAG laser (EdgeWave Innoslab IS12II-E, maximum power: 60 W at a 532 nm) to pump a tunable Sirah CREDO dye laser with Rhodamine 6G dye solution for exciting the Q_1 (8) line of the $A^2\Sigma^+$-$X^2\Pi$ (1, 0) band of OH at approximately 283.5 nm. The output beam from the dye laser is formed into a laser sheet with sheet forming optics and passed through the flame. OH fluorescence is filtered through an Asahi narrow band pass filter (10 nm FWHM at 310 nm) to remove Rayleigh and other surface scattering. OH fluorescence is imaged with a Photron SA-5 CMOS camera, a Lavision image intensifier, and a 100 mm f/2.8 UV lens (Sodern Cerco).

3.3. Results and discussion

3.3.1. Mesoscale burner array operation

Visible images of premixed and diffusion flames on the diffusion mesoscale burner array, at a total flowrate of 48 L/min and an equivalence ratio of 0.8, are shown in Figure 3.5. The bulk axial velocity in the swirler is 1.99 m/s for each burner element. The geometric swirl number of this burner array is 0.75. This swirl number is similar to that of the mesoscale burner array used in our previous research [56], where mesoscale flame phenomenology by flame interaction such as V to M shaped flame transition was reported. For diffusion flames, however, flame structures are blurred possibly due to fuel mixedness variations giving rise to stronger flame fluctuations. However, flame merging and stabilization on the bluff body are observed in both the premixed and diffusion mode operation.

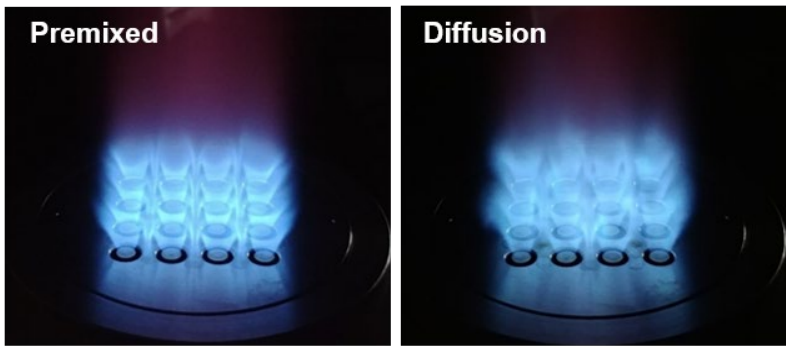

Figure 3.5. Images of premixed and diffusion flames in the mesoscale burner array.

3.3.2. Lean blow-off limit

The flame stability of the diffusion mesoscale burner array is analyzed by measuring lean blow-off limits at various thermal power outputs. In swirl-stabilized flames, the recirculation zone is an important factor for stable burner operation because blow-off is triggered when the flow time scale is insufficient for igniting the reactants [64, 65]. Flames start stretching and begin to lift off near the lean blow-off limit. Flames lift off sequentially starting from one of the edge elements due to excessive heat loss to the surroundings. The mesoscale burner array will eventually blow off completely as the equivalence ratio continues to decrease. The equivalence ratios of complete lean blow-off are shown as a function of the thermal power output in Figure 3.6. In both flame configurations, lean blow-off equivalence ratios increased slightly with thermal power output (as well as flowrate). This is partially due to the increased difficulty associated with sustaining reignition through combustion product recirculation. Lean blow-off equivalence ratios of diffusion flames are slightly lower than that of premixed flames. This is because diffusion fuel injection induces equivalence ratio stratification due to mixing resulting in the availability of locally rich premixed zones that are easy to ignite when compared to homogeneously lean premixed mixtures.

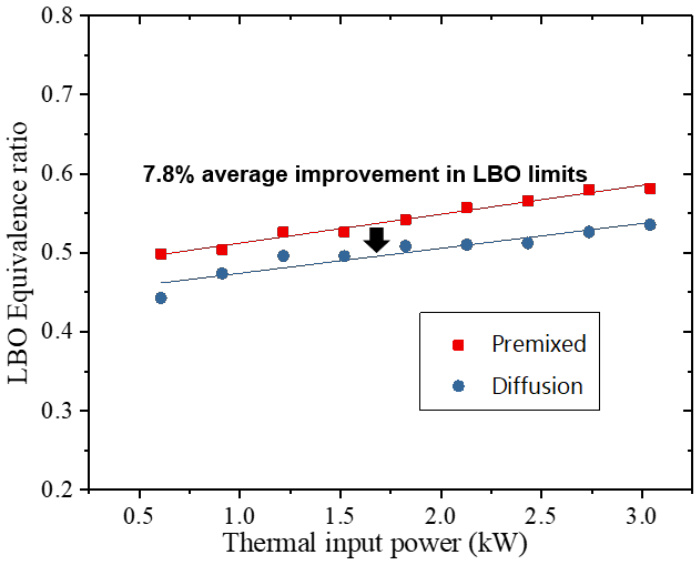

Figure 3.6. Lean blow-off (LBO) equivalence ratios of premixed and diffusion flames in the diffusion mesoscale burner array for varying thermal power outputs.

3.3.3. Temperature measurement

Spatial temperature profile measurements of premixed and diffusion flames are shown in Figure 3.7. These results can be used to evaluate the thermal performance of the diffusion mesoscale burner array. Temperature measurements are carried out at three different heights above the burner array surface and along the line depicted in Figure 3.7 (a). More uniform temperature distributions are observed under premixed flames than diffusion flames for all three conditions. Observed temperatures, on the other hand, are higher for diffusion flames (particularly around the burner array center) than premixed flames. Furthermore, diffusion flames show significant variation in axial temperature distribution with 1 cm from the burner surface being the hottest and progressively becoming colder further away from the burner surface as expected. Radial variations in the diffusion flame temperature distribution may be due to the differences in the local equivalence ratios. Flame temperature is the hottest in the burner array center and gradually

decreases toward the edges, possibly due to mixing with excess entrained air through the edge elements. Overall, the higher heat release near the diffusion flame center contributes to its non-uniform temperature profile. Higher diffusion flame temperatures near the burner center provide favorable environment for flame stabilization under fuel lean operation.

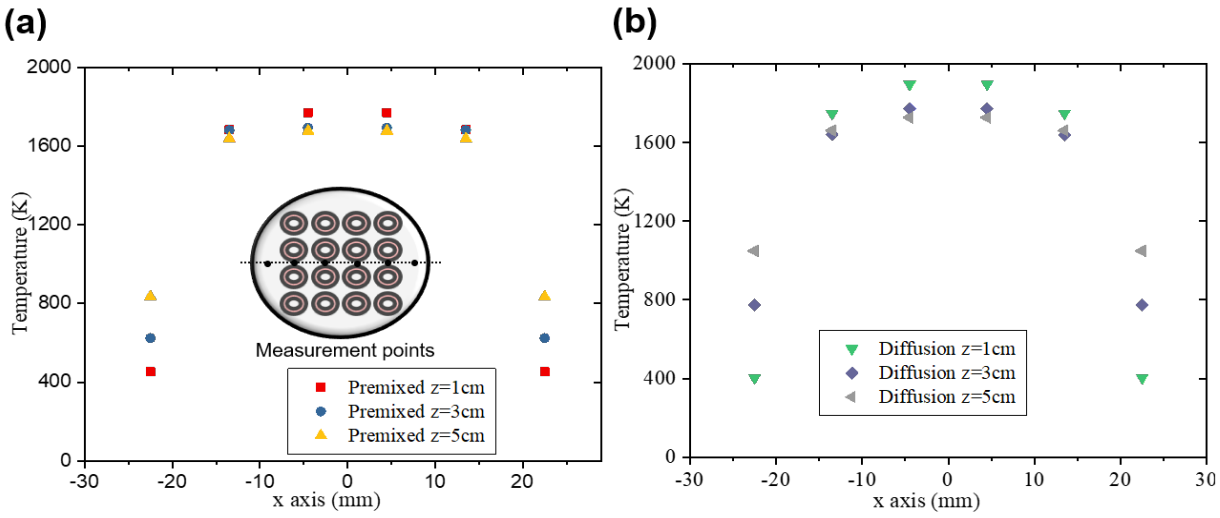

Figure 3.7. Spatial temperature distribution at various heights along the burner centerline for (a) premixed flames and (b) diffusion flames in the mesoscale burner array for ϕ = 0.8 (global) and total flow rate of 48 SLPM.

3.3.4. Flame visualization using OH and CH_2O-PLIF

Figure 3.8 (a) shows averaged OH-PLIF images of premixed and diffusion flames at various equivalence ratios ranging from 0.6 to 0.8. Optical diagnostics made along the centerline of the second row of burner elements is shown in Figure 3.3. These spatially resolved OH-PLIF images are ideal for visualizing the flame front. They can reveal mesoscale flame structures and interactions since OH is a good marker for heat release. Both premixed and diffusion flames exhibit

a typical V-shaped flame structure at $\phi = 0.6$. Flame merging between two center flame elements is observed near the burner surface. Under such fuel lean operating condition, the merging distance of the two center diffusion flames is shorter than that of the premixed flames because higher local equivalence ratio enhances flame interaction. As the equivalence ratio increases, the two center flames start to form M-shaped flame structures near the interaction region. The V- to M-shaped flame transition leads to a large reduction in flame lengths. Relatively weak flame interaction zone is only observed in the diffusion flame array at $\phi = 0.6$ and 0.7, possibly due to lower fuel concentration from fuel unmixedness. The weak interactions and the resulting irregular flame shapes in diffusion flames are partly attributed to variations in fuel flow rate from the fuel injection holes and manifold.

OH intensity profile 5 mm above the burner surface is extracted from Figure 3.8 (a) and is shown in Figure 3.8 (b). OH intensity peaks in premixed flames are located near the two shear layers of each burner. In diffusion flames, only a single peak near one of the shear layers is observed. Furthermore, OH profile of the diffusion flame shows an irregular OH concentration distribution across the four flame elements due to the uneven fuel concentration distribution along the measurement line.

Figure 3.8 (c) and (d) show instantaneous images of both flames. Pockets of unburnt reactants are observed near the flame merging zone in both premixed and diffusion flames. Premixed flames exhibit unstable fluctuations along the flame front due to inherent Kelvin-Helmholtz instability and flame interactions [66]. On the other hand, diffusion flames show much larger flame area change with bulk fluctuations due to rapid expansion of reactant gases between two center flames [67, 68]. Center flame interaction zone in diffusion flames shows flame roots

heading to the burner by the expanding reactants. As a result, V- to M-shaped flame transition can be triggered and the flame is stabilized as M-shaped flame at higher equivalence ratios.

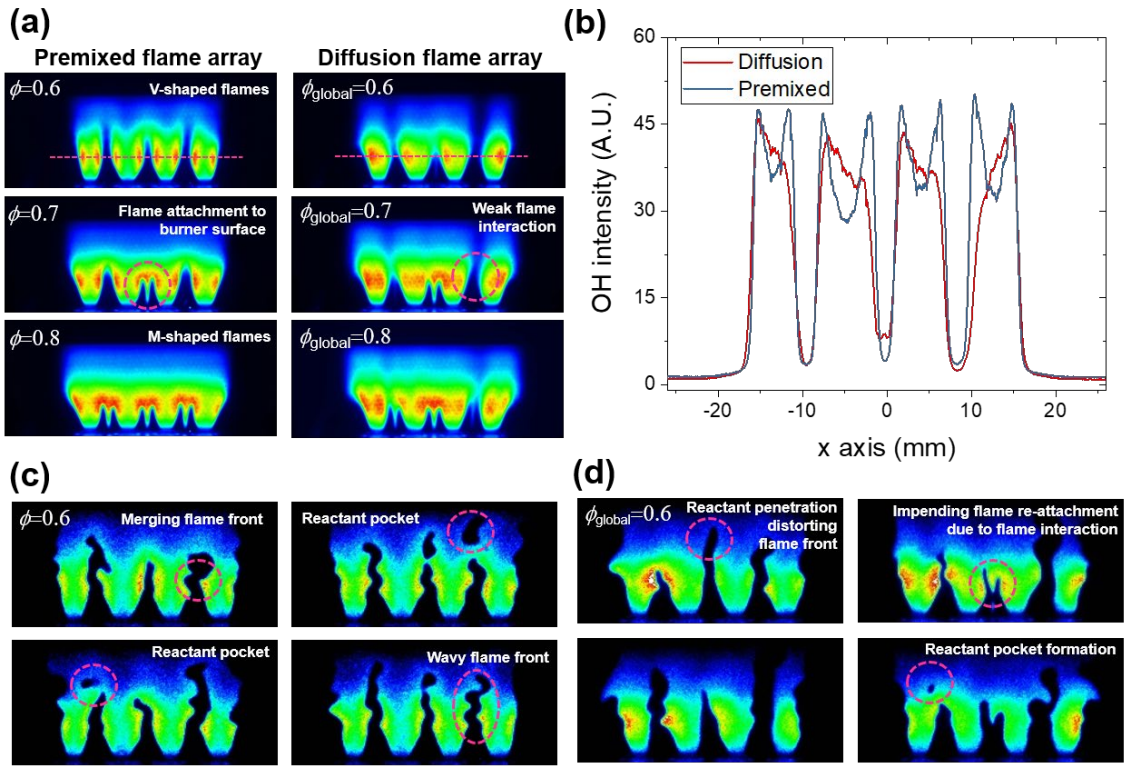

Figure 3.8. (a) Averaged OH-PLIF images (200 snapshots) of premixed and diffusion flames in the mesoscale burner array at a total flowrate of 48 SLPM; (b) Radial profile of OH intensities along the magenta dotted line in the averaged OH-PLIF images. Instantaneous OH-PLIF images of (c) premixed and (d) diffusion flames in the mesoscale burner array at ϕ = 0.6.

The fuel pre-heating zone is visualized using CH_2O-PLIF imaging for premixed and diffusion flames on the mesoscale burner array in Figure 3.9. CH_2O-PLIF images can also be used to determine the flame front location since CH_2O is consumed rapidly at the flame front in high-temperature heat release reactions [69]. CH_2O fluorescence presented in Figure 3.9 shows

reactants merging and separating in the flame interaction region at various equivalence ratios. CH_2O layer merging indicates direct reactant exchange in the interaction zone, that is observed in both flames at the lowest equivalence ratio ($\phi = 0.6$). At higher equivalence ratios, CH_2O layer separation is observed near the center interaction zone, triggering V- to M-shaped flame transitions as observed in the averaged OH-PLIF images (Figure 3.8, $\phi = 0.7$). CH_2O layer separation indicates product and heat exchange in the absence of reactants mixing. The formation of M-shaped flame is the direct result of increased flame interaction, the shrinking preheat zone due to decreasing CH_2O thickness in the high temperature laminar flame, and higher burning velocity [38]. The average CH_2O layer thicknesses in diffusion flames are thicker than those of premixed flames due to stronger flame fluctuations. Also, both flames exhibit thicker CH_2O layer outside the burner array perimeter, which may be partly attributed to turbulence fluctuations and instabilities.

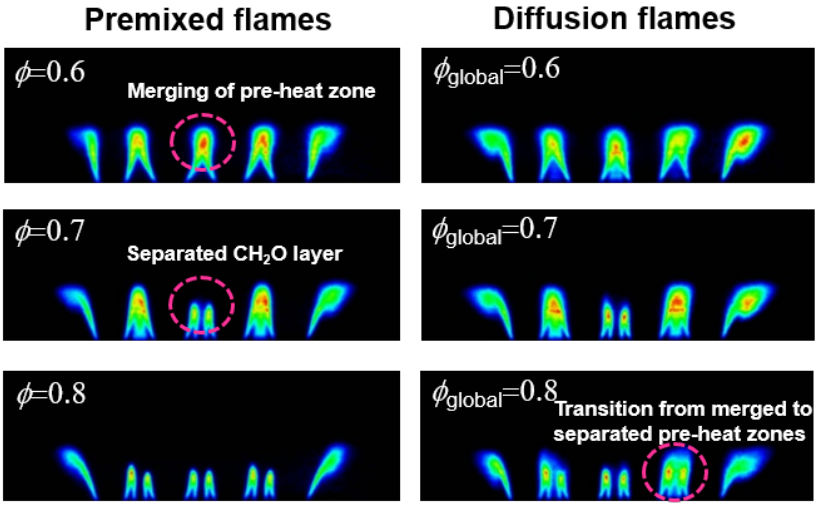

Figure 3.9. Averaged (200 snapshots) CH_2O-PLIF images of premixed and diffusion flames in the mesoscale burner array.

Figure 3.10 shows OH-PLIF images along the burner array centerline, between the second and the third row. They visualize the flame interactions between neighboring elements in the burner array center. At the lowest equivalence ratio ($\phi = 0.6$), lifted flame interactions are mainly observed above the burner surface for premixed and diffusion flames. Diffusion flames show center flames that are partially attached to the burner surface. Notably, premixed flames exhibit flame interactions that are concentrated in the burner array center whereas diffusion flames are spread out more evenly across the burner surface. At $\phi = 0.7$, both premixed and diffusion flames show attached flame interactions, similar to swirl-stabilized flames. As the equivalence ratio increases, the M-shape flame interaction in the burner array center drives the flame to the burner surface. This is observed in both premixed and diffusion flames. Images of the two flames at $\phi = 0.8$ are mostly similar with the exception of small interaction structures observed due to fuel unmixedness in diffusion flames.

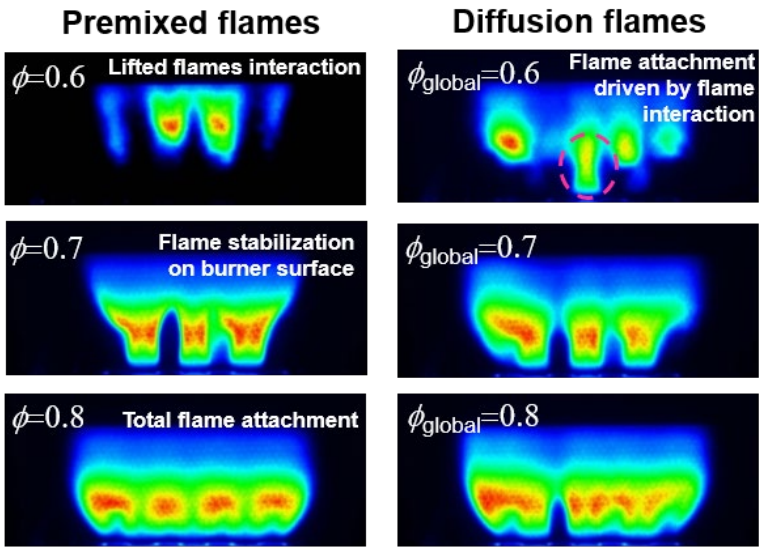

Figure 3.10. Averaged (200 snapshots) OH-PLIF images above the centerline of the mesoscale burner array (flame interaction plane).

3.3.5. Flame response to external forcing

Flame response at 200 Hz perturbation frequency is analyzed using 10 kHz OH-PLIF imaging. The laser sheet is passed through the centerline of the second row of flames in the mesoscale burner array. Acoustic pressures are measured at the flame position. The normalized pressure and heat release rate, calculated using OH-PLIF intensity at $\phi = 0.8$ and total flowrate = 48 SLPM, are shown in Figure 3.11. The pressure fluctuations and OH-PLIF images are captured simultaneously. The pressure fluctuations of both flames are similar, though diffusion flames exhibit larger heat release fluctuations compared to premixed flames. Additionally, the heat release response between premixed and diffusion flames exhibits a distinct phase difference of ~ 86º as shown in Figure 3.11 (b), possibly due to fuel injection schemes, which can affect the thermo-acoustic stability of the flames due to fuel stratification.

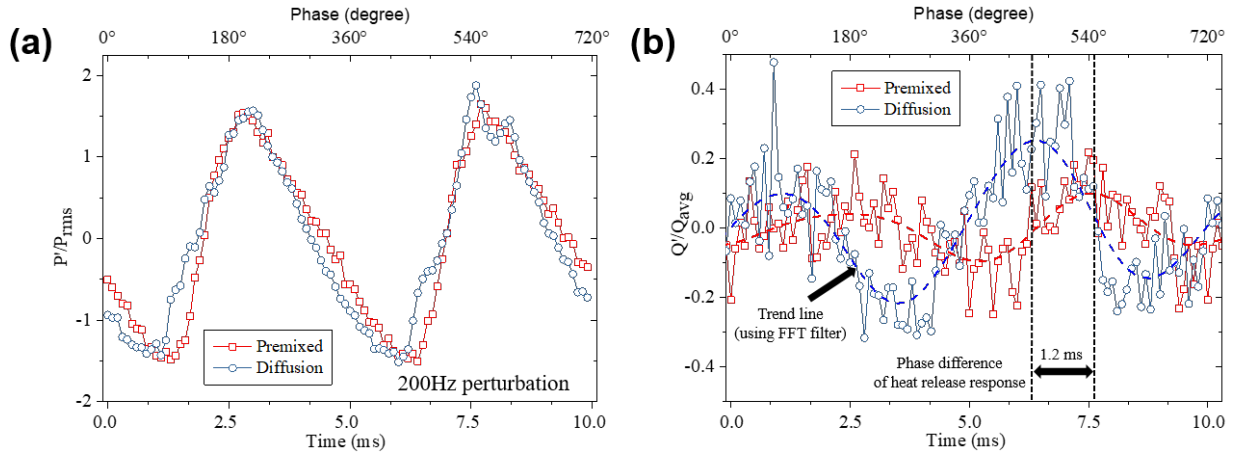

Figure 3.11. Simultaneous (a) pressure and (b) heat release fluctuation measurements due to external perturbation at 200 Hz.

Instantaneous OH-PLIF images of premixed and diffusion flames shown in Figure 3.12 highlight the important differences in the spatial heat release characteristics and flame interaction across one perturbation cycle. For premixed flames, all the interaction zones in the array show M-shaped flames that are either attached or located close to the burner. Flame front fluctuations due to swirl flow perturbation with small vortex roll up and flame interactions are observed without any significant change in the premixed flame structure. Diffusion flames fluctuate more significantly at the flame interaction zones, leading to flames merging higher above the burner array surface compared to the premixed flames. Furthermore, large flame surface stretching effects due to external perturbations are observed particularly in the edge flames in diffusion mode operation. These images indicate thermo-acoustic oscillations driven by fuel unmixedness can induce large flame area changes thereby resulting in higher heat release fluctuations.

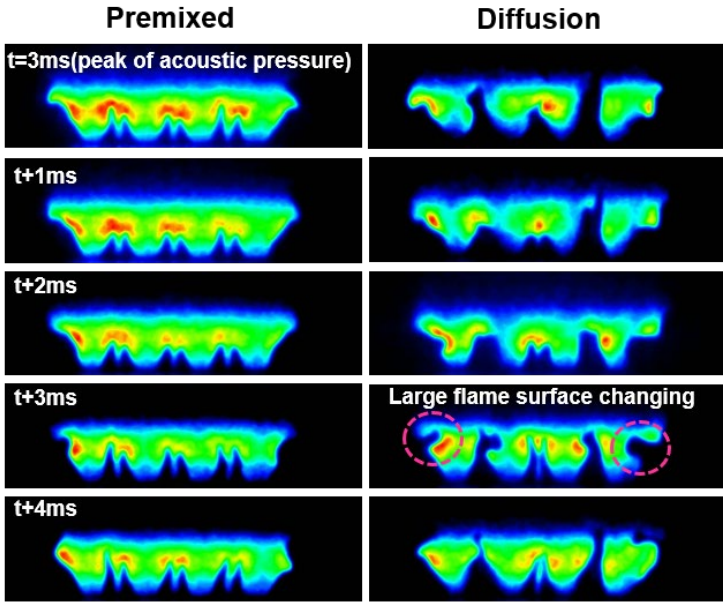

Figure 3.12. Instantaneous OH-PLIF images of premixed and diffusion flames under external perturbation at 200 Hz.

3.3.6. Rayleigh index and SPOD analysis

The results of flame forcing response by external perturbation are processed to calculate the frequency-driven Rayleigh index, R. This non-dimensional number is an indicator of thermo-acoustic instability or combustion instability. The frequency-driven Rayleigh index can be expressed by the following equation for the driving period [70].

$$R = \int_0^t \frac{p'q'}{p_{rms}\overline{q}} dt$$

The normalized pressure is expressed by the ratio of the measured pressure fluctuation (p') to the root-mean-square of the amplitude of the measured pressure (p_{rms}). The heat release rate fluctuation (q') and the mean heat release rate ($\bar{q}$) are obtained from OH-PLIF intensity as it is a good heat release indicator [71]. Two-dimensional Rayleigh index maps in Figure 3.13 (a) are obtained across 40 perturbation cycles at 200 Hz. This Rayleigh index map depicts the thermo-acoustical driving and damping regions along the second row of flames in the mesoscale burner array. Positive and negative Rayleigh indices indicate constructive (driving) and destructive (damping) thermo-acoustic coupling, respectively.

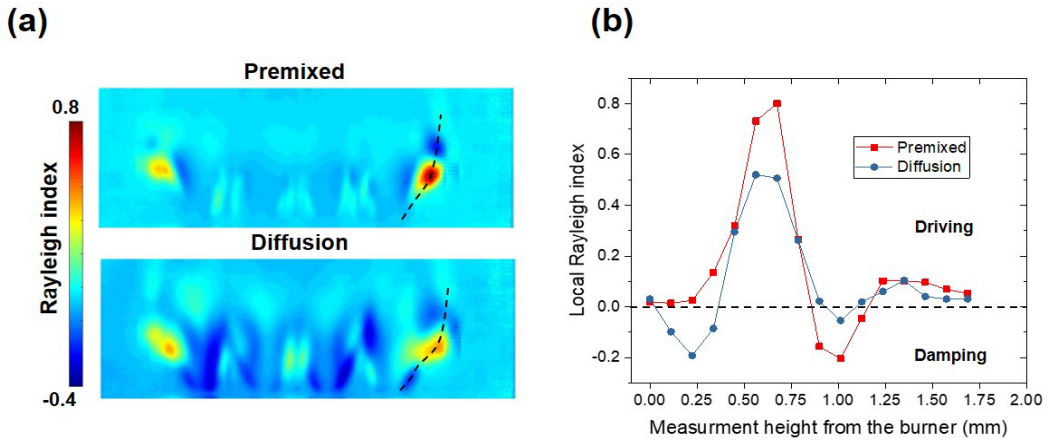

Figure 3.13. (a) 2D Rayleigh index map of premixed and diffusion flames and (b) local Rayleigh index along the outer flame boundary (dotted line in the Rayleigh index map) at 200 Hz.

In both the premixed and diffusion flames, the flames from the edge elements show intense positive Rayleigh indices (driving regime) and toroidal structures at the shear layer. These structures are formed by the axial flow fluctuation as seen in Figure 3.12 and are similar to the characteristic structures observed on low-swirl burner as reported by [72, 73]. Even with high swirl number, the forcing response of the mesoscale flame is similar to low-swirl burner because the angular momentum of the mesoscale burner array swirl flow is less than that of macroscale swirl flows. Lower Rayleigh indices are observed at the central region of the premixed and diffusion flames, indicating a region of strong flame interaction and are therefore more robust against thermo-acoustic instability in the shear layer [73, 74]. These flames are well isolated from ambient conditions. On the other hand, the edge elements are prone to thermo-acoustic insatiability by ambient heat loss and mixing with ambient air. The major difference between premixed and diffusion flames is that the thermo-acoustic instability driving and damping zones are wider under diffusion flames due to greater flame structure fluctuations. The spatial Rayleigh index distributions along the outer premixed and diffusion flame boundaries are plotted in Figure 3.13 (b). The two flames show similar Rayleigh index distribution along the toroidal structure centerline. The structure frequency is very similar since the perturbation is excited with the same acoustic amplitude and frequency. For a more comprehensive characterization of these structures, the same set of images is analyzed by SPOD technique.

SPOD is a method of extracting coherent modes for a wide range of applications including the mesoscale burner array. A detail derivation and explanation are introduced in [75, 76]. SPOD is similar to the classic POD method [77-79] which decomposes a set of images into orthogonal spatial modes by using singular value decomposition. However, SPOD uses a specific filter operation to the correlation matrix in POD analysis. This filter width is specified according to the

user's interest for certain physical phenomenon. The filter temporally resolves the POD modes. Consequently, the quantity *q(x,t)*, a scalar field, from the OH-PLIF intensity is decomposed into a set of basis functions such as the spatial eigenmodes $\Phi(x)$ and the time coefficients $a_n(t)$, which have a specific frequency mode. Therefore, the heat release *q(x,t)* can be reconstructed by following equation.

$$q(x,t) = a_0\Phi_0(x) + \sum_{n=1}^{\infty} a_n(t)\Phi_n(x)$$

A sequence of 2000 OH-PLIF images from premixed and diffusion flames is decomposed using SPOD to compare the heat release fluctuations. The SPOD filter width is set to 50, which is the ratio of the sampling rate to forcing frequency, for decomposing coherent structures due to the 200 Hz external perturbation. The SPOD spectra in Figure 3.14 show energy fractions of each SPOD mode (heat release fluctuation mode) and their corresponding frequencies. The dot size in the spectrum indicates the coherence of each SPOD mode and the SPOD mode structures indicate the spatial structures at the specific SPOD mode (at a given frequency). Coherent structure of two dominant modes, mode A (200 Hz) and B (400 Hz) in Figure 3.14, corresponding to the first and second highest energy fractions is also shown. Energy contents of mode A and B account for 48.75 % and 38.14 % of the total energy in premixed and diffusion flames, respectively. Coherent structures in the premixed flames are mainly observed near the shear layer.

Furthermore, phase difference between the edge and central flames is also observed in SPOD mode structures. For diffusion flames, the coherent structures near the shear layer are thicker than those of the premixed flames. Coherent structures are also observed near the inner recirculation zones indicating a larger fluctuating region that can lead to significant flame structure transformations in diffusion flames. Even though diffusion flames show similar thermo-acoustic instability characteristics based on Rayleigh indices, they exhibit increased heat release

fluctuations as shown in Figure 3.11 and Figure 3.12 which are likely driven by changes in reactant unmixedness due to flow perturbation [80].

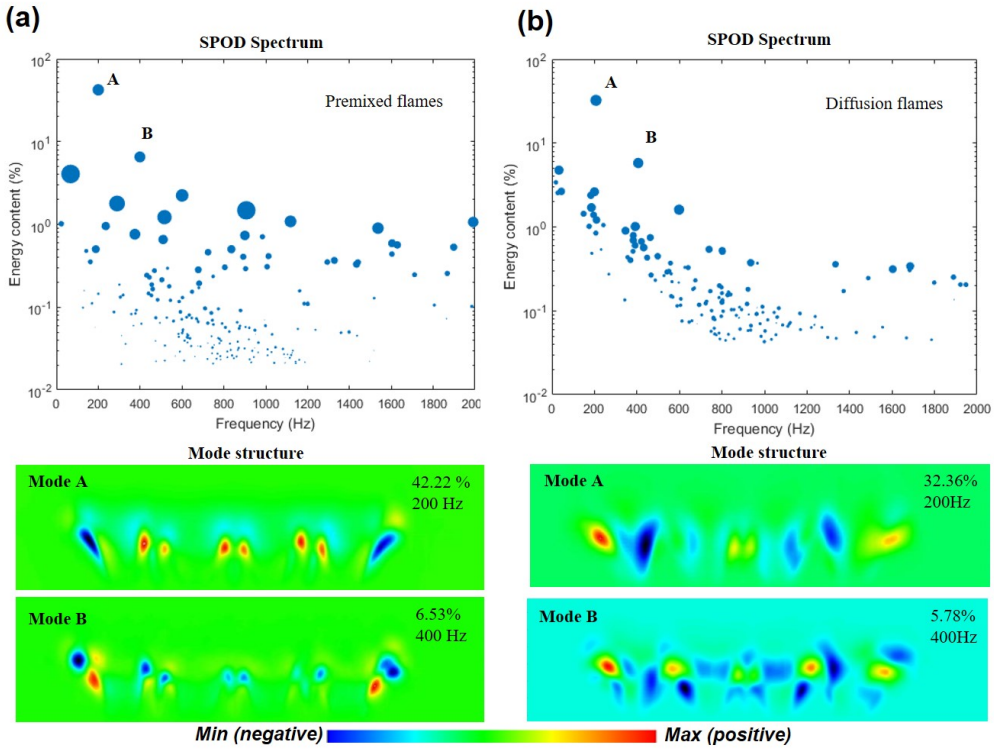

Figure 3.14. SPOD spectra and mode structures of the (a) premixed and (b) diffusion flames at 200 Hz.

SPOD analysis also reveals higher heat release fluctuations in structures observed in the recirculation zones for diffusion flames compared to premixed flames which suggests fuel unmixedness as driving factor for thermo-acoustic instability. Further, SPOD modes of the diffusion flame reveal the presence of irregular structures in each flame as seen in the two dominant SPOD modes in Figure 3.14. This large, irregular spatial and temporal heat release fluctuation is mostly likely due to reactant unmixedness of diffusion flames further exacerbated by external perturbation rather than flow turbulence, as the flow field remains fairly laminar

without acoustic perturbations. SPOD structures of both premixed and diffusion flames are symmetrical because heat fluctuations are driven by axial perturbation modes and not by the natural shear layer instability from vortex shedding. Although the SPOD mode structures are observed in the central flames of both premixed and diffusion flames, they exhibit very little thermo-acoustic instability (negative Rayleigh index) compared to edge flames in Figure 3.13. As a result, the central flame zone is weakly affected by the driving acoustic pressures that arise from the burner resonance or external disturbance. SPOD analysis has shown that the thermo-acoustic driving zone is closely related to dominant SPOD mode.

3.4. Conclusions

In this research, a diffusion mesoscale burner array has been developed for small-scale and efficient power-generation applications. The fuel is injected into a swirl-inducing geometry to effectively mix fuel and air while enhancing flame interactions. Premixed and diffusion flames are employed to characterize the burner performance and analyze diffusion flame stability in the diffusion mesoscale burner array. The mesoscale burner array performance characterization is conducted by measuring lean blow off and flame temperatures of premixed and diffusion flames in the mesoscale burner array. Slightly leaner blow off equivalence ratios and higher local temperatures are observed in the diffusion flames due to fuel unpremixedness producing higher local equivalence ratios. OH and CH_2O fluorescence images of premixed and diffusion flames show similar stabilization mechanisms and flame interaction structures. Stability and flame dynamics analysis are carried out under externally perturbed flow conditions using Rayleigh index and spectral proper orthogonal decomposition. Incomplete fuel mixing leads to higher local equivalence ratios in diffusion flames, which ultimately results in higher heat release fluctuations

compared to premixed flames. Both flames show thermo-acoustic damping characteristics at the center of the burner array due to strong flame interactions. In conclusion, the radial fuel injection strategy in the diffusion mesoscale burner array architecture is capable of producing the required output for small-scale applications such as unmanned aerial vehicle and power generation systems with improved combustion stability. Furthermore, this design configuration has a potential for liquid hydrocarbon fuel injection since the fuel can be readily vaporized without the need for atomization due to large surface to volume ratio of the mesoscale burner assembly.

CHAPTER 4. JET A COMBUSTION IN A MESOSCALE SWIRL-STABILIZED BURNER ARRAY

We investigate the use of Jet A fuel in a mesoscale burner array, developed to improve small-scale flame stability and reduce combustor length scale. Jet A is vaporized before being mixed with air to produce premixed Jet A-air flame arrays. The reactant mixture temperature is controlled by a heater to study the effects of mixture temperature on flame stability. Overall combustion characteristics of Jet A and methane are compared on the mesoscale burner array. The Jet A flame array exhibited higher lean blow-off equivalence ratio than that of the methane flame array under a range of inlet temperatures varying from 373.15 to 773.15 K. The heated Jet A fuel composition is analyzed using gas chromatography-mass spectrometry. 10 kHz planar laser-induced fluorescence (PLIF) imaging of the hydroxyl radical (OH) is employed to visualize the post-combustion zone of the Jet A flame array using filtered separation of Jet A fluorescence. From the OH-PLIF images, the Jet A flame array showed narrower flame structures and smaller recirculation zones compared to that of the methane flame under the same operating condition. Furthermore, the Jet A flame array showed larger flame fluctuations compared to that of the methane flame at an equivalence ratio of 0.8 based on proper orthogonal decomposition (POD) analysis. These results can be extended toward designing and operating other small-scale combustion systems using heavy hydrocarbon liquid fuels.

4.1. Introduction

Recently, there is considerable interest in small-scale combustion systems and stable power generations [81]. Hydrocarbon (HC) fuels are promising energy sources for light and portable energy systems due to their higher energy density compared to modern electric batteries [2, 82, 83]. Even accounting for the electrical conversion losses in practical devices, HC fuels can easily outperform other power sources in practical propulsion systems in terms of energy density [24]. Moreover, micro- and mesoscale combustion systems are being proposed due to recent advances in micro-machining and fabrication techniques [2, 3, 7, 36]. Therefore, a wide range of studies from fundamental small-scale combustion science to portable power supply are being performed [2]. Despite these efforts, however, many critical issues still remain for developing a practical small-scale combustion system.

Small-scale flames in compact geometries are susceptible to thermal quenching and potential extinction mechanisms that reduce flame stability [3-5]. Furthermore, compact burner dimensions may induce inadequate fuel/oxidizer mixing and shorten residence time inside combustors, thereby compromising highly efficient and stable combustor operations [82]. The reduced residence timescale of compact combustors can also induce flame quenching, incomplete reaction, and unsteady flame dynamics [20-22]. These concerns must be addressed for compact burners to be widely adapted in small-scale applications [2, 7].

In response to these concerns, a mesoscale burner array [24] has been developed by exploiting multiple flame interactions to enhance flame stability and combustion efficiency [45-48]. The mesoscale burner array has a counter-rotating arrangement for improving flame interactions with neighboring swirl-stabilized flames. This unique configuration can minimize heat loss and maximize flame stability by reducing the overall combustor length scale [24, 52].

However, liquid fuels with low vapor pressure, such as kerosene-based fuels, can induce a number of challenges and prevent efficient and stable mesoscale combustor system operations since liquid fuels must be vaporized prior to being mixed with air for use in the mesoscale burner array.

In light of the shorter diffusion length scale and residence timescale in the mesoscale burner array, injection or dispersion techniques capable of producing micron-range droplets or films are necessary for quick vaporization. Another approach is to use a recuperator in a compact burner system to improve fuel vaporization and efficiency [82]. In addition to the aforementioned physical challenges, heavier hydrocarbon fuels have different lean blow-off and flame dynamic characteristics compared to single-component gaseous fuels. Heavy hydrocarbon fuels, such as an alternative alcohol-derived kerosene and Jet A, are much more susceptible to lean fuel operations compared to methane [84]. Therefore, a study of heavy hydrocarbon fuel flame behaviors in small-scale combustor systems is required since their geometric constraint can have significant effects on flame dynamics.

In this study, a heavy hydrocarbon fuel, Jet A, is fully or partially vaporized and used to analyze flame characteristics in the mesoscale burner array. Air and fuel inlet temperatures are carefully controlled to study the effects of inlet temperatures on flame stability using the lean blow-off equivalence ratio. We have also investigated the basic aspects of the fuel heating process under highly heated condition using gas chromatography-mass spectrometry (GC-MS). Composition changes of Jet A fuel are analyzed to show the effect of the fuel heating process during the vaporization. Mesoscale flame dynamics are studied using a 10 kHz high-speed imaging system. Hydroxyl radical (OH) and Jet A planar laser-induced fluorescence (PLIF) are imaged using an optical filter and selective wavelengths. A gaseous fuel, methane, is also used with Jet A to study fuel composition effects on the mesoscale flame array by comparing flame structures and

stabilities. The overall flame dynamics in the mesoscale swirl flame array may provide insights into the design optimization of micro/mesoscale combustion systems using heavy hydrocarbon fuels.

4.2. Experimental setup

4.2.1. Mesoscale burner array design and operation

The 4 × 4 mesoscale burner array is designed for small-scale combustion applications by exploiting uniform and well-distributed flames [24, 56]. The burner architecture is fabricated using the direct metal laser sintering (DMLS) technique. The burner design parameters are provided in our previous research [24, 56]. A schematic of the burner cross section is shown in Figure 4.1 (a). Every burner element consists of a bluff body with two tangential inlets. First, the premixed air/fuel reactant mixture is fed through the burner inlet layer and headed into the two tangential inlets (swirl structures) for every burner element to produce a swirling flow. The swirling reactant passes through the burner layer and then forms a swirl-stabilized flame on each bluff body. Individual mesoscale flames interact with neighboring flames thereby improving flame stability using a counter-rotating swirl pattern known as the Taylor-Green vortex arrangement [23].

The liquid fuel and inlet air temperature are controlled by external heating systems. The Jet A fuel flow rate is controlled using a LEGATO 100 syringe pump (±0.5% accuracy). The liquid fuel, Jet A, is heated by a tubular furnace (Lindberg/Blue M Mini-Mite Furnace, Thermo Scientific). A K-type thermocouple (Omega) is embedded at the tube outlet to measure the vaporized fuel temperature. Air is supplied to the burner using MKS mass flow controllers (±1% accuracy). After the mass flow controller, the inlet air temperature is controlled by an inline air

heater (4 kW threaded inline heater, Tutco Sureheat). The heated air and fuel are mixed in the mixing tube as seen in Figure 4.1 (b). The mixing tube is designed using co-axial stainless steel tubes for preventing fuel condensation. The preheated mixture is injected into each individual burner element of the mesoscale flame array. Figure 4.1 (c) shows the schematic of the experimental setup for studying the combustion characteristics of the liquid-fueled mesoscale burner. The effects of liquid fuel and inlet mixture temperature on burner performance and flame dynamics are analyzed using lean blow-off limit and OH-PLIF imaging. Fuel component changes due to the fuel heating are also studied using a GC-MS system (6980N gas chromatograph and 5973N mass selective detector, Agilent).

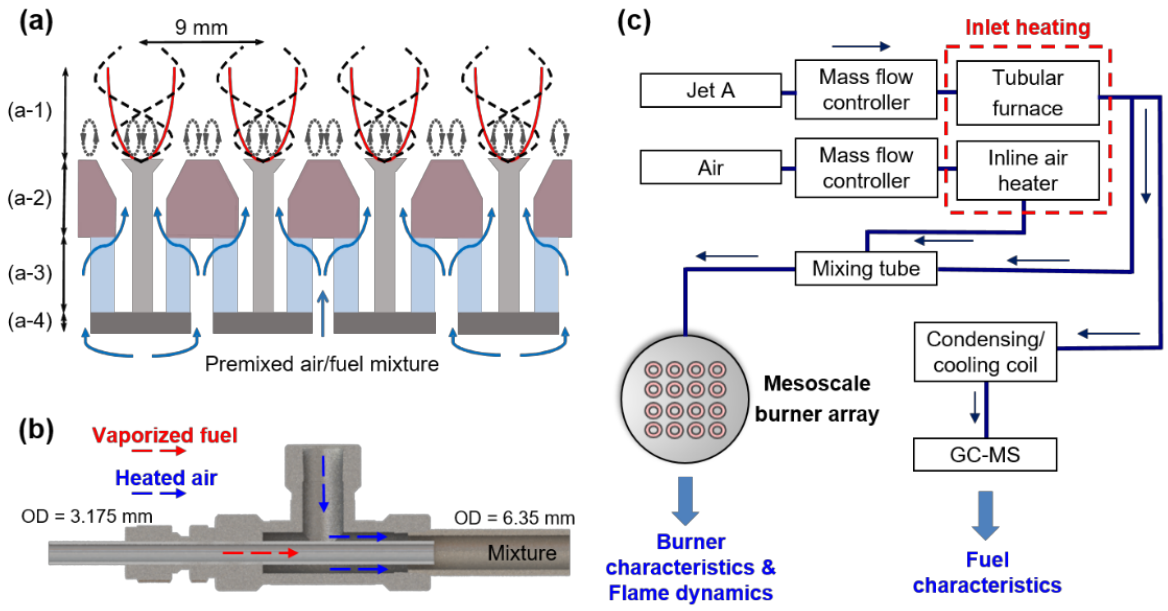

Figure 4.1. (a) Cross section of the 4 × 4 mesoscale burner array: (a-1) swirl-stabilized mesoscale flames, (a-2) burner layer, (a-3) tangential inlet, and (a-4) inlet layer. (b) Co-axial stainless steel air/fuel mixing tube. (c) Schematic diagram of the experiment setup.

4.2.2. OH-PLIF imaging setup

The OH-PLIF setup is introduced in Figure 4.2. A 10 kHz diode pumped solid-state Nd:YAG laser (Innoslab IS200-2-L, EdgeWave) is used to pump a tunable dye laser (Credo dye laser, Sirah). The beam from the dye laser is produced with a Rhodamine 6G dye solution. Output from the doubling crystal after second harmonic generation is used to excite the Q_1 (7) line of the $A^2\Sigma^+$-$X^2\Pi$ (1, 0) band of OH at near 283 nm. The output beam is formed into a thin laser sheet using sheet forming optics. The laser sheet propagates through the combustion area of interest above the mesoscale burner array. OH fluorescence is carefully filtered and imaged with a narrow band-pass filter (10 nm full width at half-maximum (FWHM) at 310 nm, Asahi) to mitigate fuel fluorescence. The filtered fluorescence is intensified and recorded by a high-speed imaging system, which is composed of a complementary metal oxide semiconductor (CMOS) camera (FASCAM SA-Z, Photron), an image intensifier (High-Speed IRO, LaVision), and a 100 mm f/2.8 CERCO UV lens (Sodern).

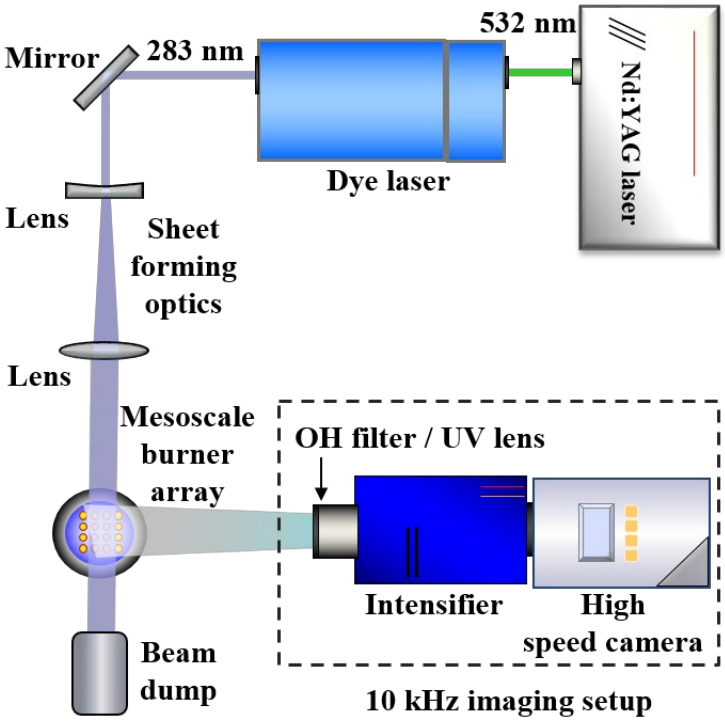

Figure 4.2. 10 KHz OH-PLIF imaging setup.

4.3. Results and discussion

4.3.1. Properties of Jet A

The distillation curve of Jet A (POSF 10325) as reported by the US Air Force Research Laboratory [85, 86] is reproduced in Figure 4.3 (a). It shows that the fuel temperature must exceed 542.15 K, so that the fuel is fully vaporized before being injected into the mixing tube to mitigate internal fuel condensation effects. Stable flame operations will be predicated on the fact that the vaporized fuel in the mesoscale burner array remains free of condensation by maintaining the temperature of the fuel-air mixture higher than its liquid-vapor equilibrium curve.

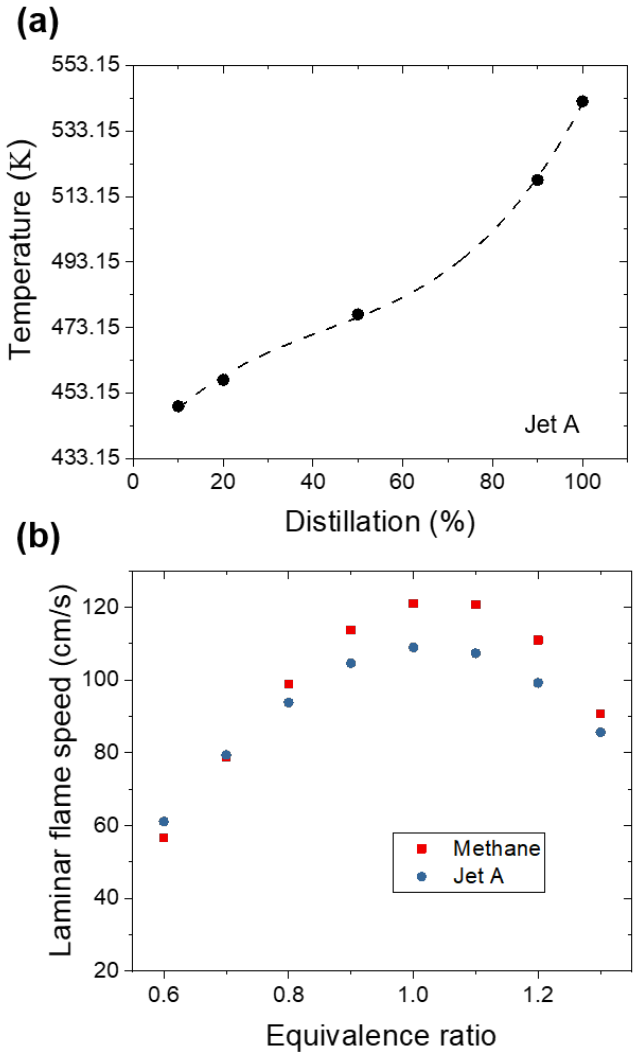

Figure 4.3. (a) Jet A distillation curve and (b) calculated laminar flame speeds of methane and Jet A at 573.15 K.

Laminar flame speeds of Jet A/air and methane/air are calculated in Figure 4.3 (b) as a means of discerning the flame dynamic characteristics of the two fuels. The data points are calculated using CHEMKIN software [87] using HyChem A2 [88, 89] and GRI-Mech 3.0 [90] chemical kinetics mechanisms. Jet A and methane show similar laminar flame speeds under fuel lean conditions at 573.15 K. Below the equivalence ratio of 0.6, the laminar flame speed of Jet A

is faster than that of methane, whereas at a higher equivalence ratio, it is vice versa. Laminar flame speed is often used for estimating flame lean blow-off equivalence ratio, but to better understand Jet A flame stabilization on the mesoscale burner array under fuel lean conditions, further comparison with methane flames will be necessary. Therefore, various inlet mixture and fuel temperature conditions are examined to study their effects on flame stability.

4.3.2. Lean blow-off (LBO) limit

Figure 4.4 shows the LBO characteristics of Jet A and methane flame arrays for various inlet mixture and Jet A heating temperatures. The air and Jet A are heated by an inline air heater and a tubular furnace, respectively, prior to being injected into the mixing tube. The methane is fed directly from the mass flow controller to the mixing tube. The inlet mixture temperature, combustor inlet temperature, is controlled by adjusting the upstream air and fuel temperatures. The equivalence ratios of Jet A/air mixture are calculated using the molar composition of $C_{11.4}H_{21.7}$ [91]. From Figure 4.4, the first lift-off indicates the equivalence ratio when the first flame elements start to lift off [56]. The air flow rate is set to 50 SLPM and the lean blow-off equivalence ratios are determined by reducing fuel flow rates.

The effect of inlet mixture temperature on LBO limits can be seen in Figure 4.4 (a). Flame LBO is triggered by the insufficient physical (flow) timescale compared to the chemical reaction timescale. Visible images of Jet A flame blow-off process are shown in Figure 4.4 (b). The LBO equivalence ratios of both methane and Jet A flame arrays slightly decrease as inlet mixture temperatures are increased. This result is attributed to the increased chemical reaction rate of the combustion reactants [64, 65].

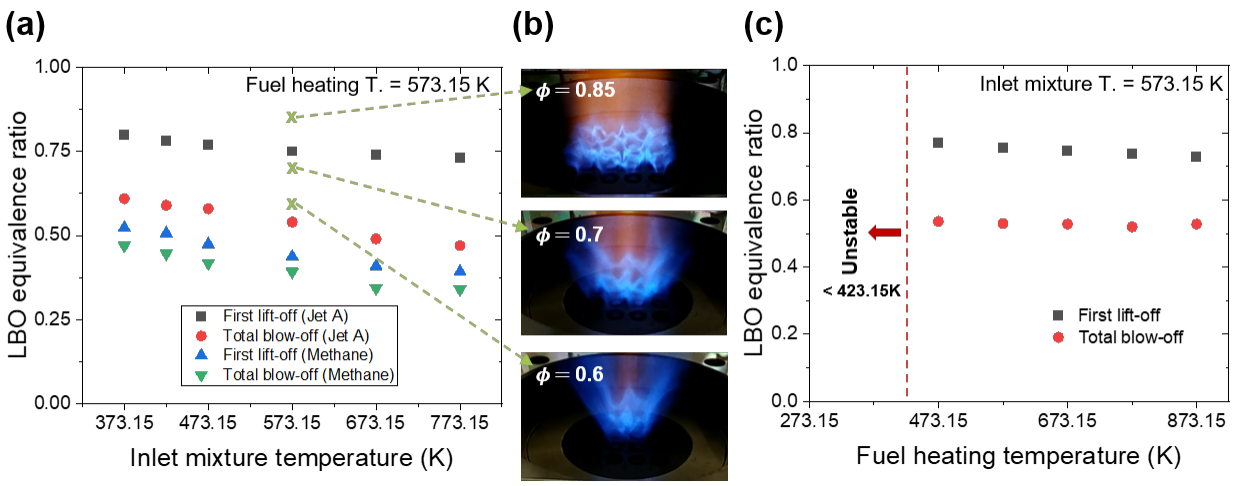

Figure 4.4. (a) Effect of inlet mixture temperature on the lean blow-off equivalence ratio. (b) Visible images of the Jet A flame array. (c) Effect of Jet A heating temperature on the lean blow-off equivalence ratio.

The lean blow-off equivalence ratios of Jet A flame arrays are much higher than those of methane. The result indicates Jet A, a heavy hydrocarbon fuel, is less stable than methane over a wide range of inlet mixture temperatures under fuel lean operations. Furthermore, differences between the first lift-off and the total blow-off equivalence ratios of Jet A flame arrays are significantly higher than those of methane flame arrays. The first flame lift-off starts from one of the edge flame elements in the burner array. Jet A flame is more susceptible to lean blow off without flame-to-flame interactions, which can prevent ambient heat loss and improve flow swirl strength, inducing a stronger center recirculation flow. Therefore, the heat loss at the outer flames is highly correlated to Jet A flame stability limit under lean fuel operation conditions. This trend cannot be explained by high-temperature chemistry such as laminar flame speed even though that is widely used for estimating lean blow-off equivalence ratio in gas turbines [92]. Instead, low-temperature chemistry during the fuel preheating process may be closely related to flame lean

blow-off characteristics for different fuel types as noted in the literature of vaporized kerosene flame characteristics [84, 93].

The effect of fuel heating temperature on flame blow-off characteristics is shown in Figure 4.4 (c). When the fuel heating temperature is lower than roughly 423.15 K, inadequate fuel and air mixing due to condensation may further exacerbate flame stabilization issues and lead to immediately blow off after ignition. The first lift-off equivalence ratios show a slight negative slope as a function of fuel heating temperature from $\phi = 0.77$ at 473.15 K to $\phi = 0.73$ at 873.15 K. However, the total blow-off equivalence ratios are fairly constant for fuel heating temperatures ranging from 473.15 to 873.15 K. These results indicate that the vaporized Jet A flame stability is largely affected by the inlet mixture temperature rather than the fuel heating temperature. The slightly decreased LBO equivalence ratio in the first lift-off can be attributed to the inadequate vaporization or incomplete air/fuel mixing under low fuel injection temperature. In the high temperature region, fuel thermal cracking into lighter hydrocarbons might have an effect on the first lift-off characteristics on the mesoscale burner array.

4.3.3. GC-MS characterization

Figure 4.5 shows the total ion current chromatogram of Jet A at 298.15 K and 873.15 K. The Jet A fuel flowrate is set to 1 mL/min through the heated vaporization tube (o.d. = 3.175 mm, i.d. = 1.397 mm). The heater was operated at atmospheric pressure and has a length of 30 cm. During the vaporization process in the heated tube, Jet A can undergo composition changes and cracking. Therefore, the sampled fuel is analyzed to characterize any changes in fuel composition due to external heating using a GC-MS. The sampled fuel compositions are characterized by isolating heavy hydrocarbon compounds using an HP-5ms column (Agilent).

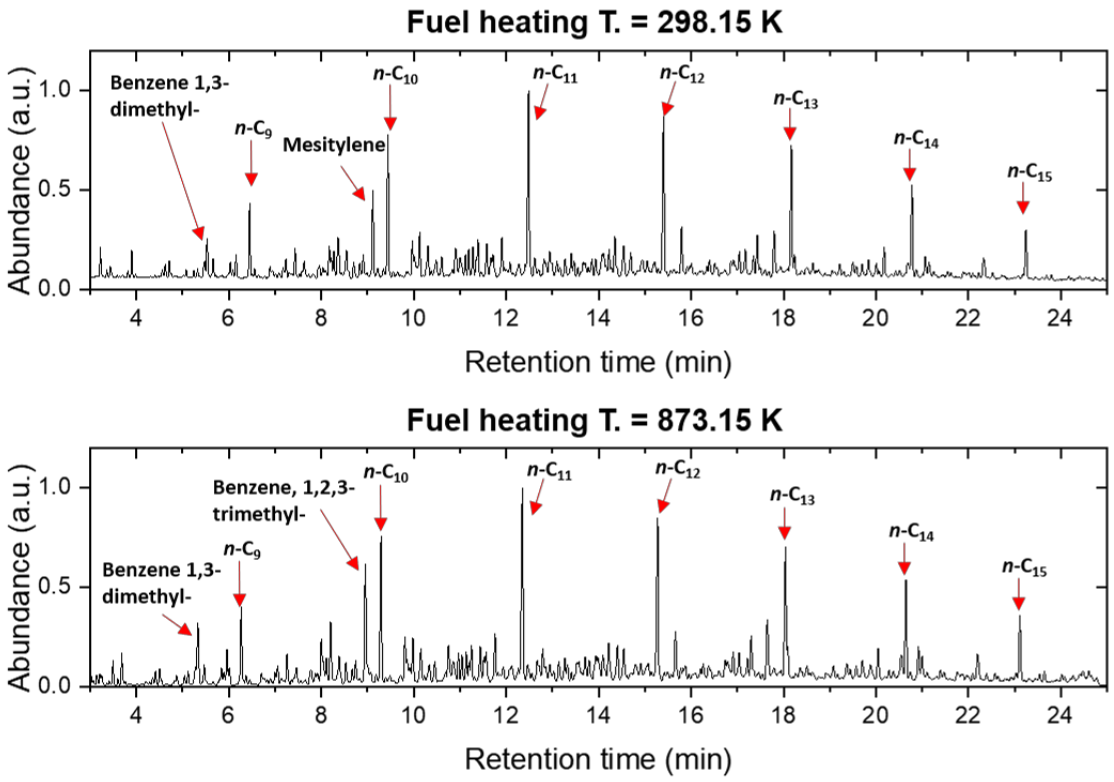

Figure 4.5. Total ion current (TIC) chromatogram of Jet A from a GC-MS.

The GC-MS analysis results show no discernible changes in hydrocarbon compositions from *n*-C9 to *n*-C15 up to 873.15 K using the existing tubular furnace. At 873.15 K, the gas yield (indicator of fuel decomposition to gaseous component) is 6.15 ± 0.62 wt %. At 873.15 K, slight increases in benzene trimethyl and benzene dimethyl peaks are observed. However, no noticeable polycyclic aromatic hydrocarbons (PAH), a precursor to carbon deposits [94], are formed during the fuel heating process. Therefore, fuel heating up to 873.15 K had no significant effect on fuel composition.

4.3.4. OH and Jet A-PLIF

For OH-PLIF imaging, a method of isolating OH-PLIF from fuel fluorescence was utilized using a narrow band-pass filter (FWHM = 10 nm) as seen in Figure 4.6 (a). The kerosene vapor fluorescence emission spectrum in Figure 4.6 (a) is mainly composed of two fluorescence bands, monoaromatics and diaromatics fluorescence, which strongly vary with excitation wavelength as reported in [95, 96]. The key insight is that the signal from monoaromatics from kerosene-based fuel can be significantly reduced using an excitation wavelength at 283 nm and an appropriate optical filter for OH fluorescence [97]. The intensifier gate width was also minimized to separate OH signal from fuel fluorescence, while rejecting the excitation wavelength by optical filtering because kerosene-based fuel has long fluorescence emission timescale than OH fluorescence [96, 97]. Thus, the mesoscale flame characteristics of the two fuels, Jet A and methane, can be studied over a range of operating conditions by examining flame structures using OH-PLIF images.

An alternative diagnostic technique can visualize both the fuel and OH on the mesoscale burner array by carefully tuning the laser wavelength. From Figure 4.6 (b), OH fluorescence yield was carefully tuned to a wavelength slightly off the $Q_1(7)$ peak for simultaneous measurement of Jet A vapor and OH fluorescence. The detuned excitation wavelength produces Jet A vapor fluorescence signal intensity that is roughly equivalent to that of OH fluorescence. This strategy can simultaneously show both fuel and OH regions on the mesoscale burner array as the OH and fuel regions are clearly separated by a thin reaction layer. Fuel fluorescence can give valuable insight into the flame interactions within the mesoscale burner array and the blow-off process.

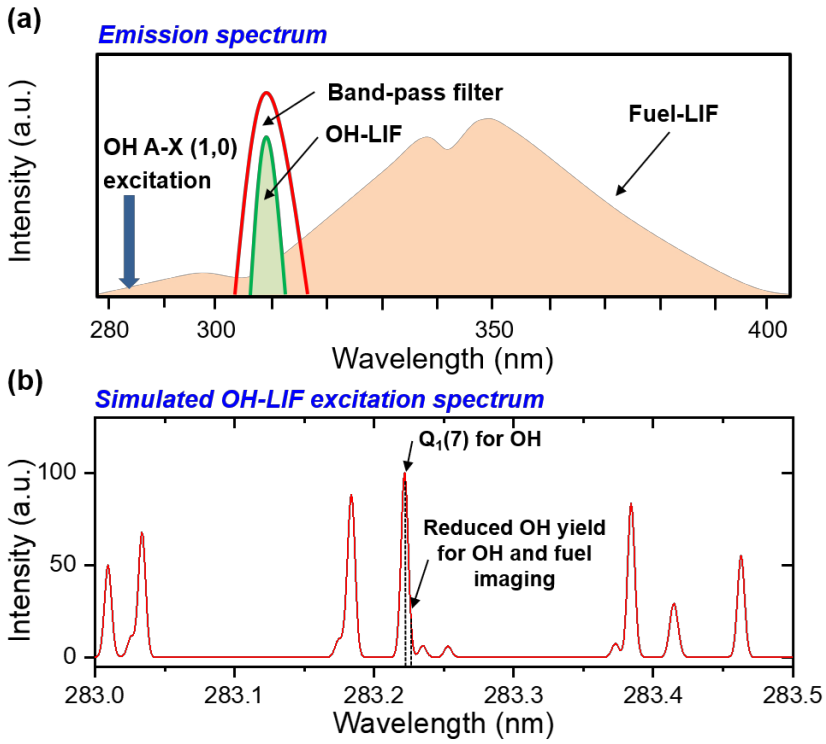

Figure 4.6. (a) Emission spectrum of OH and kerosene-based Jet A fuel when excited at 283 nm. (b) Excitation strategy for imaging OH and vaporized Jet A.

Figure 4.7 shows PLIF images that were averaged over 1000 shots. The excitation wavelength is carefully tuned to simultaneously visualize Jet A and OH fluorescence. Jet A vapor and OH radicals are visualized at an inlet temperature of 573.15 K. The PLIF images were visualized using a grayscale color map without any postprocessing since the images were intended to provide a qualitative comparison between flame conditions. In the cold flow image (Figure 4.7 (a)), only Jet A vapor is visualized due to the absence of ignition. Jet A vapor from each burner element is stabilized on the bluff body by the swirl flow. Jet A vapor on the outer burner elements is angled inward toward the center of the burner array due to viscous effects from the surrounding air.

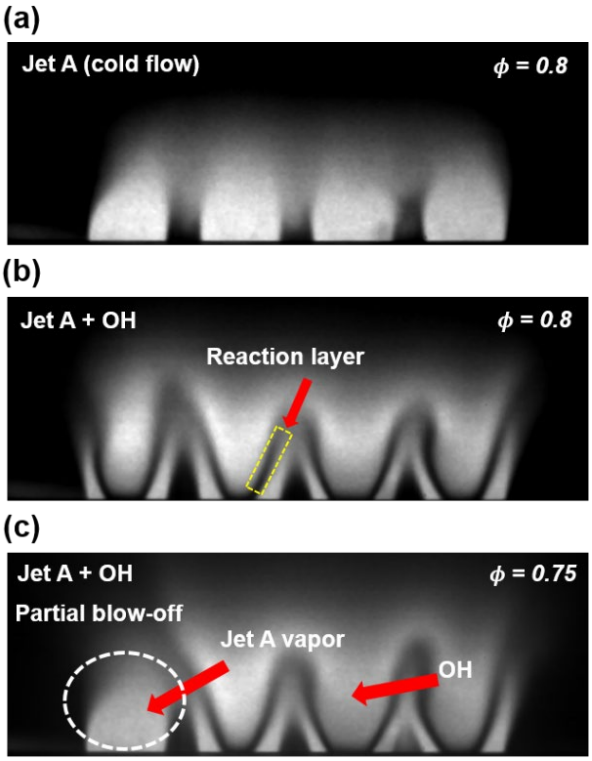

Figure 4.7. Averaged OH and Jet A-PLIF images of (a) cold flow at ϕ = 0.8, (b) reactive flow at ϕ = 0.8, and (c) at ϕ = 0.75.

Flames in the reactive flow following an ignition process were visualized using both Jet A and OH-PLIF imaging as shown in Figure 4.7 (b). At an equivalence ratio of 0.8, all of the flames were well stabilized on their respective bluff bodies. Jet A vapor region and OH radicals were observed as expected in Figure 4.7 (b) and the two regions appear to be clearly separated by the reaction layer. Both OH, a major combustion product, and fuel are absent in the combustion reaction layer. As such, simultaneous OH and Jet A fluorescence images can identify the combustion reaction layer, which is normally visualized using CH-PLIF. Figure 4.7 (b) clearly shows V-shaped flame structures that are well stabilized on their respective bluff bodies. As a combustion product, OH radical can exist in the center recirculation zone and mix with reactants due to swirl stabilization [24, 98]. Therefore, the OH fluorescence on the bluff body can be used

to estimate the recirculation zone size and shape. The outer flames show the narrower recirculation zones, estimated by the flame structures, compared to the center flame recirculation zones.

Next, a partial blow-off condition in Figure 4.7 (c), was recreated by decreasing the equivalence ratio from 0.8 to 0.75. Visual inspection of the flame array confirmed that one of the edge flames had been lifted off. The neighboring flame in the PLIF image shows the fuel vapor stabilized on the bluff body reacting with the neighboring flame further downstream due to the outer flame lift-off on the burner array. This result clearly shows that the combustion reaction layer is located in between OH radicals and Jet A vapor.

Jet A and OH-PLIF images in Figure 4.8 show the lean blow-off process at the edge flame element. From Figure 4.8 (a), edge flames show weaker interactions compared to center flames as evidenced by long flame merging distances since Jet A vapor can penetrate further downstream. The Jet A fuel vapor from the left side edge flame is completely separated from the Jet A vapor from the center element. When the narrow flame (leftmost flame in Figure 4.8 (a)) fluctuates, the size of the recirculation region decreases and exhibits larger flame surface variations. At an equivalence ratio of 0.75, the leftmost flame is lifted up and the unburned Jet A vapor is stabilized on the bluff body in Figure 4.8 (b). The lower equivalence ratio increased the chemical reaction timescale eventually led to blow out after the leftmost flame structure became too narrow [99]. Furthermore, the outer flame on the right-hand side also showed large fluctuation and narrow recirculation zone from the OH-PLIF. The gap between OH and Jet A vapor layer at the edge flames is further increased as the flame near the LBO condition due to a thicker reaction layer.

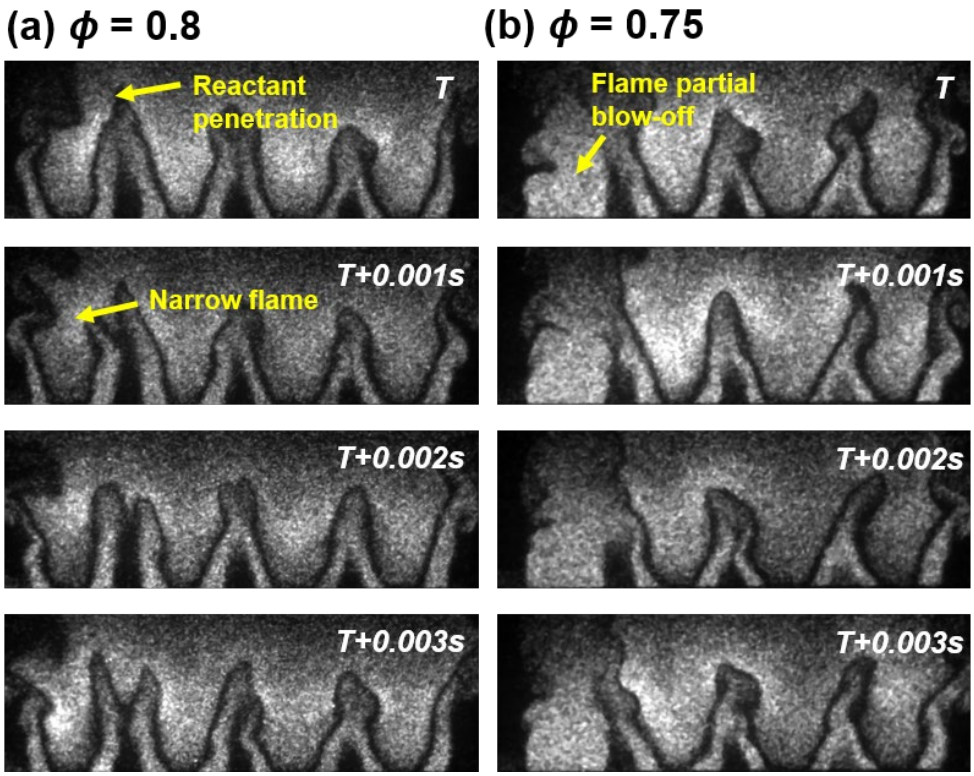

Figure 4.8. Jet A and OH-PLIF images at equivalence ratios of 0.8 and 0.75.

4.3.5. OH-PLIF separation

Figure 4.9 (a) shows an optimized OH-PLIF image by mitigating Jet A fluorescence using the narrow optical band-pass filter. The imaging gate was maintained at 20 ns and the excitation wavelength was tuned to the peak of $Q_1(7)$ with an inlet temperature of 573.15 K. The image in Figure 4.9 is raw data without any postprocessing. Figure 4.9 (b) shows the fluorescence signal intensities across one of mesoscale flame along the red dot line (*X*-*X*') in Figure 4.9 (a). The Jet A fluorescence signal level is largely negligible because it is comparable to the noise intensity. The OH-PLIF images can be used to study flame structures and dynamics by applying proper orthogonal decomposition (POD).

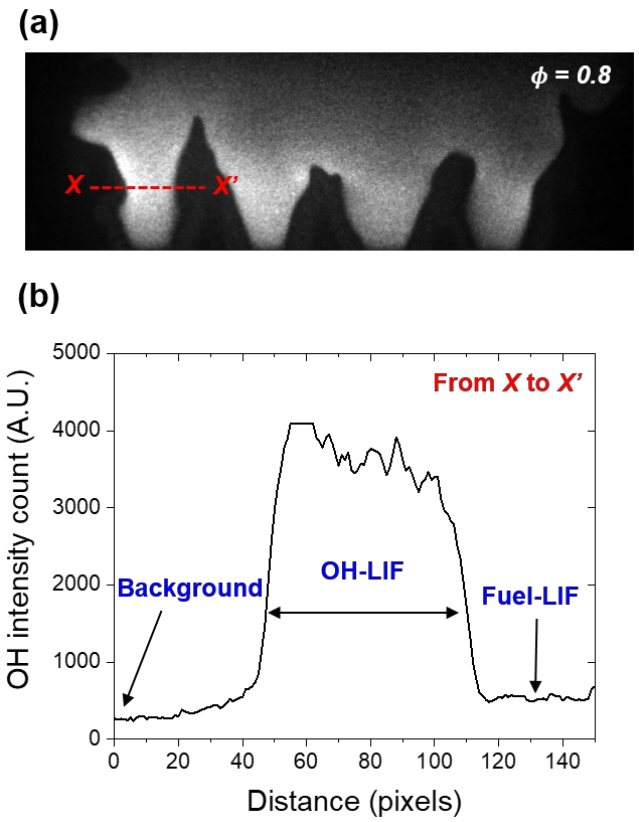

Figure 4.9. (a) Optimized OH-PLIF image with minimal Jet A fluorescence and (b) fluorescence intensity profile across a single flame.

OH-PLIF images of Jet A flames were compared with those of methane flames as shown in Figure 4.10. Both methane and Jet A flame images were taken at the same inlet mixture temperature of 573.15 K. The methane flame array in Figure 4.10 (a) shows bluff body-stabilized structure with M-shaped flame at the flame merging region. These flame structures are the result of strong flame interactions in the burner array. The flame merging region in the methane flame array is much closer to the burner surface than that of the Jet A flame.

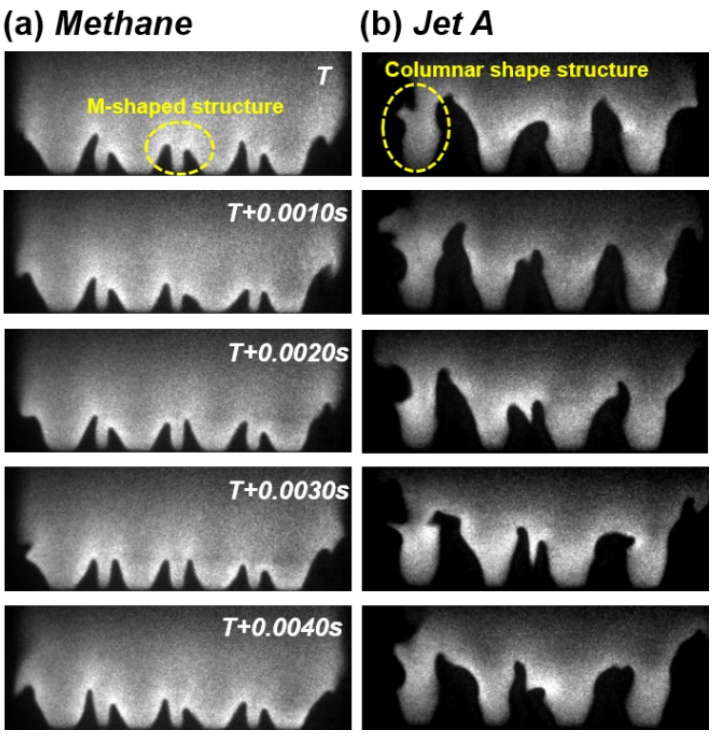

Figure 4.10. OH-PLIF images of the (a) methane and (b) Jet A flame array at an equivalence ratio of 0.8.

The Jet A flame structure is narrower than the methane flame structure in Figure 4.10 (b). The Jet A flame array shows smaller recirculation zone compared to methane flame's recirculation zone on the bluff body. Moreover, larger flame surface fluctuations were observed at the outer flames in the Jet A flame array. Once the columnar shape flame was observed (at the left side outer flame), the flame can be considered to have initiated the blow-off process. From these images, the overall Jet A combustion reaction occurs farther away from the burner surface with a longer chemical reaction timescale than methane combustion. These results demonstrate that fuel composition differences have an effect on flame characteristics and dynamics. According to a recent study, prevaporized heavy hydrocarbon fuels have been shown to have higher lean blow-off equivalence ratios compared to methane and ethanol [84, 92]. This is also consistent with

observations deduced from Figure 4.10. For small-scale burners, in particular, the variation in the flame stabilization structure is largely driven by the differences in chemical reaction timescale between methane and Jet A combustion processes. Thus, LBO for small-scale flames should be characterized by chemical timescale estimations based on low-temperature reaction mechanisms rather than laminar flame speed.

4.3.6. POD analysis

Snapshot POD analysis is used to study mesoscale flame dynamics using two different fuels in Figure 4.11. POD is one of several modal decomposition techniques that decomposes a series of snapshot images into a set of orthogonal modes with their energy contents using singular value decomposition [77, 78]. A total of 2000 snapshot images, taken from the same experimental condition as the images shown in Figure 4.10, are used without any postprocessing and mean subtraction in the POD analysis. Therefore, a scalar field $q(x,t)$ from OH-PLIF images can be expressed by the following equation: $q(x,t) = \sum_{n=0}^{N-1} a_n(t)\Phi_n(x)$, where *N*, *Φ(x)*, and *a(t)* represent the number of snapshots, spatial modes, and time coefficients, respectively. The energy contents of the mean modes (zeroth POD modes) for the methane and Jet A flame array are 97.9 and 93.1%, respectively. The zeroth POD mode represents time-averaged OH images and can be used to gauge the flame stability as well as determine the total fluctuation energy content of all of the other POD modes [50, 100]. Therefore, the lower-energy content in the mean mode of the Jet A flame array compared to that of methane flame array indicates a larger fluctuation energy content in the Jet A flame array.

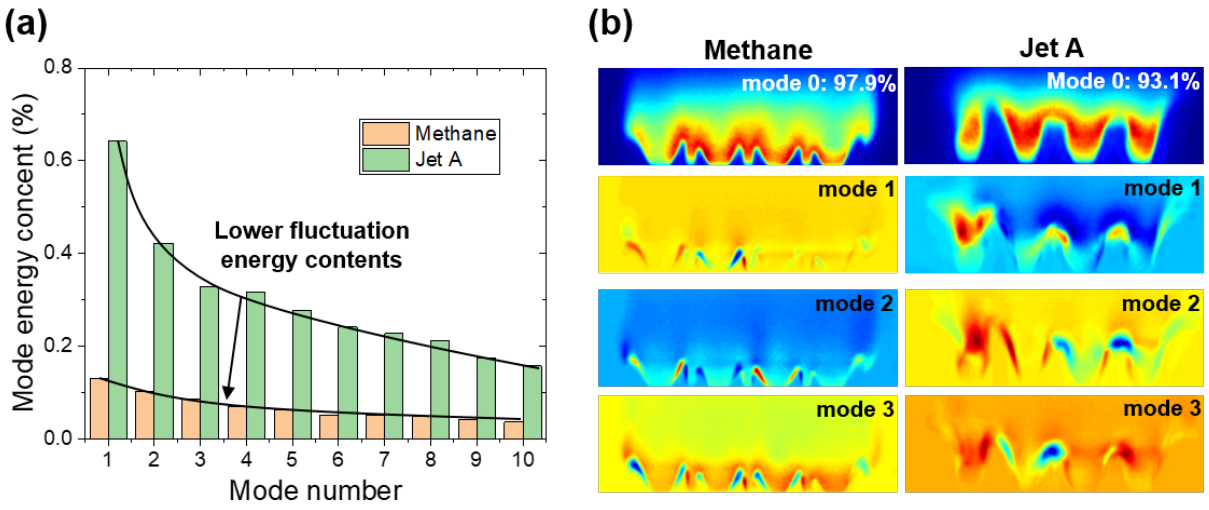

Figure 4.11. (a) POD mode energy contents and (b) mode structures of the methane and Jet A flame arrays.

The results in Figure 4.11 (a) show the energy contents of the first 10 fluctuating modes (POD mode 1-10). Overall, the first 10 fluctuating POD modes of the Jet A flame array show higher energy contents than those of the methane flame array as expected from the mean mode energy comparison. From Figure 4.11 (b), the zeroth mode structure of the Jet A flame array shows weaker flame interaction strengths and smaller recirculation zones compared to those of the methane flame array. The fluctuating mode structures (POD modes 1, 2, and 3) also reveal distinct layers at the flame shear layer region and small fluctuating structures in the methane flame array. On the other hand, distinct fluctuating structures are observed even at the center flame zone for the Jet A flame array due to weaker flame interactions. The leftmost flame region shows very a large fluctuating structure that overlaps the recirculation zone. Overall fluctuating mode energies and their corresponding structures were larger for the Jet A flame array compared to those of the methane flame array. These results are attributed to differences in fuel reactivity and flame stabilization structure on the mesoscale burner array.

4.4. Conclusions

In this work, Jet A fuel in a mesoscale burner array has been studied for compact-scale combustion system applications. Overall lean blow-off characteristics and flame dynamics were compared to a gaseous single-component fuel, methane. Results show that the Jet A fuel should be vaporized for stable combustion operations. While inlet mixture temperature had a significant impact on lean blow-off characteristics, injected fuel temperature did not. OH-PLIF images showed that recirculation zones in the Jet A flame array are much narrower compared to those of the methane flame array. The Jet A flames exhibit large flame fluctuations and are more susceptibility to flame blowout under fuel lean operations. Our work has shown that higher inlet temperatures can improve Jet A flame stabilization. The Jet A mesoscale flame characteristics are also studied using high-speed OH-PLIF imaging and POD analysis. The fuel and OH fluorescence can be visualized simultaneously to better understand the reaction processes of Jet A flame within the mesoscale burner array. Near the lean blow-off limit, narrow flame structures with reduced recirculation zone are observed. The POD analysis shows that fluctuating mode energies of the Jet A flame array are much greater than those of the methane flame array.

CHAPTER 5. HYDROGEN ENHANCEMENT ON A MESOSCALE SWIRL-STABILIZED BURNER ARRAY

This chapter presents a study of hydrogen-enhanced methane flames in a compact mesoscale burner array, where even a minute addition of hydrogen can significantly improve flame stability with reduced combustion length scale thereby enabling volumetric flexibility in small-scale combustion systems. The effect of hydrogen enhancement is demonstrated through combustion reaction length scale and operation limit analysis using methane fuel. The added hydrogen lowered lean blow off equivalence ratios, increased flame temperatures, and shorten the flame length scale, ultimately producing a denser flame array. 10 kHz OH* chemiluminescence and OH planar laser-induced fluorescence imaging techniques were used to estimate heat release rate and visualize flame structures. Hydrogen addition increased the OH intensity and decreased global heat release rate fluctuation, and also showed more stable operation under acoustic perturbations. Hydrogen enhancement can be a promising solution for reducing geometric constraints and improving operating capabilities for compact propulsion and power generation systems.

5.1. Introduction

Considerable efforts have been made to develop small-scale combustion systems with high operational stability and efficiency [81]. In small-scale combustion applications, minute flames in compact geometries are susceptible to thermal quenching and potential extinction mechanisms which can ultimately affect flame stability [3-5]. Furthermore, compact burner dimensions may limit fuel/oxidizer mixing and induce short residence times, thereby compromising efficient and stable combustor operations [6]. The reduced residence time can also result in the insufficient chemical reaction time scale inside the compact combustors that may induce flame extinction, incomplete heat generation, and unsteady combustion dynamics [20-22]. Therefore, overcoming these aforementioned challenges is critical for the successful implementation of stable burner operations in small-scale combustion systems.

A promising solution for improving stability in small-scale combustion systems is to add hydrogen to the fuel since hydrogen has better ignitability and reactivity than any other hydrocarbon fuels [101, 102]. However, using pure hydrogen would require a complete redesign of the combustor as well and suffers from other disadvantages such as safety and storage issues. Therefore, mixing adequate amounts of hydrogen into hydrocarbon fuels can be a minimally disruptive solution for improving the flame stability in small-scale combustion systems. Hydrogen addition to hydrocarbon fuels may further increase the flame temperature and dramatically lower the lean blow off equivalence ratio, enabling emission reduction [101, 103-105]. Furthermore, OH concentrations can be dramatically increased by adding 20% hydrogen to methane fuel [103] which can expedite the oxidation process from CO to CO_2, thereby enhancing combustion efficiency [106].

Studies of hydrogen addition to natural gas for gas turbine operations have yielded similar burner performance improvements [107-110]. When hydrogen is added, fuel properties undergo intrinsic changes and directly alter the flame structure. Furthermore, researchers have reported that changes in flame stabilization locations and flame shapes can ultimately affect flame dynamics, which drives the thermoacoustic coupling inside a combustor [111-113]. Previous research also showed that swirl-stabilized flames induce stronger flame attachment on the nozzle thereby producing stronger combustion intensity when hydrogen is added to the methane fuel [114]. Overall, hydrogen enrichment is a promising method for reducing combustion emissions under lean operations due to increased flame extinction strain rates [115].

Another strategy for improving flame stability under lean operations for gas turbines is a swirl burner. Conventional gas turbine combustors are operated normally using a large single swirl burner, exploiting flow recirculation to achieve leaner operations. However, lean combustor operations are more susceptible to combustion instabilities. For better stability under lean operations, multiple burner combustors are widely being adopted in gas turbines [45-48]. Additionally, multi-burner systems can also be scaled down for reducing overall combustor length scale without any performance degradations [50, 56]. Thus, mesoscale burner arrays have been developed by further reducing combustor dimensions and improving stability for highly efficiency and small combustion applications over a wide range of operating conditions [24, 52]. While more studies are required to better understand and utilize these phenomena on mesoscale burner arrays, experimental studies on hydrogen addition has been very limited, which may have inhibited the development of highly stable and efficient small-scale combustion systems. Therefore, a combination of hydrogen enhancement and mesoscale burner array can improve overall flame stability under lean operation due to increased reactivity in small-scale combustor applications.

In this study, the effects of hydrogen enrichment on mesoscale burner array flame dynamics and stability were experimentally studied. A mesoscale burner array based on mesoscale swirl-stabilized flame interaction has been developed to enhance combustion performance and stability in small energy systems [45-48, 50]. A counter rotating swirl configuration was adopted to enhance flame-to-flame interactions. The mesoscale burner array reduced overall combustor length scale without performance degradations compared to a single swirl burner [24, 52] with similar power inputs. The effects of hydrogen enrichment on the mesoscale burner array were studied using several experimental techniques. First, the mesoscale burner array performance was characterized by observing its lean blow off limit and flame temperature measurement variations from 0 to 50% volumetric hydrogen fractions. Second, 10 kHz high speed images of OH* chemiluminescence and OH planar laser-induced fluorescence (PLIF) were used to study flame structures and length scale variations due to hydrogen enrichment. Finally, flame stability analysis was carried out by monitoring the flame response under transverse acoustic forcing at 210 Hz.

5.2. Experimental setup

5.2.1. Mesoscale burner array

The mesoscale burner array consists of 4 by 4 burner elements. The burner cross-section in Figure 5.1 (a) shows bluff bodies, fuel flow paths, air flow paths, and swirl structures. The burner center to burner center distance is 9 mm. The fuel was injected through a fuel manifold that is connected to the bluff bodies. The schematic and design parameters of the mesoscale burner element are shown in Figure 5.1 (b) and Table 5.1, respectively, and more details are also provided in our previous research about diffusion type mesoscale burner array [116]. In the case of the

mesoscale burner array, the dimensions and spacing between individual burner elements are on the order of 1cm. The mesoscale burner array concept has been developed to improve flame interactions and reduce flame length scale.

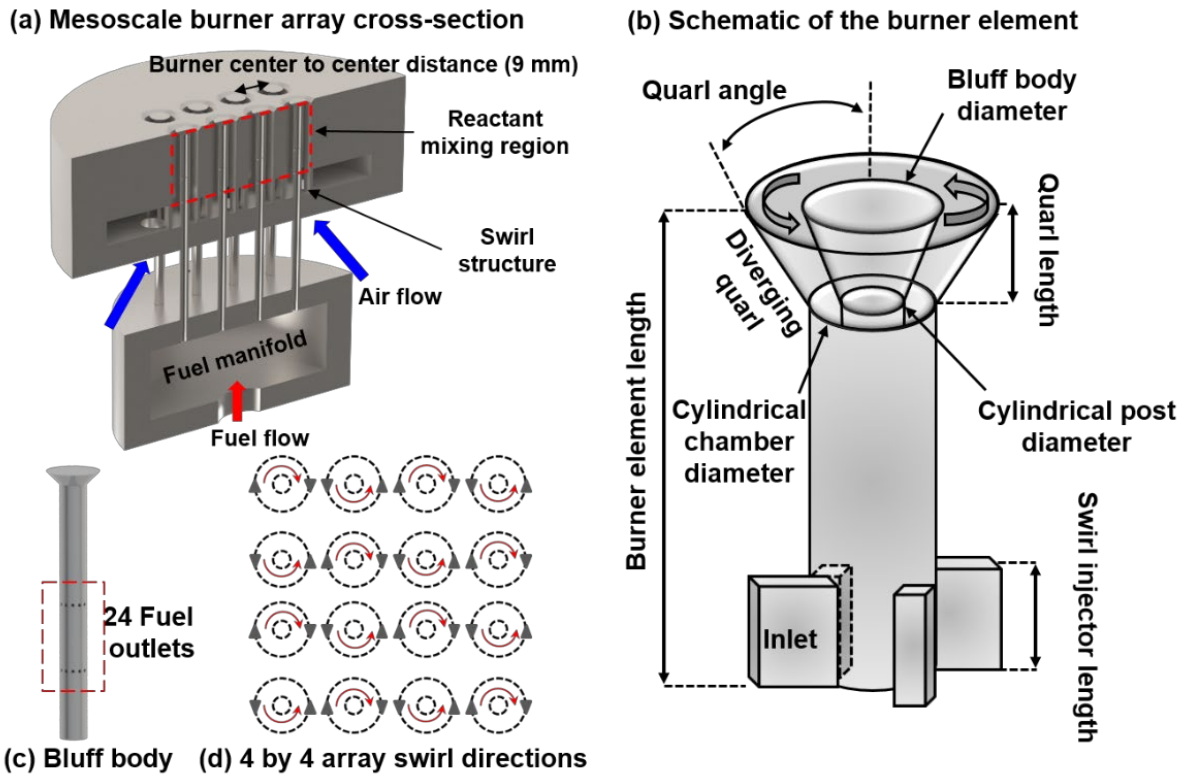

Figure 5.1. (a) Sectional view of the mesoscale burner array, (b) Schematic of the burner element, (c) Bluff body design for fuel injection, and (d) Swirl directions.

Parameter	Value
Quarl included angle (degrees)	45
Quarl length (mm)	1
Bluff body diameter (mm)	4
Cylindrical post diameter (mm)	2
Cylindrical chamber diameter (mm)	6
Burner element length (mm)	20
Swirl injector length (mm)	5

Table 5.1. Design parameters for the mesoscale burner element.

Each burner element has a bluff body with 24 fuel injection ports, machined by electrical discharge machining (EDM), as shown in Figure 5.1 (c). The injection port diameter is 250 μm and ensures uniform mixing behavior inside the mesoscale burner array architecture. Radially injected fuel is mixed with swirling air from two tangential inlets in each burner element and produces swirl-stabilized flame on each bluff body. This unique burner array design can prevent flame flashback, attributed to hydrogen addition. As shown in Figure 5.1 (d), burner elements were arranged in an array of counter-rotating swirl directions known as the Taylor-Green vortex arrangement to improve mesoscale flame interactions [24, 56]. The mesoscale burner array was mounted onto a custom-built plenum [116] and air and fuel mixture (methane and hydrogen) were supplied by dedicated MKS mass flow controllers. The volumetric fraction of hydrogen (X_{H2}) in the mixture was controlled from 0 to 50%.

5.2.2. Laser diagnostics

10 kHz OH* chemiluminescence and OH-PLIF imaging were performed to visualize flame structures and estimate heat release rates. The experimental setup is shown in Figure 5.2. OH* chemiluminescence and OH-PLIF were filtered using an Asahi band-pass filter with 10 nm of FWHM at 310 nm. A Lavision image intensifier, a Photron SA-Z CMOS camera, and Sodern Cerco UV lens (100mm f/2.8) were used to image the filtered OH* chemiluminescence and OH fluorescence.

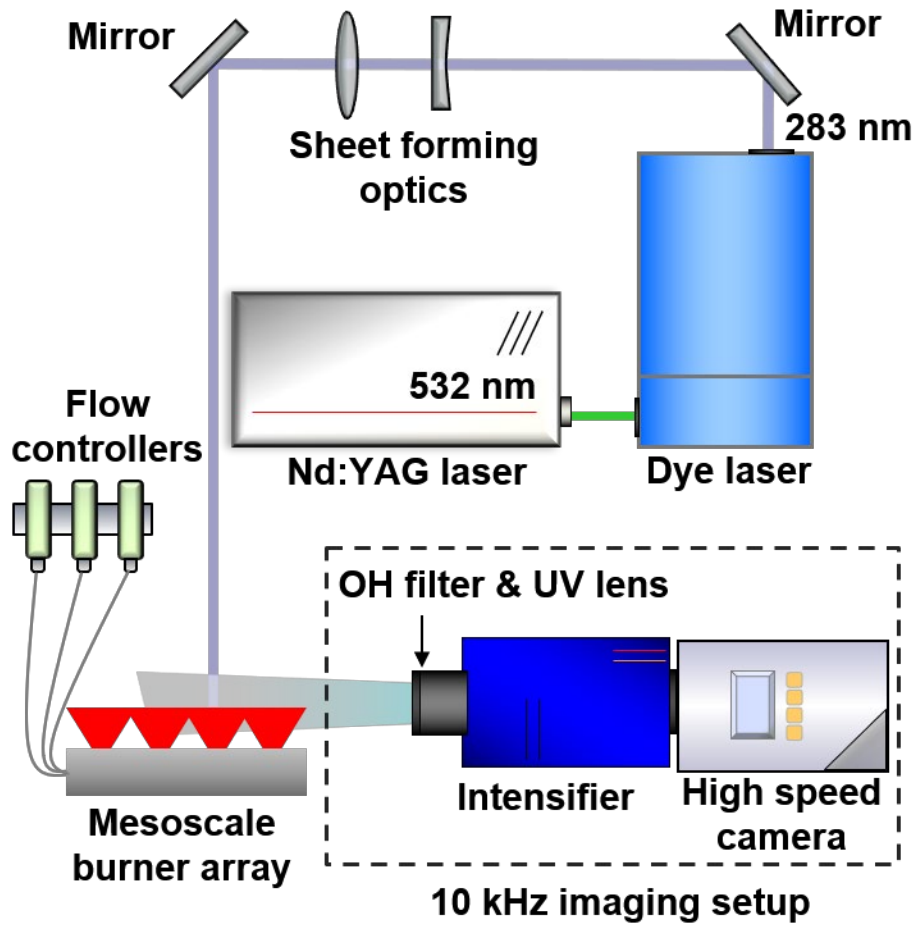

Figure 5.2. Schematic of the imaging setup for OH chemiluminescence and OH-PLIF.*

For OH excitation, a dye laser (Credo dye laser, Sirah) with Rhodamine 6G dye dissolved in ethanol was pumped by a 532 nm solid state Nd:YAG laser (Innoslab IS200-2-L, EdgeWave). The red dye laser beam was frequency doubled using a BBO doubling crystal. The frequency doubled laser output was controlled to excite the Q_1 (6) line of the $A^2\Sigma^+$-$X^2\Pi$ (1, 0) OH band. Sheet forming optics transform the UV output beam into a thin laser sheet (120 μm of FWHM, ~ 60 mm in height). The laser sheet was routed from above the burner chamber down towards the burner surface to allow for transverse acoustic forcing.

5.2.3. Acoustic forcing setup

Transverse acoustic forcing was imposed onto the mesoscale flame array by two 50 W woofer speakers (DS135-8 5" Designer Series Woofer Speaker, Dayton Audio) as shown in Figure 5.3 (a). The two speakers were attached onto the side walls to create a standing wave inside the chamber. The wall-to-wall distance was 127 mm. The speaker amplitude and frequency were controlled by a 1400 W power amplifier (PTA1400, Pyle) and LabVIEW software (National Instruments). The two speakers produced a pressure antinode of sinusoidal standing wave at 210 Hz located above the center of the burner array as shown in Figure 5.3 (b). The forcing frequency of 210 Hz was selected due to the sensitive mesoscale flame response near this frequency based on our previous research [56]. The acoustic excitation induced a pressure oscillation, resulting in an axial velocity fluctuation, on the burner array and a longitudinal flame fluctuation was observed. In this study, any transverse pressure oscillation can be negligible at the pressure antinode due to the smaller geometric dimension of the burner array compared to the acoustic wavelength at 210 Hz (1.64 m). Flame array responses as a result of acoustic perturbation were imaged through an optically accessible quartz window to study the effects of hydrogen addition on flame stability.

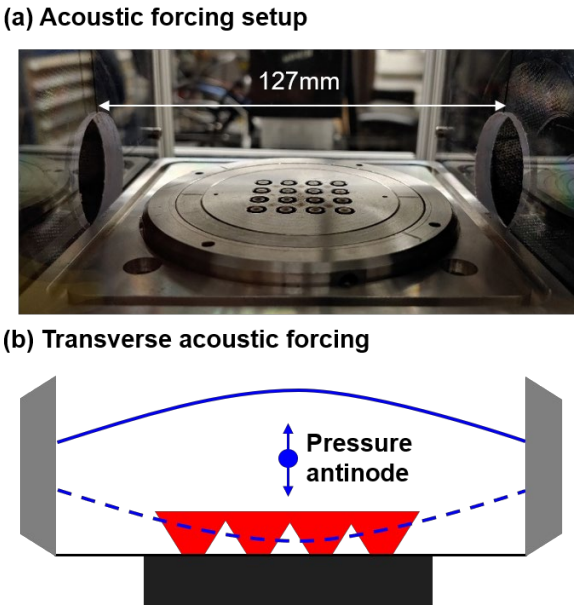

Figure 5.3. (a) Acoustic forcing setup using two speakers and (b) Transverse acoustic forcing mode.

5.3. Results and discussion

5.3.1. Visible flame image

Visible mesoscale flame array images show the effect of hydrogen enrichment in Figure 5.4. The flame arrays were maintained at an equivalence of 0.7 and the air flowrate was set to 60 SLPM. Volumetric hydrogen fractions from 0 to 50% were employed and a dramatic reduction in overall flame length scale was observed. At X_{H2} = 0%, the flames exhibited stretched flame structures. At X_{H2} = 50%, denser combustion structures were observed much closer to the burner surface. Reduced flame length scales can be directly correlated to the higher hydrogen content in the fuel mixture leading to an increase in the adiabatic flame temperature as well as the overall burning rate [117, 118]. Shorter flame length scales can be beneficial when designing a small-scale

combustor since the overall reduction in the combustor length scale reduces the volume and weight of the entire combustor system.

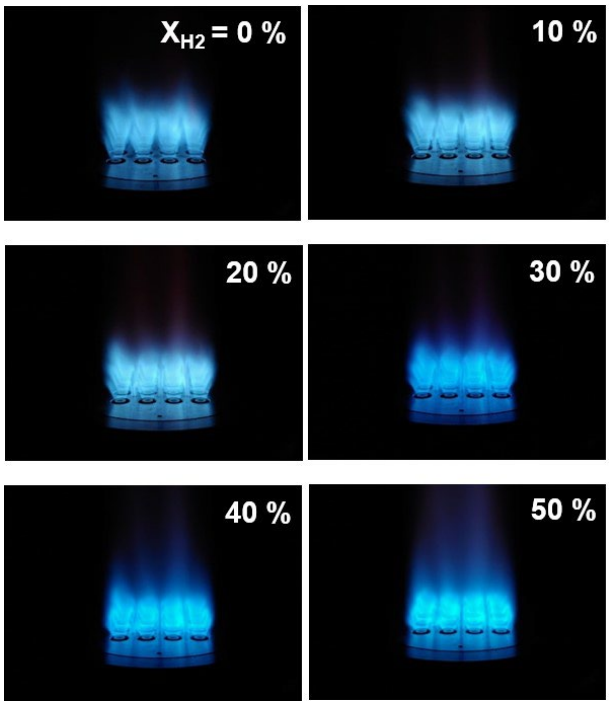

Figure 5.4. Visible images of hydrogen enriched flame arrays at an equivalence ratio of 0.7.

5.3.2. Lean blow off limit

Figure 5.5 shows lean blow off (LBO) equivalence ratios of hydrogen-enriched flame arrays with varying amounts of volumetric hydrogen fraction (0 – 50%) and constant thermal input power of 3 kW. Volumetric hydrogen fraction was controlled by adjusting the methane and hydrogen flow rates as listed in Table 5.2. Following this, the air flow rate was gradually increased to trigger the flame lift off under fuel lean conditions. The mesoscale flame arrays started to blow off partially from one of the burner array edge elements (partial blow off). As the air flow rate continued to increase, the flame arrays were completely lifted from the burner (total blow off). The

figure clearly shows that an increase in hydrogen fraction leads to a decrease in both the partial and total lean blow off equivalence ratios. It is known that hydrogen enriched fuel can withstand higher strain rates before flame extinction [106]. For pure methane flames, the partial and total flame lift off were observed at an equivalence ratio 0.618 and 0.538, respectively. The lean blow off equivalence ratios dramatically decreased to 0.295 (partial blow off) and 0.273 (total blow off) at 50% volumetric hydrogen fraction. The reduction in LBO limits is attributed to the increased burning rate of reactant due to hydrogen addition [117, 118]. Furthermore, hydrogen enrichment reduced the difference in the equivalence ratio between the partial lift off and the total blow off limits. This implies that hydrogen addition can provide a more stable operation under ultra-lean conditions for reducing emissions.

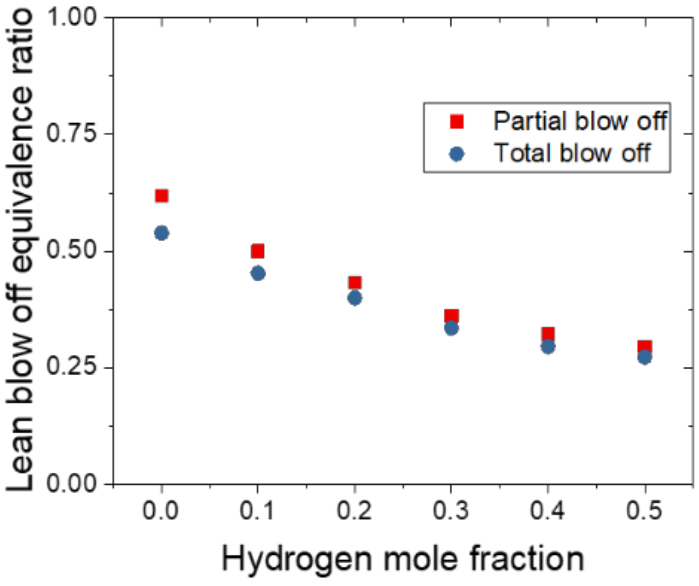

Figure 5.5. Lean blow off equivalence ratios as a function of hydrogen addition at 3 kW thermal input.

H2 volume fraction	CH4 (SLPM)	H2 (SLPM)
0	5	0
0.1	4.85	0.54
0.2	4.66	1.17
0.3	4.45	1.91
0.4	4.20	2.80
0.5	3.87	3.87

Table 5.2. Hydrogen and methane flow rates at 3 kW thermal input.

5.3.3. Temperature measurement

Flame temperature measurements were carried out to characterize the effect of hydrogen enrichment on the mesoscale burner array. Flame temperature profiles can help determine the flame array uniformity and its thermal performance. Figure 5.6 shows temperature profile measurements along the centerline at a height of z = 5 cm above the burner surface. A type R thermocouple (Nordic Sensors) was used to measure the flame temperature. All temperature measurements were corrected for radiation loss as the same calculation method in [24]. Conduction loss was neglected due to aligned thermocouple wires along isotherms and the catalytic effect was also neglected because the temperature measurements were carried out above the combustion reaction region. Therefore, only convection-radiation energy balance [119] was considered for radiation losses using the following equations.

$$T_g = T_b + \frac{\varepsilon_b \sigma D_b}{Nu_D k_g}(T_b^4 - T_\infty^4) \qquad (1)$$

Where T_g the corrected gas temperature, T_b measured thermocouple temperature, T_∞ ambient temperature, ε_b emissivity of the platinum bead, σ Stefan-Boltzmann constant (5.67×10^{-8} W m^{-2} K^{-4}), D_b bead diameter, Nu_D Nusselt number at the bead, and k_g thermal conductivity of the gas.

$$Nu_D = 2 + \left(0.4Re_D^{\frac{1}{2}} + 0.06Re_D^{\frac{2}{3}}\right) Pr^4 \left(\frac{\mu}{\mu_s}\right)^{\frac{1}{4}} \text{ (For } 0.71<Pr<380;\ 3.5<Re_D<76000;$$

$$1.0<\left(\frac{\mu}{\mu_s}\right)<3.2) \quad (2)$$

Where Re_D Reynolds number at the bead, Pr Prandtl number at the bead, μ dynamic viscosity of the gas at T_g, and μ_s dynamic viscosity of the gas at T_b.

The bead emissivity (ε_b) was calculated using the equation [120]:

$$\varepsilon_b = 1.108 \times 10^{-4} T_b + 0.014 \quad (3)$$

For the operating conditions, the temperature difference between the measured thermocouple temperature and the corrected gas temperature ranges from ~100 to 200 K.

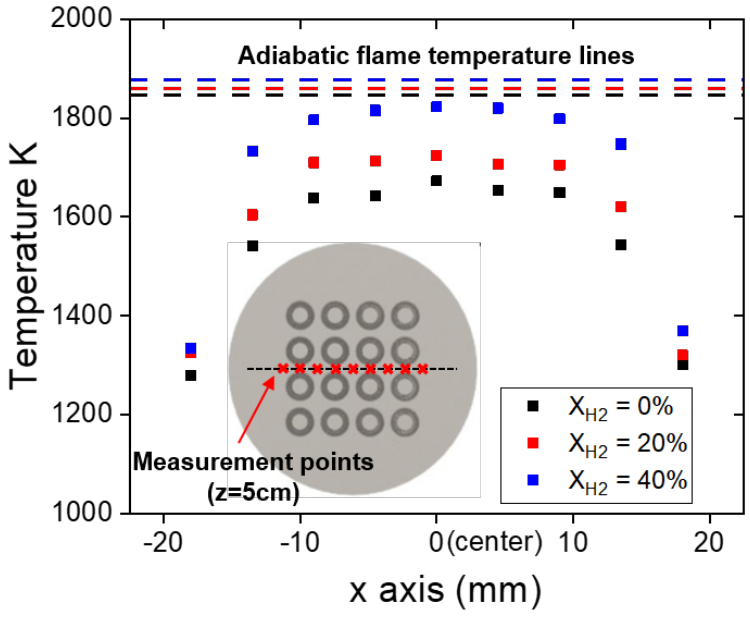

Figure 5.6. Spatial temperature profiles along the burner centerline for various volumetric hydrogen fractions at ϕ = 0.7 and air flowrate = 60 SLPM.

Mostly uniform temperature profiles were observed at the burner center region, with the maximum temperatures at the very center of the burner. Flame temperatures gradually decreased as we moved the thermocouple away from the burner center and toward the outer burner elements due to greater heat loss and weaker flame interactions. The dashed lines in Figure 5.6 represent the adiabatic flame temperatures under various volumetric hydrogen fractions at an equivalence ratio of 0.7. The added hydrogen can raise the adiabatic flame temperature since hydrogen has a higher adiabatic flame temperature than methane at the same equivalence ratio [117]. The maximum flame temperatures at 0, 20, and 40% hydrogen fractions were 1673.2, 1724.2, and 1822.9 K, respectively. Furthermore, flames with higher hydrogen fractions produced temperature profiles that were closer to their adiabatic flame temperatures. This is due to hydrogen enrichment reducing the overall flame length scale and contributing towards a more efficient combustion process. Overall, hydrogen enrichment can promote more effective combustion processes under fuel lean operations without the need for increasing the equivalence ratio by adding more methane.

5.3.4. OH chemiluminescence and OH-PLIF imaging*

Figure 5.7 shows the averaged OH* chemiluminescence and OH-PLIF images of the mesoscale flame array under various hydrogen volumetric fractions from 0 to 50%. OH* chemiluminescence images can visualize the overall OH radical concentrations of the flame array and can be a good indicator of heat release rates during the combustion process [121, 122]. From Figure 5.7 (a), the methane flame array showed V-shaped flames due to swirl stabilization at 0% hydrogen volumetric fraction. As the hydrogen fraction increased from 10 to 50%, the flame length scale decreased. Simultaneously, the flame structure was converted from a V- to an M- shaped structure. Adding hydrogen to methane could significantly shorten the mesoscale flame reaction

length scale, so that the flame array looked almost flat at 50% hydrogen volumetric fraction. Since OH* chemiluminescence is a major spontaneous emission from combustion reactions [123], flame structures visualized by OH* directly represent the reduction in combustion reaction length scales due to hydrogen enrichment.

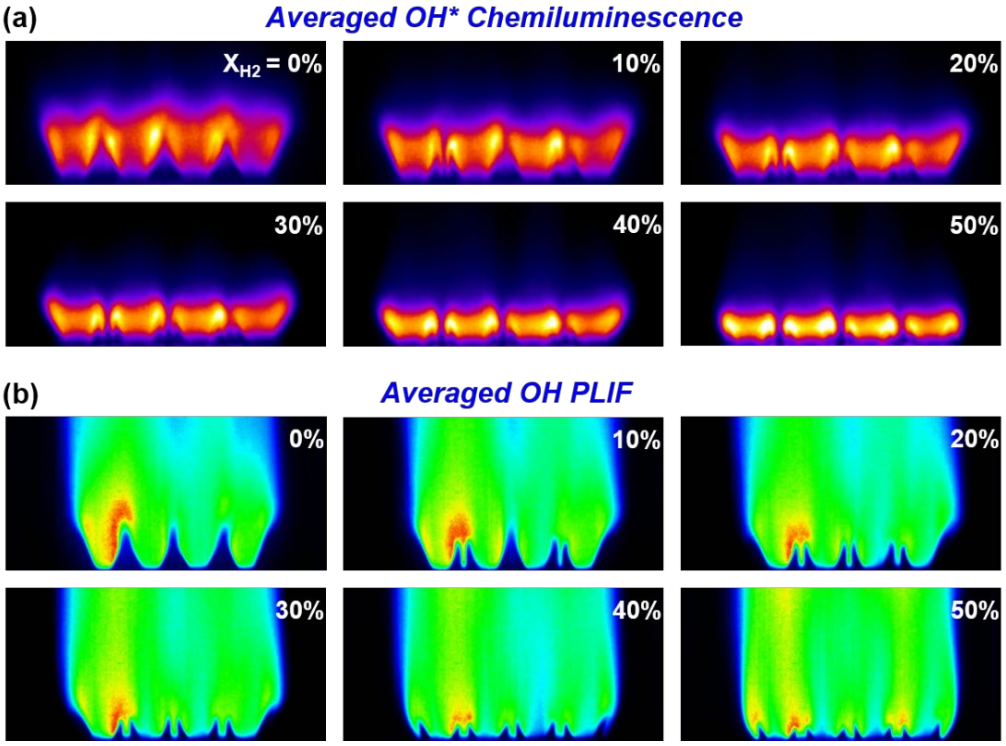

Figure 5.7. (a) Averaged images of OH chemiluminescence and (b) OH-PLIF at various hydrogen volumetric fractions at ϕ = 0.7 and air flowrate = 60 SLPM.*

OH-PLIF images under the same operating conditions are provided in Figure 5.7 (b). OH-PLIF images were taken along the centerline of the second row of the burner array, dissecting four burner elements and their bluff bodies. As shown in the OH* chemiluminescence images, V-shaped flame structures were also observed in the pure methane flame array, and individual flames interacted well with neighboring elements. The V-shaped flame was the result of flow interaction

between the center recirculation flow and the inner shear layer on the bluff body [56]. As the hydrogen volumetric fraction increased between 0 and 20%, flame merging points started to attach to the burner surface due to increased reactivity and laminar flame speed. The V- to M-shape flame structure transition was completed by X_{H2} = 20% as each flame on the mesoscale burner array attached to the burner surface between neighboring burner elements due to its interaction with their respective neighboring flames. Further increase in hydrogen volumetric fraction pushed the M-shaped flame further down towards the burner surface. This flame shape transition can also be observed in methane mesoscale flames by increasing the operating equivalence ratio which results in higher flame speeds [56]. These results show that highly efficient small-scale combustion systems are feasible due to the extreme reduction of combustion reaction length scale under hydrogen-enriched fuel-lean operations.

The length scale of the mesoscale flame array can be identified by plotting the vertical OH* chemiluminescence intensity from the burner surface as shown in Figure 5.8 (a). OH* chemiluminescence intensities along every row of an image were integrated into a vertical profile along the burner axial direction. The distance from the burner surface to each peak in Figure 5.8 (a) is a good representation of the flame length scale for the pure methane flame array (0%) and hydrogen-enriched flame arrays (20 and 40%). As expected from Figure 5.7, the overall flame length scale decreased with increasing hydrogen volumetric fraction. The flame length scale of 40% hydrogen-enriched flame array was nearly half that of the pure methane flame array. Moreover, the peak OH* intensity value of 40% hydrogen enriched flame array exhibited much higher OH* concentration compared to that of a pure methane flame array. This result indicates that denser flames can be achieved by using a hybrid fuel, a combination of methane and hydrogen.

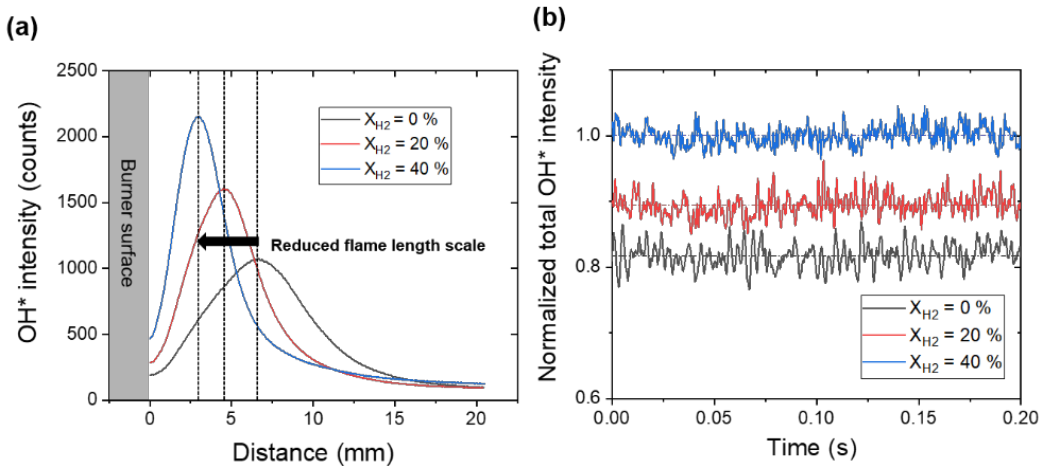

Figure 5.8. (a) Vertical OH chemiluminescence profiles in various hydrogen-enriched flame arrays and (b) Normalized integrated OH* intensity as an indicator of heat release rate at ϕ = 0.7 and air flowrate = 60 SLPM.*

10 kHz normalized OH* chemiluminescence intensities were traced for 0.2 s under various hydrogen volumetric fractions (0, 20, and 40%) in Figure 5.8 (b). OH* chemiluminescence counts were integrated across an entire single snapshot OH* chemiluminescence image to infer the OH* chemiluminescence intensity at each time step, which is an indicator of the total heat release rate of the mesoscale flame array. The OH* chemiluminescence intensity was then normalized against the averaged OH* chemiluminescence intensity of the 40% hydrogen flame array. The averaged normalized OH* values, calculated by averaging 2000 OH* chemiluminescence images, were 0.817, 0.895, 1.000 at 0, 20, 40% hydrogen volumetric fraction, respectively, as shown by the dotted lines in the figure. The results show that elevated OH* radical concentrations can be achieved through hydrogen addition with the added benefit of reducing the flame length scale, which can ultimately improve the combustion efficiency by reducing the heat loss. The increase in OH* chemiluminescence can be interpreted as an increase in the heat release rate compared to

a pure methane flame array [124]. This also supports the increase in flame temperature measurements with hydrogen enrichment as described earlier in Figure 5.6.

5.3.5. Forcing response

A transverse acoustic perturbation at a frequency of 210 Hz was applied to study the longitudinal flame response of the mesoscale flame array at the pressure antinode. Figure 5.9 shows OH* chemiluminescence images of flames responding to the perturbation under various hydrogen volumetric fractions. Under the acoustic forcing condition, the flame length scale was reduced with increasing hydrogen volumetric fractions from 0 to 40% as was observed in the absence of perturbation. M-shaped flame structures were also observed at X_{H2} = 20 and 40%.

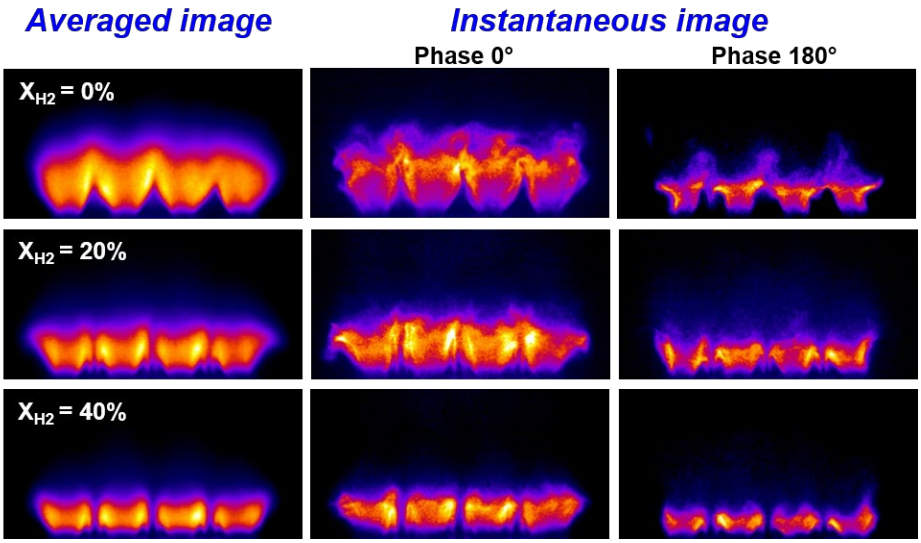

Figure 5.9. OH chemiluminescence images under 210 Hz acoustic forcing at ϕ = 0.7 and air flowrate = 60 SLPM.*

Instantaneous images in Figure 5.9 show the flame fluctuations over a single period induced by the acoustic forcing. The highest OH* intensity was observed at 0° phase. The lowest OH* intensity was observed along with the smallest flame structures at 180° phase. The largest flame surface fluctuation was observed under a pure methane flame array. The results show that a well attached M-shaped flame array under higher hydrogen volumetric fraction can be more resilient to acoustically induced perturbations with smaller flame surface fluctuations compared to a pure methane flame array.

The flame response can also be characterized by plotting the vertical OH* chemiluminescence intensity from the burner surface. Figure 5.10 shows similar trends in the vertical profiles of integrated OH* chemiluminescence intensities as was observed in the absence of acoustic forcing. With 40% hydrogen volumetric fraction, the flame array exhibited the shortest flame length scale and the highest OH* intensity compared to those of 20 and 0%. Overall, hydrogen enrichment can be beneficial for compact combustors with little to no performance degradation in both quiescent and acoustically perturbed environments.

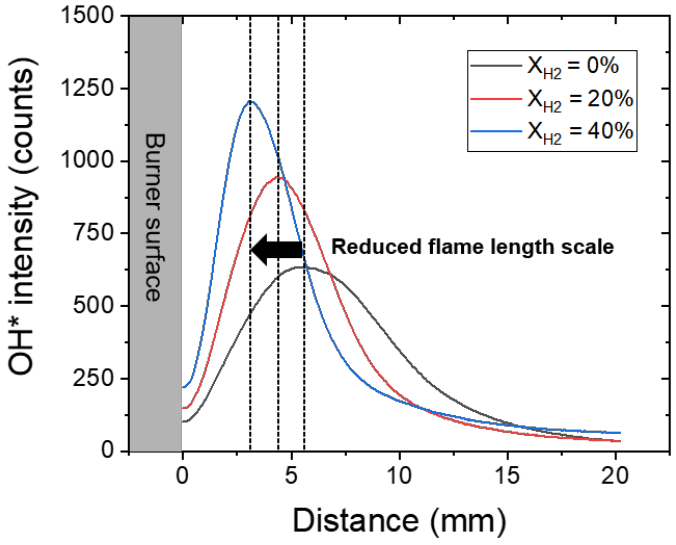

Figure 5.10. Vertical OH chemiluminescence profiles under 210 Hz acoustic forcing at ϕ = 0.7 and air flowrate = 60 SLPM.*

For better insight into the effect of hydrogen enrichment on flame dynamics, a trace of global heat release rate fluctuations can be calculated by normalizing OH* intensity fluctuations to the average OH* intensity across a set of consecutive images. The results in Figure 5.11 show the effect of hydrogen enrichment on the heat release rate fluctuation of the mesoscale flame array.

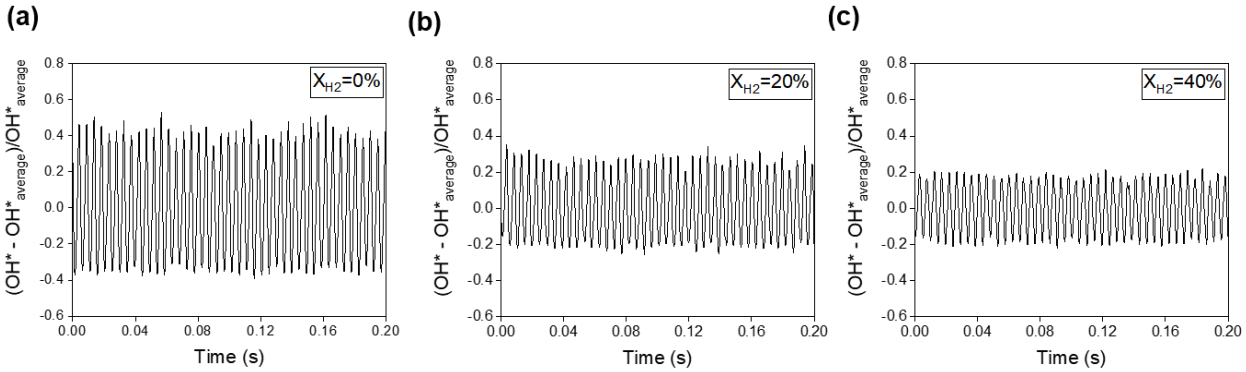

Figure 5.11. Global heat release rate fluctuations in various hydrogen fractions by 210 Hz acoustic forcing at ϕ = 0.7 and air flowrate = 60 SLPM.

A total of 2000 images were taken at 10 kHz and processed for 0, 20, and 40% hydrogen volumetric fraction flame arrays. Based on the analysis, the frequency of the flame response coincided with the forcing frequency of 210 Hz as expected. Flames with higher hydrogen content showed smaller global heat fluctuations ($\{OH^*-OH^*_{average}\}/OH^*_{average}$) indicating smaller heat release rate fluctuations. This result shows that flame surface fluctuations can be minimized by hydrogen enrichment which is likely due to the higher flame speed triggering the V- to M- flame structure transition. Ultimately, hydrogen addition in a mesoscale burner array induces reduction in both flame length scale and heat release rate fluctuations.

Instantaneous OH-PLIF images across an acoustic perturbation cycle at 210Hz are shown in Figure 5.12. The overall heat release rate fluctuations were closely correlated to the forcing and flames with higher hydrogen content were more robust to acoustic forcing. The OH-PLIF images visualized axially perturbed flame responses over the centerline of the second row in the burner array. And the initial phase (0°) was given to an image that had the peak integrated OH intensity over a single acoustic forcing cycle.

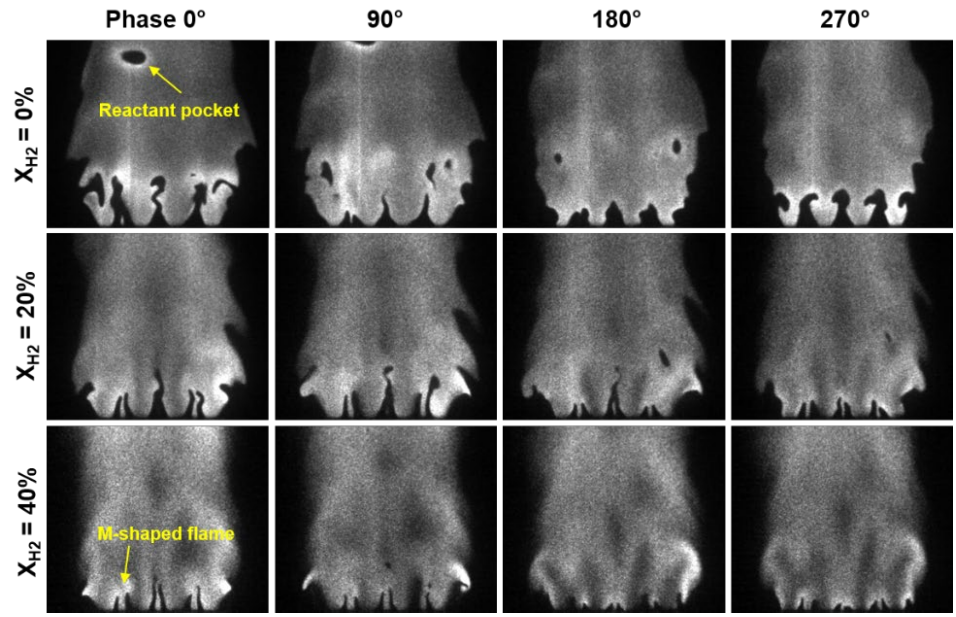

Figure 5.12. Instantaneous OH-PLIF images during a perturbation cycle (210Hz) at ϕ = 0.7 and air flowrate = 60 SLPM.

V-shaped flame structures were well stabilized on each bluff body during the perturbation cycle in case of the methane flame array. Large fluctuation at the shear layer and interaction region induced the unburnt reactant pockets. At X_{H2} = 20%, flame attaching at flame interaction regions was observed. At X_{H2} = 40%, flame structures appeared wider than methane flames and the

reaction length scale became shorter with smaller surface area changes due to the well-anchored M-shaped flame structures. M-shaped flames are triggered by hydrogen addition that increases the burning speed resulting in flames that are more robust against axially-perturbed velocity fluctuations.

5.4. Conclusions

The effects of hydrogen enrichment on methane flames in a mesoscale burner array have been investigated. Lean blow off characteristics, flame temperatures, OH* chemiluminescence, and OH-PLIF were used to analyze flame stability and flame dynamics. Hydrogen enrichment further reduced the flame length scale on the mesoscale burner array. The overall flame length scale was dramatically reduced as evidenced by the vertical OH* chemiluminescence profiles. Such a reduction is an important design criterion for the development of compact combustors. Also, leaner LBO equivalence ratios and higher flame temperatures were obtained through hydrogen enrichment. Total OH radical concentrations, a key indicator of combustion heat release rate, increased with increasing hydrogen volumetric fraction. OH-PLIF images showed that flame interactions and flame merging lengths of hydrogen-enriched flames became stronger and shorter, respectively, with higher hydrogen content compared to a pure methane flame array. Higher hydrogen volumetric fraction improved flame stability by reducing flame surface and global heat release rate fluctuations under acoustic perturbation at 210 Hz. Increased reactivity in fuels with higher hydrogen content can significantly improve flame stability, particularly in mesoscale combustion systems. Therefore, methane fuel combined with hydrogen has a potential to improve the performance and stability of a mesoscale burner array for small-scale combustion system applications.

CHAPTER 6. EFFECTS OF HYDROGEN ENHANCEMENT ON MESOSCALE BURNER ARRAY FLAME STABILITY UNDER ACOUSTIC PERTURBATIONS

Partial substitution of hydrocarbon fuel with hydrogen can effectively improve small-scale combustion system stability and performance, potentially opening the way for novel compact power generation and/or propulsion systems in the future. In this study, the effects of hydrogen enhancement between 0% and 40% hydrogen volumetric fractions in methane fuel were experimentally observed in a mesoscale burner array subjected to external acoustic perturbations. The mesoscale burner array utilizes an array of swirl-stabilized burner elements and their interactions with neighboring elements to improve the overall flame stability and simultaneously reduces the combustor length scale. OH* chemiluminescence and OH planar laser-induced fluorescence (OH-PLIF) were used to image various hydrogen-enriched flames at an equivalence ratio of 0.7, subjected to transverse acoustic perturbations at 320 Hz. Two acoustic modes were imposed by controlling the phase difference between two speakers perturbing the flow. OH* chemiluminescence images exhibited flame length scale reduction, leading to a denser flame array. Also, flame arrays with higher hydrogen enrichment were found to be more robust against transverse acoustic perturbations, demonstrated by reduced fluctuations in the global heat release rate. OH-PLIF images showed that flames with higher hydrogen enrichment initiated V- to M-shaped flame shape transition even under fuel lean conditions, thereby improving the combustion stability. OH-PLIF images were also used for flame stability analysis through spectral proper orthogonal decomposition (SPOD). The SPOD analysis showed hydrogen enrichment diminished flame fluctuation structures under fuel lean operations.

6.1. Introduction

Most compact combustor designs have been motivated by the fact that energy densities of hydrocarbon (HC) fuels are one to two orders of magnitude greater than those of modern batteries or fuel cells [1, 2]. Even accounting for conversion losses, HC fuels can easily outperform other power sources in practical applications. However, a number of technical challenges should be addressed for compact and high-efficiency combustors to be truly viable. Smaller flames in compact geometries are susceptible to thermal and chemical quenching that can affect burner stability [3-5]. The smaller burner dimensions may further limit the fuel and oxidizer mixing process by inducing a shorter residence time inside the combustor and compromising stable burner operation [6]. The reduced residence time, if comparable to the characteristic chemical reaction timescale of the fuel-air mixture, may induce incomplete combustion reaction and flame extinction [20-22].

An approach recently being developed is a mesoscale burner array built with additive manufacturing [24, 56]. The mesoscale burner array adopts an array of bluff body swirl-stabilized burner elements by enhancing flame interactions. However, intrinsic physicochemical characteristics and aforementioned challenges of small burner geometries can nevertheless prohibit successful burner operation under fuel lean conditions. In combustors, fuel lean operation is susceptible to combustion instabilities attributed to thermo-acoustic coupling inside the combustor, thereby resulting in flame blow out and performance degradation [18, 125-128]. These issues must be addressed for mesoscale burner arrays to be widely adopted in small-scale combustion systems ranging from portable energy sources to micro gas turbine combustors.

One approach for enhancing stable fuel lean operation in compact burners is to improve combustion reactivity by substituting some of the fuel with hydrogen since it has better reactivity

than conventional hydrocarbon fuels [101, 102]. The combustion reaction rate can be accelerated by adding hydrogen due to increased H, O, and OH radical generation [129]. Furthermore, combustion efficiency can be dramatically improved due to higher OH radical production and more efficient oxidation process from CO to CO_2 as reported in [103, 106, 109, 110].

Many studies have examined the effects of hydrogen addition on swirl-stabilized flames for stable fuel lean operation. Hydrogen addition can improve combustion intensity and flame stability as well as mitigate NOx emission by significantly altering the flame stabilization structure [104, 111, 112]. Furthermore, hydrogen enrichment results in better flame holding and stabilization as well as mitigating emissions by reducing combustion gas temperatures, even under fuel lean conditions [101, 103-105, 114]. These results are also supported by a simulation study [106] that shows higher resistance to strain in hydrogen enhanced flames due to increased OH radicals. However, limited studies have been conducted on the effects of hydrogen enhancement on small-scale flame stability, particularly on swirl-stabilized burner arrays under fuel lean operation.

In this study, the effects of hydrogen enhancement on flame stability in the mesoscale burner array subjected to external perturbations were experimentally studied. The effects of two different transverse acoustic perturbation configurations, a pressure node and antinode, on the flame dynamics and stabilities were characterized. The pressure node and the antinode at 320 Hz perturbation frequency were imposed on a methane-air flame at an equivalence ratio of 0.7. The volumetric fractions of hydrogen in the fuel stream were controlled from 0% to 40%. OH* chemiluminescence imaging was employed to show flame length scale changes and global heat release fluctuations under various hydrogen enrichment and acoustic perturbation conditions. 10 kHz OH planar laser-induced fluorescence (OH-PLIF) imaging was used to visualize flame

responses as a result of acoustic perturbations. Lastly, the effects of hydrogen enrichment on the flame stability were examined using a spectral proper orthogonal decomposition (SPOD) analysis.

6.2. Experimental setup

6.2.1. Mesoscale burner array and optical diagnostics

Figure 6.1 (a) shows the top view of the mesoscale burner array equipped with 16 individual burner elements. The design parameters of the burner array can be found in our previous research [116]. Each burner element has a counter-rotating swirl direction noted by the yellow arrows in Figure 6.1 (a). This swirl arrangement enhances the burner stability by exploiting flame-to-flame interactions between neighboring burner elements [56]. Air and fuel are injected into the burner by MKS mass flow controllers. Burner operating conditions were set to an equivalence ratio of 0.7 and an air flow rate of 60 SLPM. The burner housing walls are made up of two optically accessible quartz glass plates to image the flame and two polycarbonate plates with cutouts for speakers to perturb the flame array as shown in Figure 6.1 (b). The wall-to-wall distance of the burner housing is 127 mm. Two 50 W woofer speakers (DS135-8 5" Designer Series Woofer Speaker, Dayton Audio) and a 1400 W power amplifier (PTA 1400, Pyle Pro) were used to acoustically-perturb the flame. The input signals to the speakers were generated using LabVIEW software (National Instruments).

A laser diagnostic setup for 10 kHz OH-PLIF and OH* chemiluminescence is introduced in Figure 6.1 (c). A dye laser (Credo dye laser, Sirah) and a pumping laser, 532 nm solid state Nd:YAG laser (Innoslab IS200-2-L, EdgeWave), were used to generate a 283 nm wavelength beam to excite the Q_1 (6) line of the $A^2\Sigma^+$-$X^2\Pi$ (1, 0) OH band for OH-PLIF imaging. A laser sheet (120 μm FWHM and 60 mm height) was formed by sheet forming optics and directed through a

mirror to the burner array from above the burner. OH-PLIF or OH* chemiluminescence signals were filtered through an Asahi band-pass filter (10 nm FWHM at 310nm) and imaged by an image intensifier (High-Speed IRO, LaVision) and a high speed camera (SA-Z, Photron) equipped with a 100mm f/2.8 UV lense (Sodern).

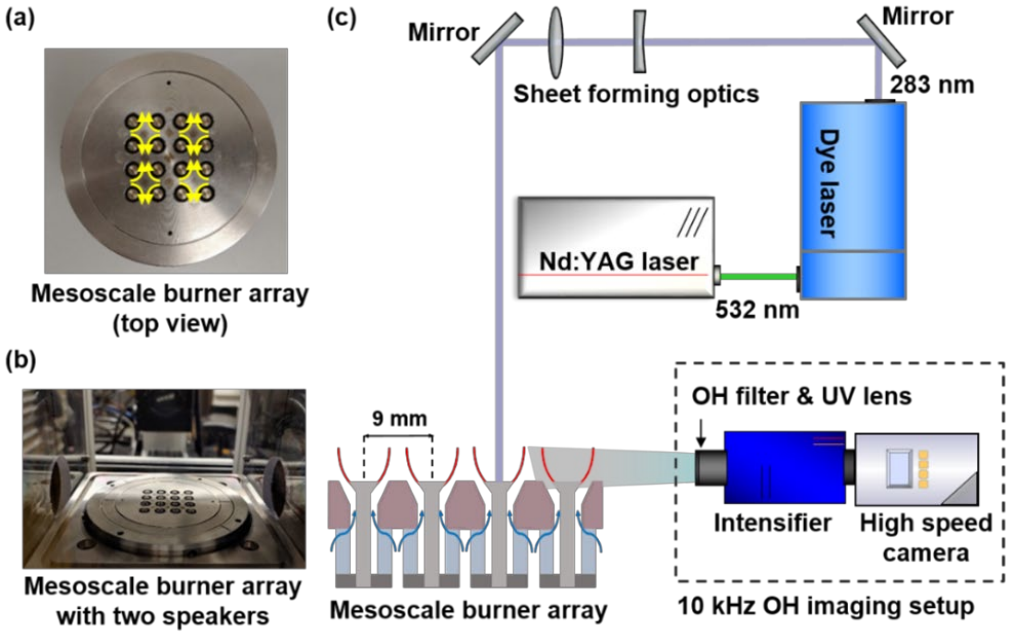

Figure 6.1. (a) Top view of the mesoscale burner array with swirl flow directions. (b) Mesoscale burner with the external speaker setup. (c) Schematic of the imaging setup for OH chemiluminescence and OH-PLIF.*

6.2.2. Acoustic perturbation configurations

Two acoustic perturbation configurations were used to study the flame dynamics as illustrated Figure 6.2. The two speakers generated sine waves at 320 Hz. Two sinusoidal standing waves were produced by changing the phase difference between the two speakers. When the phase difference is 0°, a pressure antinode was imposed at the center of the flame array. This

configuration axially-perturbed the flow by inducing large pressure fluctuations, corresponding to velocity fluctuations. When a pressure node was imposed at the center of the flame array due to a phase difference of 180°, the induced pressure fluctuations laterally-perturbed the mesoscale flame array. In this study, the two flame responses were examined using OH* chemiluminescence and OH-PLIF imaging as well as SPOD analysis to understand the effects of hydrogen addition on flame stability as a result of the two perturbation configurations.

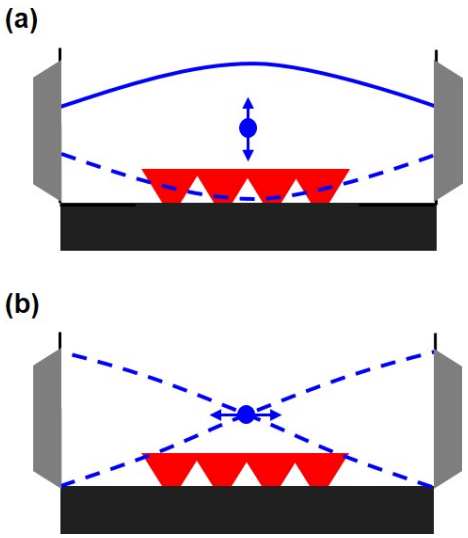

Figure 6.2. Acoustic perturbation configurations: (a) the pressure antinode (0° speaker phase difference) and (b) the pressure node (180° speaker phase difference) at the burner center.

6.3. Results and discussion

6.3.1. OH chemiluminescence imaging*

Figure 6.3 shows the OH* chemiluminescence images of the flame forcing responses as a result of the two acoustic perturbation configurations at 320 Hz. The flame responses are attributed

to the pressure antinode (0° speaker phase difference) and the pressure node (180° speaker phase difference) at the center of the burner array. The averaged OH* chemiluminescence images, calculated using 1000 images, show that hydrogen enrichment promotes flame length scale reduction. The mesoscale flame array shows the longest flame structure at X_{H2} = 0% and becomes shorter with increasing hydrogen enrichment as observed in the 20% and 40% hydrogen flame images in Figure 6.3 (a) and (b).

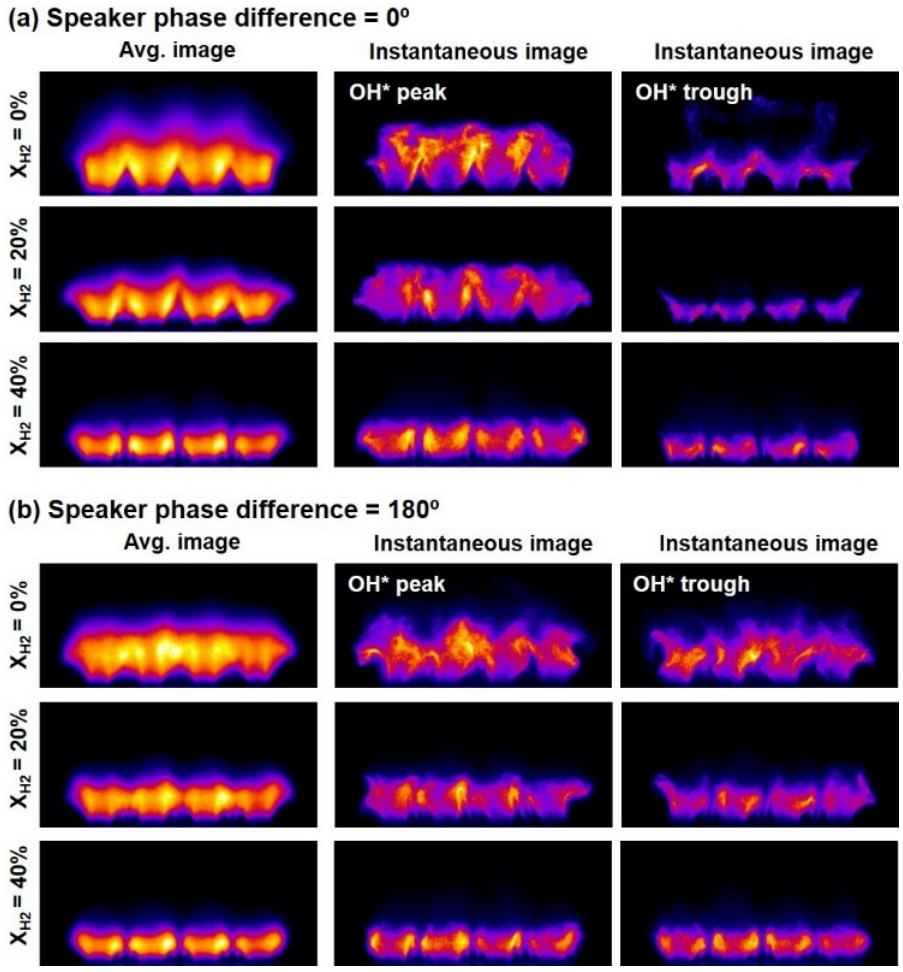

Figure 6.3. OH chemiluminescence images of (a) axial flame fluctuations by the pressure antinode and (b) lateral flame fluctuations by the pressure node at an equivalence ratio of 0.7 and an air flow rate of 60 SLPM.*

The instantaneous images in Figure 6.3 (a) show the axial flame fluctuations due to the pressure antinode at the burner center. Large flame surface fluctuations were observed in the 0% and 20% hydrogen-enriched flame arrays during a perturbation cycle. At 40% hydrogen enrichment, the flame surface fluctuations were significantly suppressed. The results exhibit that the overall improvement in reactivity of hydrogen-enriched flame arrays induces flame length scale reduction and promotes M-shaped flame transition as shown in 40% hydrogen flame array, ultimately leading to more stable burner operation.

In Figure 6.3 (b), the flame forcing response shows lateral fluctuations due to the pressure node at the burner center. Flame length scale reduction is also observed in the hydrogen-enriched flame arrays. At $X_{H2} = 0\%$, the flame array shows large flame movements and long flame structures during a perturbation cycle in the instantaneous images. In the 20% and 40% hydrogen-enriched flame arrays, however, the flame fluctuations are suppressed and the flame structures show shorter flame length scales. Therefore, the increase in flame reactivity due to hydrogen addition results in more stable operation under the two flame perturbation configurations.

6.3.2. Heat release characteristics

OH* chemiluminescence intensity can be used as an indicator of combustion heat release rate [121, 122, 130]. Therefore, the vertical OH* chemiluminescence profiles along the axial axis of the burner array are introduced in Figure 6.4. The profiles were constructed by integrating OH* chemiluminescence counts of the six averaged images in Figure 6.3. These profiles are used to show flame length scale reduction as well as heat release distribution estimation from the burner surface. The peaks in the profiles are used as an indicator of the combustion reaction length scale.

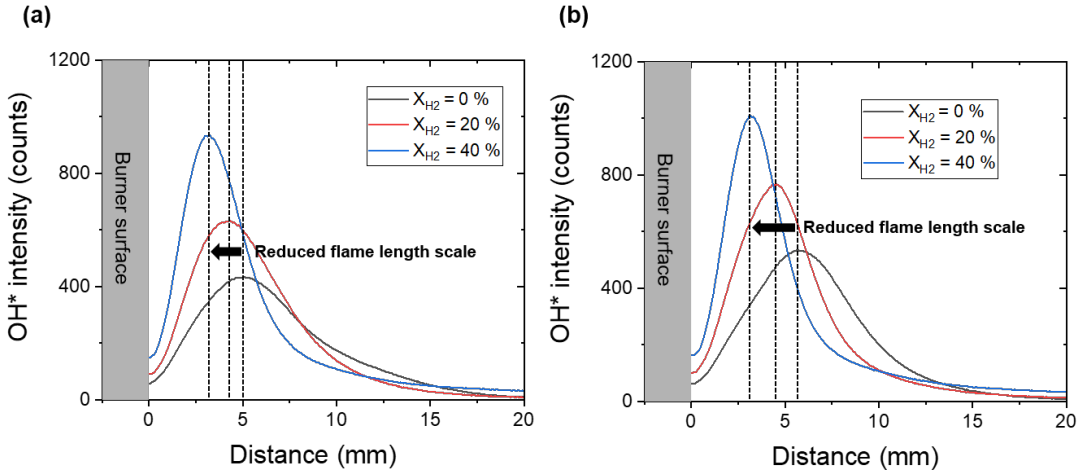

Figure 6.4. Vertical OH chemiluminescence profiles of the (a) axially-perturbed flame array and (b) laterally-perturbed flame arrays.*

Figure 6.4 (a) shows the flame length scales of the axially-perturbed flame arrays (pressure antinode). The heat release peak heights were observed at 5.05 mm, 4.30 mm, and 3.19 mm above the burner surface for the 0%, 20%, and 40% hydrogen flame arrays, respectively. Figure 6.4 (b) shows the flame length scales of the laterally-perturbed flame arrays (pressure node). The heat release peak heights were observed at 5.69 mm, 4.53 mm, and 3.14 mm for the 0%, 20%, and 40% hydrogen flame arrays, respectively. The distance between the OH* peak and the burner surface decreases with increasing hydrogen concentration in both perturbation configurations. The laterally fluctuating flame arrays show more reduction in the flame length scale and exhibit narrower OH* distributions compared to those of the axially-perturbed flame arrays.

Figure 6.5 represents the global heat release rate fluctuations of the flame arrays for 0.2 s. The global heat release rate was estimated by integrating every OH* chemiluminescence count of

an image. The burner operation conditions were set to an equivalence ratio of 0.7 and air flow rate of 60 SLPM. From Figure 6.5 (a), hydrogen addition increased the amplitude of the normalized heat release fluctuations at X_{H2} = 20% due to large flame surface changes as shown in Figure 6.3 (a). The flame structure transition between V- and M-shaped structures was triggered at every perturbation cycle and induced large heat release fluctuations. However, the flame quickly became well-stabilized as indicated by the M-shaped flame at X_{H2} = 40%, as seen in Figure 6.3 3 (a), thereby resulting in reduced heat release rate fluctuations.

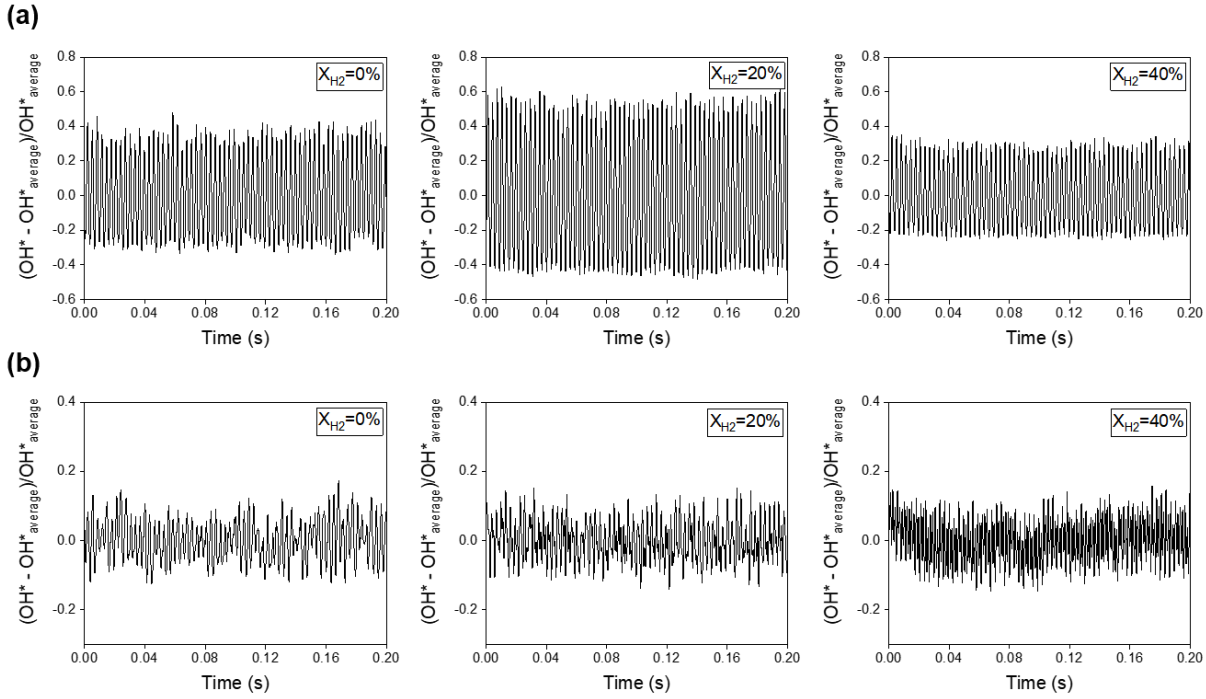

Figure 6.5. Global heat release fluctuations of the (a) axially-perturbed flame array and (b) laterally-perturbed flame array at 320 Hz.

Figure 6.5 (b) shows the response of the laterally-perturbed flames with 0, 20, and 40% hydrogen enrichments. The global heat release rate fluctuations show similar fluctuating

amplitudes across three hydrogen enrichment conditions. Results show that the global heat release characteristics are less sensitive to the laterally-perturbed flame responses compared to the axially-perturbed flame responses. These results are attributed to the fact that flame stabilization is closely linked to the pressure antinode above the burner array. More detailed study on the flame fluctuation characteristics will be performed in the next section using spatially-resolved OH-PLIF images and SPOD analysis.

6.3.3. OH-PLIF imaging

The phase-averaged OH-PLIF images of axially- and laterally-perturbed flame arrays across 20 acoustic perturbation cycles are presented in Figure 6.6 and Figure 6.7, respectively. The phase information in the figures is based on the imposed acoustic forcing wave timescale. The imaging plane was along the centerline of the 2nd row of the mesoscale burner array. These images provide spatially-resolved flame structures with which SPOD analysis can be performed.

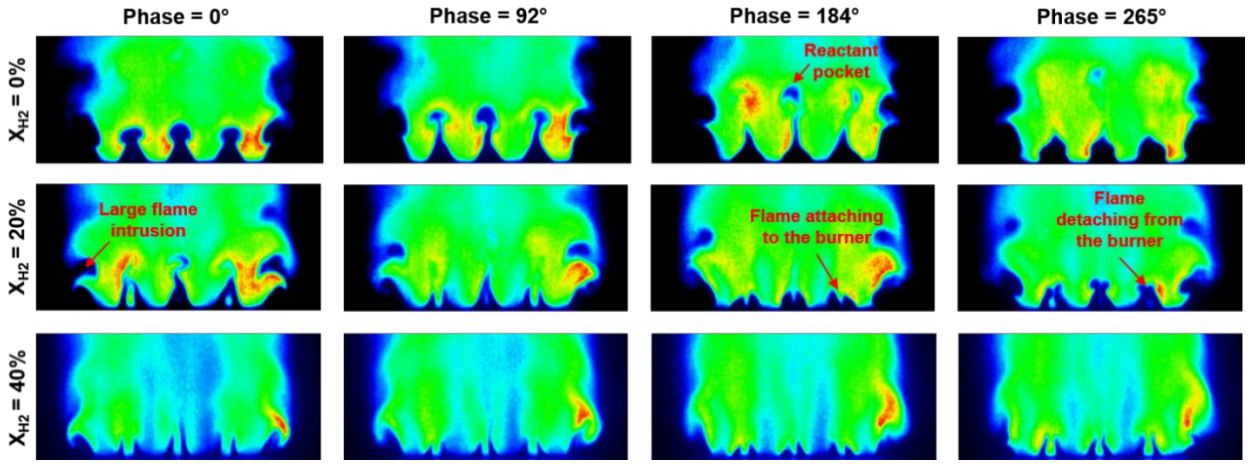

Figure 6.6. Phase-averaged OH-PLIF images of the axially-perturbed flame responses at 320 Hz.

The axially-perturbed flame structures are clearly visualized in Figure 6.6. V-shaped flame structures stabilized on each bluff body were observed at X_{H2} = 0%. The reactant pocket in the 184° image was formed at the flame-to-flame interaction region due to acoustic forcing. For the 20% hydrogen-enriched flame array, large flame intrusions were detected at the outer flames. Furthermore, flame attaching and detaching at the flame interaction region were observed during a perturbation cycle. This result indicates that flame structure transitions can be an important factor for large global heat release rate fluctuations as shown in Figure 6.5 (a). At 40% hydrogen enrichment, only M-shaped structures were observed across a perturbation cycle. Also, flame structures appear to be wider and show less flame surface variations than those of the 0% and 20% hydrogen-enriched flame arrays.

The laterally-perturbed flame fluctuations in Figure 6.7 are the result of the pressure node at the burner center. M-shaped flame structures were formed at the flame interaction zones in the 20% and 40% hydrogen-enriched flames. The lateral movement of the flame array is greatly minimized as a result of hydrogen enhancement. Overall, the hydrogen-enriched flame arrays promoted the flame structure transition and reduced the combustion length scale, ultimately making the flames more robust against laterally-perturbed flame forcing.

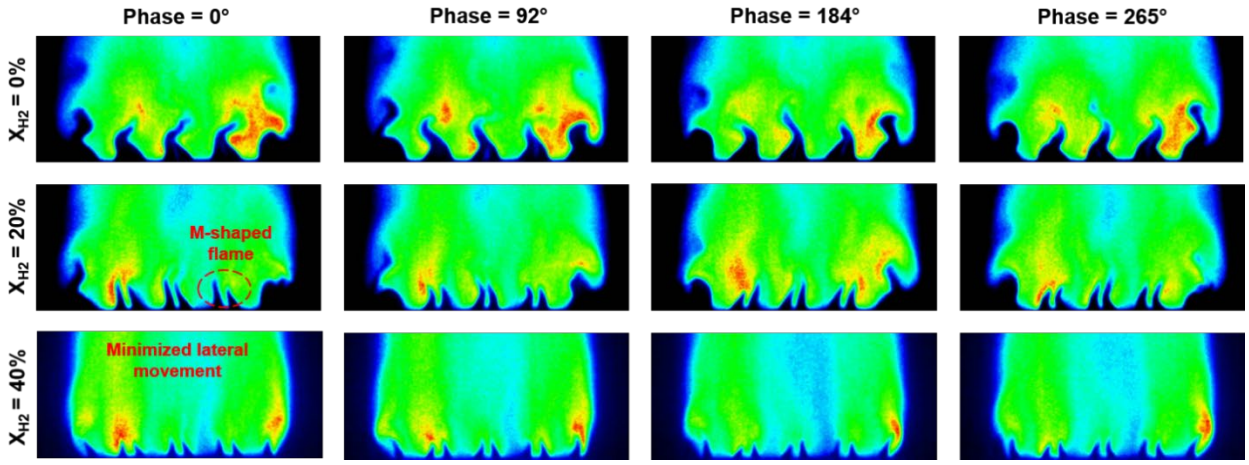

Figure 6.7. Phase-averaged OH-PLIF images of the laterally-perturbed flame responses at 320 Hz.

6.3.4. SPOD analysis

SPOD analysis is used to study the effects of hydrogen enrichment on the stability of the mesoscale burner array subjected to various perturbation configurations. SPOD is a subset of proper orthogonal decomposition (POD) analysis method. A scalar field $q(x,t)$ can be decomposed into a mean part and a fluctuation part, which consists of spatial eigenmodes *Φ(x)* and time coefficients $a_n(t)$, by the following equation.

$$q(x,t) = \bar{q}(x) + q'(x,t) = \bar{q}(x) + \sum_{n=1}^{N} a_n(t)\Phi_n(x)$$

In this study, the fluctuation part is decomposed by SPOD. Unlike POD, an SPOD filter operation is applied on the POD temporal correlation matrix to capture a coherent phenomenon in the mesoscale flame arrays. More details for the analysis used here are explained in [75, 76]. A Gaussian filter is used for the filter operation and the filter size is set to 31, which is approximated by calculating the ratio of the imaging frame rate (10 kHz) to the acoustic forcing frequency (320 Hz). This filter allows the extraction of coherent information even in the presence of external noise

and frequency variations during a physical phenomenon. As a result, the analysis method can extract coherent modes that are induced by flame fluctuations.

1000 OH-PLIF images from each flame condition in Figure 6.5 were decomposed using SPOD to capture flame dynamics under acoustic forcing. The six mean mode structures ($\bar{q}(x)$) in Figure 6.8 show flame structures subjected to the two perturbation configurations and hydrogen enrichments. These mean structures demonstrate that shorter flame merging lengths are induced by hydrogen enrichment. Also, M-shaped flames induced by higher hydrogen enrichment increase the flame holding strength and result in greater flame stability under both acoustic perturbation configurations as seen in Figure 6.5.

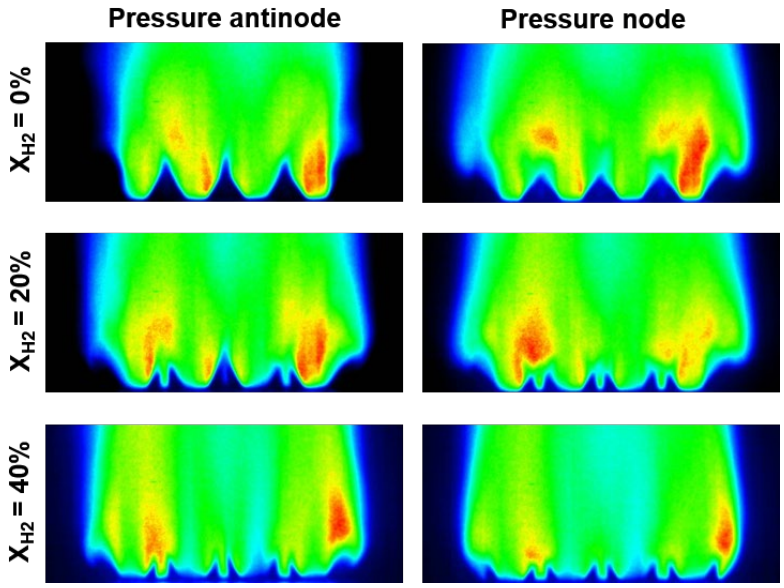

Figure 6.8. Mean mode structures subjected to the pressure antinode and pressure node at 320 Hz.

The SPOD spectra of the axially-perturbed flame arrays with 0%, 20%, and 40% hydrogen enrichments are shown in Figure 6.9 (a). The mode energy contents and frequencies were calculated based on the method in [75, 76]. Each dot in the figure represents an SPOD mode pair and the coherence of the SPOD mode pair is indicated by the dot size [75, 76, 131]. Modes with large heat release fluctuations have higher energy content. Each mode is ranked by its energy content so that modes that are relevant to large flame fluctuations can be quickly identified. At X_{H2} = 0% (pure methane flame), a dominant mode (S1) is detected at 320 Hz and the energy content of the mode is 18.6% (of the total fluctuating energy). Dominant modes in the 20% and 40% hydrogen enrichment flames are also detected at the same frequency. The dominant mode (S2) in the X_{H2} = 20% spectrum has a slightly higher energy content of 24.0% compared to that of the pure methane flame. Despite hydrogen enrichment leading to increased reactivity and higher flame speed, higher fluctuating energy content is observed and that is largely associated with the flame shape transitioning as observed in Figure 6.6. In the 40% hydrogen-enriched flame array, 13.2% of all fluctuating energy content is contained in mode S3. This mode (S3) represents the most robust flame under the acoustic perturbation at 320 Hz. The results indicate that hydrogen-enriched flames can be more stable if there are no flame shape transitions during acoustic perturbations.

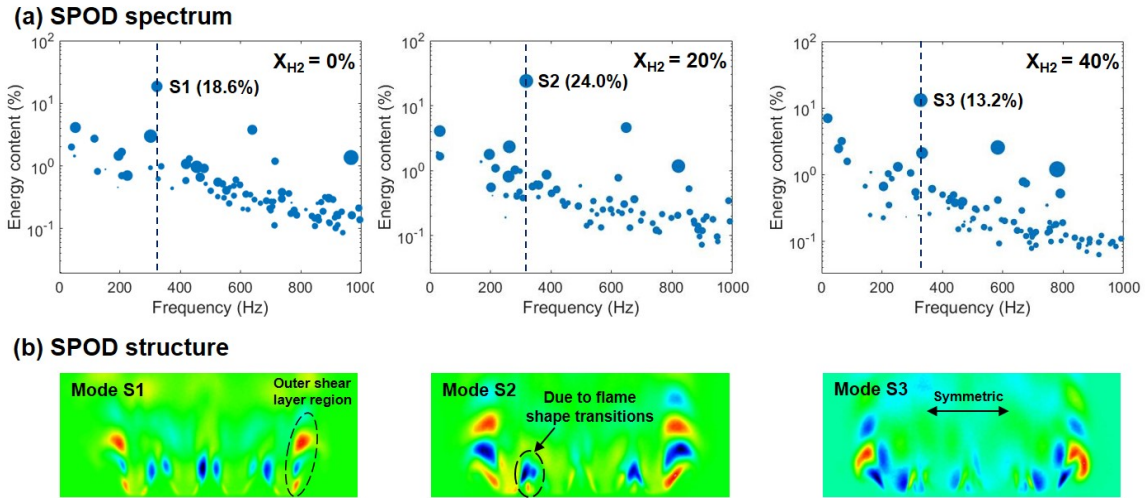

Figure 6.9. SPOD spectra and mode structures of the axially-perturbed flame arrays at 320 Hz.

The dominant SPOD mode structures are visualized in Figure 6.9 (b). These mode structures are attributed to the acoustic forcing at 320 Hz. Thin repeating structures are observed at the shear layers of the outer burner elements in the S1 mode structure. The S2 mode structure shows large fluctuating structures at the outer shear layer region. Another fluctuation structure can be found at the flame interaction region near the burner surface where flame shape transitions occur. The S3 mode structure shows no distinguishable fluctuating structures near the stable flame region at the center flames with the absence of flame shape transitions. Overall, regardless of hydrogen enrichment, the axially-perturbed flame fluctuations are very symmetrical about the burner axis. Therefore, all the modes are associated with the acoustic wave propagation.

The SPOD spectra and dominant fluctuating mode structures of the laterally-perturbed flames with 0%, 20%, and 40% hydrogen enrichments are shown in Figure 6.10. Dominant fluctuating modes (mode S4, S5, and S6) were all found at a frequency of 320 Hz. The energy contents of these modes are 19.0%, 15.5%, and 9.7% for hydrogen volumetric concentrations of 0%, 20%, and 40%, respectively. The SPOD spectra in Figure 6.10 (a) clearly show that hydrogen enrichment can minimize transverse flame fluctuations. The transition to M-shaped flames induced

by hydrogen enrichment further enhances the flame stability and improves the flame holding on the burner array.

Figure 6.10 (b) shows the dominant SPOD mode structures of the 0%, 20%, and 40% hydrogen-enriched flames, respectively. All of the structures in Figure 6.10 (b) are asymmetric and are attributed to the pressure node effect on the burner array. At $X_{H2} = 0\%$, distinct structures were observed in both the center and the outer flame zone. However, the fluctuating structures at the center flames are greatly reduced by adding hydrogen as shown in the S5 and S6 mode structures. The M-shaped flames at the flame interaction regions show much smaller structures that are located closer to the burner surface. At $X_{H2} = 40\%$, the fluctuating structures near the outer flame region were also reduced. The flame shape transition from the V- to M-shaped flame makes the flame array more robust against the lateral flame forcing. Therefore, in laterally-perturbed flow conditions, hydrogen enhancement can be an effective method to reduce the flame length scale and improve the flame holding strength.

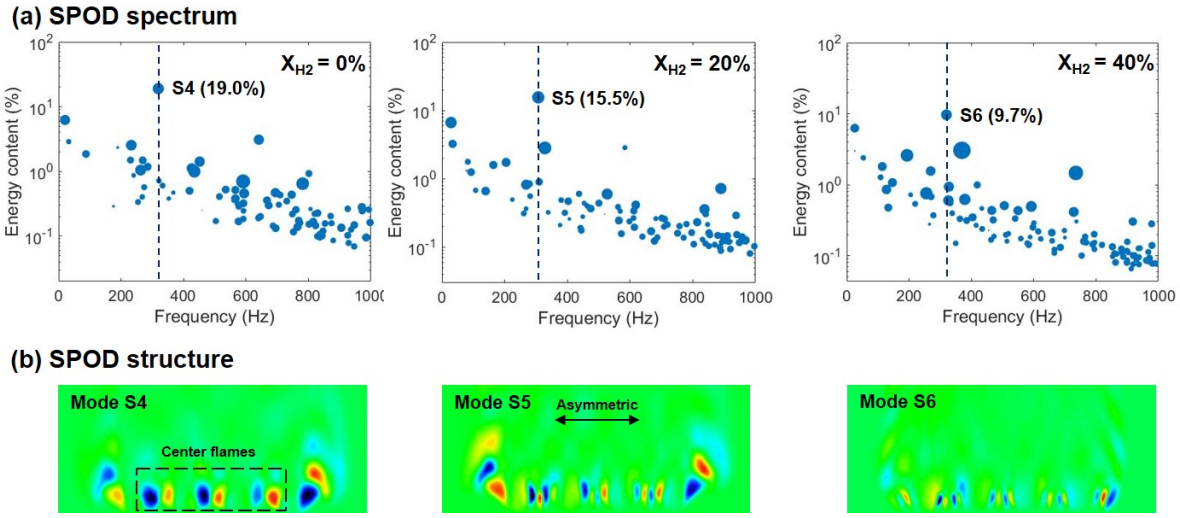

Figure 6.10. SPOD spectra and mode structures of the laterally-perturbed flame arrays at 320 Hz.

6.4. Conclusions

Hydrogen enhancement in a mesoscale burner array has been studied based on flame dynamics and combustion stability under acoustic perturbations. The mesoscale flame arrays showed axially- and laterally-perturbed flame responses by two different transverse acoustic perturbation configurations. The flame length scale comparison between the mesoscale flame arrays, evaluated using the vertical OH* chemiluminescence profiles, showed significant length scale reduction by hydrogen addition even under acoustic perturbations. Furthermore, overall flame stability of the mesoscale flame arrays was improved with global heat release fluctuation reduction by hydrogen enhancement. OH-PLIF imaging provided spatially-resolved flame structures during acoustic perturbations and revealed V- to M-shaped flame structure transition can induce large heat release fluctuations. Furthermore, the effects of hydrogen addition on flame dynamics were studied using OH-PLIF images and SPOD analysis. The SPOD spectra revealed that improved combustion stability and reduced flame length scale were achieved with hydrogen addition under transverse acoustic perturbations in the mesoscale burner array.

CHAPTER 7. CONCLUSIONS AND FUTURE WORK

7.1. Conclusions

This study presents the development of a stable and efficient small-scale combustor architecture whose performance is comparable to that of large-scale burners. The burner array reduced the susceptibility to flame extinction while maintaining high combustion efficiency under fuel-lean operating conditions. This was facilitated by flame-to-flame interactions between neighboring burner elements. The flame-to-flame interaction effects on the mesoscale flame phenomenology were studied using multi-species (OH and CH_2O) PLIF images.

Next, the design of a diffusion type mesoscale burner array was introduced for practical combustion applications, such as small-scale propulsion and power generation systems. The diffusion type mesoscale burner array was designed to mitigate any unstable operations that result from flame flashback. The diffusion burner performance was compared to its premixed mode counterpart. The radial fuel injection in the diffusion burner array produced performance output comparable to the premixed flame array.

Furthermore, the mesoscale burner array was adapted for use with vaporized complex liquid fuels, such as Jet A, in the premixed mode. The effects of inlet temperature and degree of Jet A vaporization on flame stability were studied and compared with those of methane combustion. Fuel composition was observed to have a significant effect on the flame characteristics and dynamics of the mesoscale burner array.

Finally, to improve the mesoscale burner performance, the potential use of hydrogen as a fuel enhancer was investigated in terms of combustion stability and flame length scale. The hydrogen and methane hybrid fueled mesoscale flame array, visualized using OH*

chemiluminescence and OH-PLIF imaging, exhibited improved combustion stability and reduced flame length even under acoustic perturbations.

Herein, the development and characterization of a mesoscale burner array were comprehensively studied. Moreover, the mesoscale architecture can be used to extend combustion capabilities for compact and practical applications without compromising the performance.

7.2. Recommendations for future work

An optically accessible laboratory combustor (Figure 7.1) comprising a 3D printed recuperator and a multi-array burner architecture can be used to study the engine efficiency in compact combustors. The prototype design can be a fully enclosed combustor with integration of fuel injection and heat recuperation. Waste heat recuperation has long been viewed as a key requirement for boosting compact/micro gas turbine efficiency. A heat exchanger is used to preheat incoming air or a reactant mixture to high temperatures, ideally above the boiling point of the fuel. Such high temperatures allow for rapid vaporization of the fuel and in some cases may promote the occurrence of highly efficient combustion modes, such as “flameless” reaction zones. Additionally, the high inlet temperature can improve fuel vaporization and flame stability even in mesoscale burner operations with heavy hydrocarbon fuels. The optimized operating parameters can be obtained using optical diagnostics.

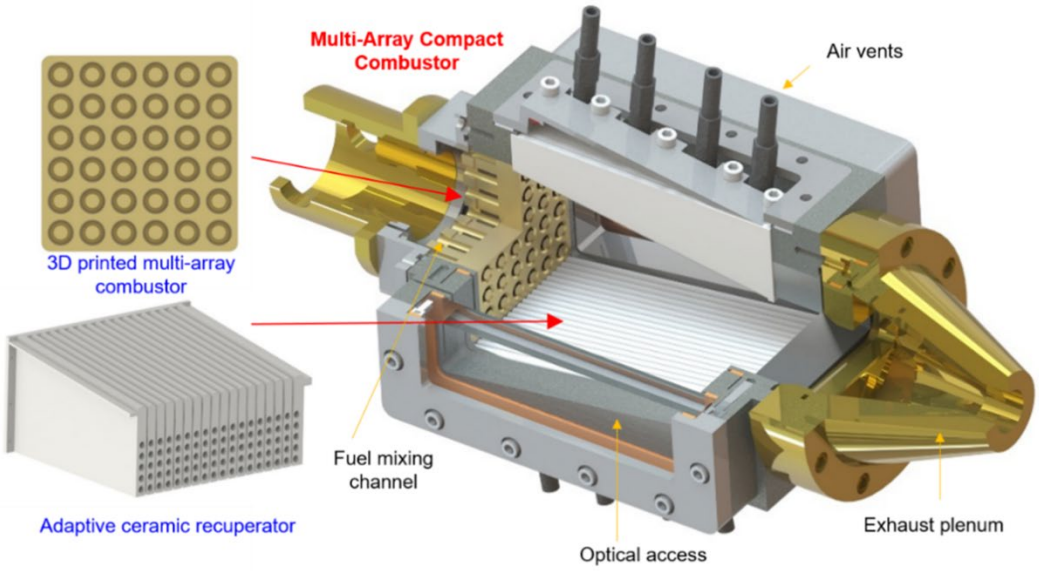

Figure 7.1. Schematic of the integrated multi-array prototype combustor.

For stable burner operation, combustor performance under high inlet temperatures should be studied to mitigate carbon formation inside the fuel delivery system integrated within the recuperator. Therefore, accurate and quantifiable analyses are highly recommended to study fuel composition changes, thermal cracking, and carbon formation.

Novel studies investigating recuperator design can be used to gain insight into a fundamental open question: What parameters are critical for the development of a highly efficient compact combustor?

REFERENCES

[1] Maruta K. Micro and mesoscale combustion. Proceedings of the Cobustion Institute (2011) **33**, 125-150.

[2] Ju Y, Maruta K. Microscale combustion: Technology development and fundamental research. Progress in Energy and Combustion Science (2011) **37**, 669-715.

[3] Chou S, Yang W, Chua K, Li J, Zhang K. Development of micro power generators–a review. Applied Energy (2011) **88**, 1-16.

[4] Hosseini SE, Wahid MA. Investigation of bluff-body micro-flameless combustion. Energy Conversion and Management (2014) **88**, 120-128.

[5] Raimondeau S, Norton D, Vlachos D, Masel R. Modeling of high-temperature microburners. Proceedings of the Combustion Institute (2002) **29**, 901-907.

[6] Wierzbicki TA, Lee IC, Gupta AK. Performance of synthetic jet fuels in a meso-scale heat recirculating combustor. Applied Energy (2014) **118**, 41-47.

[7] Walther DC, Ahn J. Advances and challenges in the development of power-generation systems at small scales. Progress in Energy and Combustion Science (2011) **37**, 583-610.

[8] Epstein AH. Millimeter-scale, micro-electro-mechanical systems gas turbine engines. Journal of Engineering for Gas Turbines and Power (2004) **126**, 205-226.

[9] Ahn J, Eastwood C, Sitzki L, Ronney PD. Gas-phase and catalytic combustion in heat-recirculating burners. Proceedings of the Combustion Institute (2005) **30**, 2463-2472.

[10] Kim NI, Kato S, Kataoka T, Yokomori T, Maruyama S, Fujimori T, et al. Flame stabilization and emission of small Swiss-roll combustors as heaters. Combustion and Flame (2005) **141**, 229-240.

[11] Kyritsis DC, Guerrero-Arias I, Roychoudhury S, Gomez A. Mesoscale power generation by

a catalytic combustor using electrosprayed liquid hydrocarbons. Proceedings of the Combustion Institute (2002) **29**, 965-972.

[12] Kyritsis DC, Roychoudhury S, McEnally CS, Pfefferle LD, Gomez A. Mesoscale combustion: A first step towards liquid fueled batteries. Experimental Thermal and Fluid Science (2004) **28**, 763-770.

[13] Howell J, Hall MJ, Ellzey JL. Combustion of hydrocarbon fuels within porous inert media. Progress in Energy and Combustion Science (1996) **22**, 121-145.

[14] Vick M, Young T, Kelly M, Tuttle S, Hinnant K. A simple recuperated ceramic microturbine: design concept, cycle analysis, and recuperator component prototype tests. ASME Turbo Expo (2016), GT2016-57780.

[15] Rathsack TC, Bohan BT, Polanka MD, Rutledge JL. Experimental analysis of an additively manufactured cooled ultra compact combustor vane. ASME Turbo Expo (2019), GT2019-91425.

[16] Miller JA, Bowman CT. Mechanism and modeling of nitrogen chemistry in combustion. Progress in Energy and Combustion Science (1989) **15**, 287-338.

[17] Lee J, Santavicca D. Experimental diagnostics for the study of combustion instabilities in lean premixed combustors. Journal of Propulsion and Power (2003) **19**, 735-750.

[18] McManus K, Poinsot T, Candel S. A review of active control of combustion instabilities. Progress in Energy and Combustion Science (1993) **19**, 1-29.

[19] Lieuwen TC, Yang V. Combustion instabilities in gas turbine engines: operational experience, fundamental mechanisms, and modeling. American Institute of Aeronautics and Astronautics, 2005.

[20] Evans CJ, Kyritsis DC. Operational regimes of rich methane and propane/oxygen flames in mesoscale non-adiabatic ducts. Proceedings of the Combustion Institute (2009) **32**, 3107-3114.

[21] Maruta K, Kataoka T, Kim NI, Minaev S, Fursenko R. Characteristics of combustion in a narrow channel with a temperature gradient. Proceedings of the Combustion Institute (2005) **30**, 2429-2436.

[22] Maruta K, Parc J, Oh K, Fujimori T, Minaev S, Fursenko R. Characteristics of microscale combustion in a narrow heated channel. Combustion, Explosion, and Shock Waves (2004) **40**, 516-523.

[23] Taylor GI, Green AE. Mechanism of the Production of Small Eddies from Large Ones. Proceedings of the Royal Society of London Series A - Mathematical and Physical Sciences (1937) **158**, 499-521.

[24] Rajasegar R, Mitsingas CM, Mayhew EK, Liu Q, Lee T, Yoo J. Development and characterization of additive-manufactured mesoscale combustor array. Journal of Energy Engineering (2018) **144**, 04018013.

[25] Candel SM. Combustion instabilities coupled by pressure waves and their active control. Symposium (International) on Combustion (1992) **24**, 1277-1296.

[26] Lefebvre AH. Gas turbine combustion. Taylor & Francis, 1999.

[27] Rajasegar R, Mitsingas CM, Mayhew EK, Liu Q, Lee T, Yoo J. Development and experimental characterization of metal 3D-printed scalable swirl stabilized mesoscale burner array. ASME International Mechanical Engineering Congress and Exposition (2017), IMECE2017-72577.

[28] Hammack SD, Skiba AW, Lee T, Carter CD. CH PLIF and PIV implementation using C-X (0, 0) and intra-vibrational band filtered detection. Applied Physics B (2018) **124**, 1-5.

[29] Brackmann C, Nygren J, Bai X, Li Z, Bladh H, Axelsson B, et al. Laser-induced fluorescence of formaldehyde in combustion using third harmonic Nd:YAG laser excitation. Spectrochimica

Acta Part A: Molecular and Biomolecular Spectroscopy (2003) **59**, 3347-3356.

[30] Röder M, Dreier T, Schulz C. Simultaneous measurement of localized heat-release with OH/CH_2O–LIF imaging and spatially integrated OH^* chemiluminescence in turbulent swirl flames. Proceedings of the Combustion Institute (2013) **34**, 3549-3556.

[31] Sjöholm J, Rosell J, Li B, Richter M, Li Z, Bai X-S, et al. Simultaneous visualization of OH, CH, CH_2O and toluene PLIF in a methane jet flame with varying degrees of turbulence. Proceedings of the Combustion Institute (2013) **34**, 1475-1482.

[32] Clouthier DJ, Ramsay DA. The spectroscopy of formaldehyde and thioformaldehyde. Annual Review of Physical Chemistry (1983) **34**, 31-58.

[33] Najm HN, Paul PH, Mueller CJ, Wyckoff PS. On the adequacy of certain experimental observables as measurements of flame burning rate. Combustion and Flame (1998) **113**, 312-332.

[34] Lee SH, Chen IC. Axis switching in the $\tilde{B}^2A'$–$\tilde{X}^2A'$ transition of HCO and fluorescence lifetimes of the $\tilde{B}^2A'(0, 0, 0)$ rotational states. The Journal of Chemical Physics (1996) **105**, 2583-2590.

[35] Ayoola B, Balachandran R, Frank J, Mastorakos E, Kaminski C. Spatially resolved heat release rate measurements in turbulent premixed flames. Combustion and Flame (2006) **144**, 1-16.

[36] Zhang X, Lin Y, Xue X, Zhang L, Zhang C. Experimental investigation of convergent and convergent-divergent micro swirling flame behavior and stabilization. ASME Turbo Expo (2016), GT2016-56944.

[37] Guiberti T, Zimmer L, Durox D, Schuller T. Experimental analysis of V-to M-shape transition of premixed CH_4/H_2/air swirling flames. ASME Turbo Expo (2013), GT2013-94842.

[38] Fugger CA, Paxton B, Gord JR, Rankin BA, Caswell AW. Measurements and analysis of flow-flame interactions in bluff-body-stabilized turbulent premixed propane-air flames. AIAA

Scitech Forum (2019), AIAA 2019-0733.

[39] Kuwana K, Kato S, Kosugi A, Hirasawa T, Nakamura Y. Experimental and theoretical study on the interaction between two identical micro-slot diffusion flames: Burner pitch effects. Combustion and Flame (2016) **165**, 346-353.

[40] Bowman CT. Kinetics of pollutant formation and destruction in combustion. Progress in Energy and Combustion Science (1979) **1**, 35-45.

[41] Bardos A, Walters K, Boutross M, Lee S, Edwards C, Bowman C. Effects of pressure on performance of mesoscale burner arrays for gas-turbine applications. Journal of Propulsion and Power (2007) **23**, 884-886.

[42] Zhao W, Qiu P, Liu L, Shen W, Lyu Y. Combustion and NOx emission characteristics of dual-stage lean premixed flame. Applied Thermal Engineering (2019) **160**, 113951.

[43] Rajasegar R, Mitsingas CM, Mayhew EK, Yoo J, Lee T. Proper orthogonal decomposition for analysis of plasma-assisted premixed swirl-stabilized flame dynamics. IEEE Transactions on Plasma Science (2016) **44**, 2940-2951.

[44] Huang Y, Yang V. Dynamics and stability of lean-premixed swirl-stabilized combustion. Progress in Energy and Combustion Science (2009) **35**, 293-364.

[45] Samarasinghe J, Peluso S, Szedlmayer M, De Rosa A, Quay B, Santavicca D. Three-dimensional chemiluminescence imaging of unforced and forced swirl-stabilized flames in a lean premixed multi-nozzle can combustor. Journal of Engineering for Gas Turbines and Power (2013) **135**, 101503.

[46] Cvoro V, Easson WJ. Optimisation of furnace design for in-furnace NOx reduction: The effect of pitch spacing on multiple burner jet interactions. Fuel (2003) **82**, 2075-2085.

[47] Szedlmayer MT, Quay BD, Samarasinghe J, De Rosa A, Lee JG, Santavicca DA. Forced

flame response of a lean premixed multi-nozzle can combustor. ASME Turbo Expo (2011), GT2011-46080.

[48] Danon B, Cho E-S, De Jong W, Roekaerts D. Parametric optimization study of a multi-burner flameless combustion furnace. Applied Thermal Engineering (2011) **31**, 3000-3008.

[49] Davis LB. Dry low NOx combustion systems for GE heavy-duty gas turbines. ASME International Gas Turbine and Aeroengine Congress and Exhibition (1996), 96-GT-027.

[50] Choi J, Rajasegar R, Mitsingas CM, Liu Q, Lee T, Yoo J. Effect of flame interaction on swirl-stabilized mesoscale burner array performance. Energy (2020) **192**, 116661.

[51] Lei Y, Chen W, Lei J. Combustion and direct energy conversion inside a micro-combustor. Applied Thermal Engineering (2016) **100**, 348-355.

[52] Lee S, Svrcek M, Edwards CF, Bowman CT. Mesoscale burner arrays for gas-turbine reheat applications. Journal of Propulsion and Power (2006) **22**, 417-424.

[53] Kang X, Veeraragavan A. Experimental investigation of flame stability limits of a mesoscale combustor with thermally orthotropic walls. Applied Thermal Engineering (2015) **85**, 234-242.

[54] Lieuwen T, McDonell V, Santavicca D, Sattelmayer T. Burner development and operability issues associated with steady flowing syngas fired combustors. Combustion Science and Technology (2008) **180**, 1169-1192.

[55] Kim WH, Park TS. Non-premixed lean flame characteristics depending on air hole positions in a baffled micro combustor. Applied Thermal Engineering (2018) **129**, 431-445.

[56] Rajasegar R, Choi J, McGann B, Oldani A, Lee T, Hammack SD, et al. Mesoscale burner array performance analysis. Combustion and Flame (2019) **199**, 324-337.

[57] 18.0 ANSYS Fluent Theory Guide 18.0, Ansys Inc., 2017.

[58] Kuo C, Ronney P. Numerical modeling of non-adiabatic heat-recirculating combustors.

Proceedings of the Combustion Institute (2007) **31**, 3277-3284.

[59] Fan A, Wan J, Maruta K, Yao H, Liu W. Interactions between heat transfer, flow field and flame stabilization in a micro-combustor with a bluff body. International Journal of Heat and Mass Transfer (2013) **66**, 72-79.

[60] Li J, Chou S, Yang W, Li Z. Experimental and numerical study of the wall temperature of cylindrical micro combustors. Journal of Micromechanics and Microengineering (2008) **19**, 015019.

[61] Akhtar S, Kurnia JC, Shamim T. A three-dimensional computational model of H_2–air premixed combustion in non-circular micro-channels for a thermo-photovoltaic (TPV) application. Applied Energy (2015) **152**, 47-57.

[62] Mitsingas CM, Hammack SD, Mayhew EK, Rajasegar R, McGann B, Skiba AW, et al. Simultaneous high speed PIV and CH PLIF using R-branch excitation in the $C^2\Sigma^+$-$X^2\Pi$ (0, 0) band. Proceedings of the Combustion Institute (2019) **37**, 1479-1487.

[63] Rajasegar R, Choi J, McGann B, Oldani A, Lee T, Hammack SD, et al. Comprehensive combustion stability analysis using dynamic mode decomposition. Energy & Fuels (2018) **32**, 9990-9996.

[64] Cavaliere DE, Kariuki J, Mastorakos E. A comparison of the blow-off behaviour of swirl-stabilized premixed, non-premixed and spray flames. Flow, Turbulence and Combustion (2013) **91**, 347-372.

[65] Fooladgar E, Chan C. Effects of stratification on flame structure and pollutants of a swirl stabilized premixed combustor. Applied Thermal Engineering (2017) **124**, 45-61.

[66] Guahk YT, Lee DK, Oh KC, Shin HD. Flame-intrinsic Kelvin-Helmholtz instability of flickering premixed flames. Energy & Fuels (2009) **23**, 3875-3884.

[67] Najm HN, Ghoniem AF. Coupling between vorticity and pressure oscillations in combustion instability. Journal of Propulsion and Power (1994) **10**, 769-776.

[68] Thumuluru SK, Lieuwen T. Characterization of acoustically forced swirl flame dynamics. Proceedings of the Combustion Institute (2009) **32**, 2893-2900.

[69] Dhanuka SK, Temme JE, Driscoll J. Unsteady aspects of lean premixed prevaporized gas turbine combustors: flame-flame interactions. Journal of Propulsion and Power (2011) **27**, 631-641.

[70] Pun W, Palm S, Culick F. Combustion dynamics of an acoustically forced flame. Combustion Science and Technology (2003) **175**, 499-521.

[71] Docquier N, Candel S. Combustion control and sensors: a review. Progress in Energy and Combustion Science (2002) **28**, 107-150.

[72] Huang Y, Ratner A. Experimental investigation of thermoacoustic coupling for low-swirl lean premixed flames. Journal of Propulsion and Power (2009) **25**, 365-373.

[73] Kang D, Culick F, Ratner A. Combustion dynamics of a low-swirl combustor. Combustion and Flame (2007) **151**, 412-425.

[74] Oberleithner K, Schimek S, Paschereit CO. Shear flow instabilities in swirl-stabilized combustors and their impact on the amplitude dependent flame response: A linear stability analysis. Combustion and Flame (2015) **162**, 86-99.

[75] Sieber M, Paschereit CO, Oberleithner K. Spectral proper orthogonal decomposition. Journal of Fluid Mechanics (2016) **792**, 798-828.

[76] Sieber M, Paschereit CO, Oberleithner K. Advanced identification of coherent structures in swirl-stabilized combustors. Journal of Engineering for Gas Turbines and Power (2017) **139**, 021503.

[77] Berkooz G, Holmes P, Lumley JL. The proper orthogonal decomposition in the analysis of turbulent flows. Annual Review of Fluid Mechanics (1993) **25**, 539-575.

[78] Smith TR, Moehlis J, Holmes P. Low-dimensional modelling of turbulence using the proper orthogonal decomposition: a tutorial. Nonlinear Dynamics (2005) **41**, 275-307.

[79] Rajasegar R, Mitsingas CM, Mayhew E, Lee T, Yoo J. Proper orthogonal decomposition for flame dynamics of microwave plasma assisted swirl stabilized premixed flames. AIAA Aerospace Sciences Meeting (2017), AIAA 2017-1973.

[80] Lieuwen T, Neumeier Y, Zinn B. The role of unmixedness and chemical kinetics in driving combustion instabilities in lean premixed combustors. Combustion Science and Technology (1998) **135**, 193-211.

[81] Fernandez-Pello AC. Micropower generation using combustion: Issues and approaches. Proceedings of the Combustion Institute (2002) **29**, 883-899.

[82] Wierzbicki TA, Lee IC, Gupta AK. Combustion of propane with Pt and Rh catalysts in a meso-scale heat recirculating combustor. Applied Energy (2014) **130**, 350-356.

[83] Shirsat V, Gupta A. A review of progress in heat recirculating meso-scale combustors. Applied Energy (2011) **88**, 4294-4309.

[84] Pathania R, Skiba AW, Ciardiello R, Mastorakos E. Blow-off mechanisms of turbulent premixed bluff-body stabilised flames operated with vapourised kerosene fuels. Proceedings of the Combustion Institute (2021) **38**, 2957-2965.

[85] AFPET laboratory report, Wright-Patterson AFB, 2014LA51322007, 2014.

[86] Colket M, Heyne J, Rumizen M, Gupta M, Edwards T, Roquemore WM, et al. Overview of the national jet fuels combustion program. AIAA Journal (2017) **55**, 1087-1104.

[87] CHEMKIN-PRO 18.2, Reaction Design, 2018.

[88] Wang H, Xu R, Wang K, Bowman CT, Hanson RK, Davidson DF, et al. A physics-based approach to modeling real-fuel combustion chemistry-I. Evidence from experiments, and thermodynamic, chemical kinetic and statistical considerations. Combustion and Flame (2018) **193**, 502-519.

[89] Xu R, Wang K, Banerjee S, Shao J, Parise T, Zhu Y, et al. A physics-based approach to modeling real-fuel combustion chemistry–II. Reaction kinetic models of jet and rocket fuels. Combustion and Flame (2018) **193**, 520-537.

[90] Smith GP, Golden DM, Frenklach M, Moriarty NW, Eiteneer B, Goldenberg M, et al. GRI-Mech 3.0, 1999. http://wwwmeberkeleyedu/gri_mech.

[91] Xu R, Chen D, Wang K, Wang H. A comparative study of combustion chemistry of conventional and alternative jet fuels with hybrid chemistry approach. AIAA Aerospace Sciences Meeting (2017), AIAA 2017-0607.

[92] Pathania RS, Skiba A, Sidey JA, Mastorakos E. Blow-off mechanism in a turbulent premixed bluff-body stabilized flame with pre-vaporized fuels. AIAA Scitech Forum (2019), AIAA 2019-2238.

[93] Carbone F, Smolke JL, Fincham AM, Egolfopoulos FN. Comparative behavior of piloted turbulent premixed jet flames of C_1-C_8 hydrocarbons. Combustion and Flame (2017) **180**, 88-101.

[94] Ledesma EB, Wornat MJ, Felton PG, Sivo JA. The effects of pressure on the yields of polycyclic aromatic hydrocarbons produced during the supercritical pyrolysis of toluene. Proceedings of the Combustion Institute (2005) **30**, 1371-1379.

[95] Orain M, Baranger P, Ledier C, Apeloig J, Grisch F. Fluorescence spectroscopy of kerosene vapour at high temperatures and pressures: potential for gas turbines measurements. Applied Physics B (2014) **116**, 729-745.

[96] Chterev I, Rock N, Ek H, Emerson B, Seitzman J, Jiang N, et al. Simultaneous imaging of fuel, OH, and three component velocity fields in high pressure, liquid fueled, swirl stabilized flames at 5 kHz. Combustion and Flame (2017) **186**, 150-165.

[97] Malbois P, Salaün E, Vandel A, Godard G, Cabot G, Renou B, et al. Experimental investigation of aerodynamics and structure of a swirl-stabilized kerosene spray flame with laser diagnostics. Combustion and Flame (2019) **205**, 109-122.

[98] O'Connor J, Lieuwen T. Recirculation zone dynamics of a transversely excited swirl flow and flame. Physics of Fluids (2012) **24**, 2893-2900.

[99] Chaudhuri S, Kostka S, Renfro MW, Cetegen BM. Blowoff dynamics of bluff body stabilized turbulent premixed flames. Combustion and Flame (2010) **157**, 790-802.

[100] Rajasegar R, Choi J, Ghanekar S, Mitsingas CM, Mayhew E, Liu Q, et al. Extended proper orthogonal decomposition (EPOD) and dynamic mode decomposition (DMD) for analysis of mesoscale burner array flame dynamics. AIAA Aerospace Sciences Meeting (2018), AIAA 2018-0147.

[101] Choudhuri AR, Gollahalli S. Combustion characteristics of hydrogen–hydrocarbon hybrid fuels. International Journal of Hydrogen Energy (2000) **25**, 451-462.

[102] Kay IW, Peschke W, Guile R. Hydrocarbon-fueled scramjet combustor investigation. Journal of Propulsion and Power (1992) **8**, 507-512.

[103] Schefer R. Hydrogen enrichment for improved lean flame stability. International Journal of Hydrogen Energy (2003) **28**, 1131-1141.

[104] Kim HS, Arghode VK, Linck MB, Gupta AK. Hydrogen addition effects in a confined swirl-stabilized methane-air flame. International Journal of Hydrogen Energy (2009) **34**, 1054-1062.

[105] Choudhuri AR, Gollahalli S. Characteristics of hydrogen–hydrocarbon composite fuel

turbulent jet flames. International Journal of Hydrogen Energy (2003) **28**, 445-454.

[106] Schefer RW, Wicksall D, Agrawal A. Combustion of hydrogen-enriched methane in a lean premixed swirl-stabilized burner. Proceedings of the Combustion Institute (2002) **29**, 843-851.

[107] Phillips JN, Roby RJ. Enhanced gas turbine combustor performance using H_2-enriched natural gas. ASME Turbo Expo (1999), 99-GT-115.

[108] Bannister RL, Newby RA, Yang W-C. Final report on the development of a hydrogen-fueled combustion turbine cycle for power generation. Journal of Engineering for Gas Turbines and Power (1999) **121**, 38-45.

[109] Karbasi M, Wierzba I. The effects of hydrogen addition on the stability limits of methane jet diffusion flames. International Journal of Hydrogen Energy (1998) **23**, 123-129.

[110] Jackson GS, Sai R, Plaia JM, Boggs CM, Kiger KT. Influence of H_2 on the response of lean premixed CH_4 flames to high strained flows. Combustion and Flame (2003) **132**, 503-511.

[111] Zhang Q, Noble DR, Lieuwen T. Characterization of fuel composition effects in H_2 ／CO／CH_4 mixtures upon lean blowout. Journal of Engineering for Gas Turbines and Power (2007) **129**, 688-694.

[112] Shanbhogue S, Sanusi Y, Taamallah S, Habib M, Mokheimer E, Ghoniem A. Flame macrostructures, combustion instability and extinction strain scaling in swirl-stabilized premixed CH_4/H_2 combustion. Combustion and Flame (2016) **163**, 494-507.

[113] Chterev I, Boxx I. Effect of hydrogen enrichment on the dynamics of a lean technically premixed elevated pressure flame. Combustion and Flame (2021) **225**, 149-159.

[114] Guo S, Wang J, Zhang W, Zhang M, Huang Z. Effect of hydrogen enrichment on swirl/bluff-body lean premixed flame stabilization. International Journal of Hydrogen Energy (2020) **45**, 10906-10919.

[115] Ren J-Y, Qin W, Egolfopoulos F, Tsotsis T. Strain-rate effects on hydrogen-enhanced lean premixed combustion. Combustion and Flame (2001) **124**, 717-720.

[116] Choi J, Rajasegar R, Lee T, Yoo J. Development and characterization of swirl-stabilized diffusion mesoscale burner array. Applied Thermal Engineering (2020) **175**, 115373.

[117] Gupta RB. Hydrogen fuel: production, transport, and storage. Crc Press, 2008.

[118] Yu G, Law C, Wu C. Laminar flame speeds of hydrocarbon + air mixtures with hydrogen addition. Combustion and Flame (1986) **63**, 339-347.

[119] Incropera FP, Lavine AS, Bergman TL, DeWitt DP. Fundamentals of heat and mass transfer. Wiley, 2007.

[120] Rohsenow WM, Hartnett JP, Cho YI. Handbook of heat transfer. McGraw-Hill, 1998.

[121] Panoutsos C, Hardalupas Y, Taylor A. Numerical evaluation of equivalence ratio measurement using OH∗ and CH∗ chemiluminescence in premixed and non-premixed methane–air flames. Combustion and Flame (2009) **156**, 273-291.

[122] Hardalupas Y, Panoutsos C, Taylor A. Spatial resolution of a chemiluminescence sensor for local heat-release rate and equivalence ratio measurements in a model gas turbine combustor. Experiments in Fluids (2010) **49**, 883-909.

[123] He L, Guo Q, Gong Y, Wang F, Yu G. Investigation of OH* chemiluminescence and heat release in laminar methane–oxygen co-flow diffusion flames. Combustion and Flame (2019) **201**, 12-22.

[124] Kim D, Park SW. Effects of hydrogen addition on flame structure and forced flame response to velocity modulation in a turbulent lean premixed combustor. Fuel (2010) **89**, 3475-3481.

[125] Sé, Ducruix b, Schuller T, Durox D, Sé, Candel b. Combustion dynamics and instabilities: Elementary coupling and driving mechanisms. Journal of Propulsion and Power (2003) **19**, 722-

734.

[126] Worth NA, Dawson JR. Cinematographic OH-PLIF measurements of two interacting turbulent premixed flames with and without acoustic forcing. Combustion and Flame (2012) **159**, 1109-1126.

[127] Sung C, Law CK. Structural sensitivity, response, and extinction of diffusion and premixed flames in oscillating counterflow. Combustion and Flame (2000) **123**, 375-388.

[128] Chaparro AA, Cetegen BM. Blowoff characteristics of bluff-body stabilized conical premixed flames under upstream velocity modulation. Combustion and Flame (2006) **144**, 318-335.

[129] Gauducheau J, Denet B, Searby G. A numerical study of lean CH_4/H_2/air premixed flames at high pressure. Combustion Science and Technology (1998) **137**, 81-99.

[130] Liu Y, Tan J, Wang H, Lv L. Characterization of heat release rate by OH* and CH* chemiluminescence. Acta Astronautica (2019) **154**, 44-51.

[131] Stöhr M, Oberleithner K, Sieber M, Yin Z, Meier W. Experimental study of transient mechanisms of bistable flame shape transitions in a swirl combustor. Journal of Engineering for Gas Turbines and Power (2018) **140**, 011503.